

---

# A Rydberg Tweezer Platform with Potassium Atoms

Nikolaus Lorenz

---



München 2021

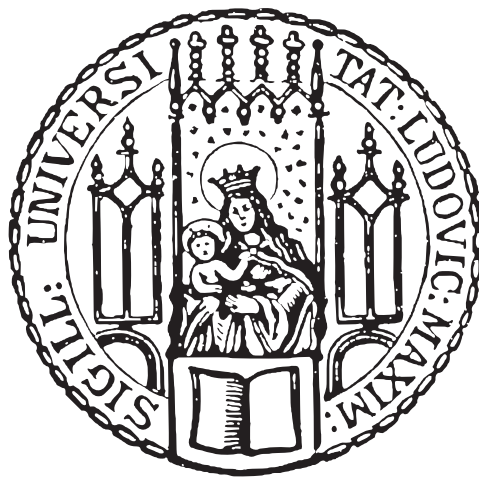


---

# A Rydberg Tweezer Platform with Potassium Atoms

---

Dissertation an der Fakultät für Physik  
Ludwig-Maximilians-Universität München



vorgelegt von

**Nikolaus Lorenz**

aus Hanau

München, den 1. Februar 2021

Tag der mündlichen Prüfung: 29. März 2021

Erstgutachter: Prof. Dr. Immanuel Bloch

Zweitgutachter: Prof. Dr. Rudolf Gross

---

## Zusammenfassung

Quantensimulationen bieten die Möglichkeit quantenmechanische Probleme zu untersuchen, welche auf klassischen Computern nicht berechenbar sind. Diese Arbeit stellt eine neue Plattform für Quantensimulationen vor und präsentiert die erste experimentelle Realisierung einzelner Kaliumatome in optischen Dipolfallen. Wechselwirkungen zwischen einzelnen neutralen Atomen werden durch die starken Energieverschiebungen von Zuständen mit großer Hauptquantenzahl verursacht, sogenannte Rydberg-Zustände. Wechselwirkungen können dabei entweder durch eine direkte Anregung in Rydberg-Zustände oder eine verstimte optische Kopplung, so genanntes ‚Rydberg dressing‘, erzeugt werden. Wir begründen, warum insbesondere Kalium für die Implementierung von ‚Rydberg dressing‘ geeignet ist und insbesondere durch das gleichzeitige Koppeln beider Grundzustände das Erzeugen komplexer Wechselwirkungen ermöglicht.

Kaliumatome werden mittels Laserkühlung abgebremst, gefangen und anschließend werden einzelne Atome in optischen Dipolfallen geladen. Zudem reduziert Raman Seitenbandkühlung die Schwingungsanregungen in den Fallenpotentialen und kühlt die Atome fast zum Bewegungsgrundzustand. Diese Kühltechnik ermöglicht ‚Rydberg dressing‘, welches ansonsten durch thermische Verbreiterung und inhomogenen Fallenpotentiale limitiert wäre. Um Atome direkt in Rydberg-Zustände anzuregen, wird ein Lasersystem mit zwei resonanten Frequenz Verdopplungsstufen aufgebaut, mit welchem bis zu einem Watt ultravioletten Lichts bei 286 nm erzeugt wird. Durch Anregung von Atomen in Rydberg-Zustände beobachten wir Rabi-Oszillationen mit Rabi-Frequenzen von bis zu 1 MHz, was eine kohärente Kontrolle der Rydberg-Atome demonstriert.

Zuletzt kombinieren wir diese Techniken, um Wechselwirkungen auf zwei verschiedene Arten zu beobachten: Erstens erzeugen wir durch direkte Anregung und Rydberg-Blockade ein sogenanntes ‚Superatom‘ aus bis zu vier einzelnen Atomen und beobachten kohärente Oszillationen zu diesem kollektiven Zustand. Wir messen die erwartete Skalierung der effektiven Rabi-Frequenz mit der Wurzel der Anzahl der Atome und bestätigen die Erzeugung eines Quantenverschränkten Zustands. Zweitens induzieren wir Wechselwirkungen zwischen Atomen durch optische Beimischung mittels ‚Rydberg dressing‘, die in einer eindimensionalen Kette optischer Dipolfallen gefangen wurden und messen korrelierte Wechselwirkungen über Distanzen von mehreren Fallenplätzen.

Zusammenfassend haben wir eine Plattform für die Quantensimulation mittels einzelner Atome in optischen Dipolfallen entwickelt. Die vorgestellten Ergebnisse zeigen eine kohärente Kontrolle einzelner Atome und Wechselwirkungen, die durch Rydberg-Zustände induziert werden. Wir zeigen damit, dass das System für die Quantensimulation von Vielkörpersystemen gut geeignet ist.



## Abstract

Quantum simulation offers the possibility to study quantum mechanical problems which are untraceable on classical computers. This thesis introduces a novel platform for quantum simulation and presents the first experimental realisation of single potassium atoms trapped in optical tweezers. Interactions between individual atoms are induced by strong energy shifts of atoms excited to states with large principal quantum number, so-called Rydberg states. Either direct excitation to Rydberg states or off-resonant dressing can be used to induce these interactions. We argue that potassium is well-suited for the implementation of Rydberg dressing, enabling simultaneous dressing of both ground states to engineer complex interactions.

Using techniques to cool and trap cold atoms, single potassium atoms are prepared in arrays of optical tweezers. Raman sideband cooling reduces vibrational excitations and prepares the atoms close to the motional ground state. This cooling technique mitigates severe limitations for Rydberg dressing, arising from thermal broadening and inhomogeneous light shifts in the array of atoms.

To directly excite atoms to Rydberg states, a high power laser setup with two cavity-enhanced frequency doubling stages is constructed, generating up to one Watt of ultra-violet light at 286 nm. By exciting atoms to Rydberg states we observe Rabi oscillations with Rabi frequencies of up to 1 MHz, demonstrating coherent control of Rydberg atoms.

Finally, we combine these techniques to observe interactions in two ways: First, we create a so-called superatom of up to four individual atoms using direct excitation and Rydberg-blockade and observe coherent oscillations to this collective state. We measure the expected square root scaling of the effective Rabi frequency with the number of individual atoms, confirming the creation of a many-body entangled state. Secondly, we off-resonantly dress the atoms prepared in a one-dimensional chain and measure correlated interaction shifts over multiple sites.

In summary, we have developed a platform for quantum simulation with single atoms in optical tweezers. The presented results show coherent control of single atoms and interactions induced by Rydberg states. We have thus demonstrated that the system is well-suited for quantum simulation of many-body systems.



## Contents

<b>1</b>	<b>Introduction</b>	<b>1</b>
<b>2</b>	<b>Rydberg physics with optical tweezers</b>	<b>5</b>
2.1	Rydberg atoms	5
2.2	Why potassium?	7
2.2.1	Advantages of a small fine structure splitting	7
2.2.2	Advantages of a small ground state splitting	9
2.2.3	Excited state shifts	9
<b>I</b>	<b>A potassium optical tweezer platform</b>	<b>11</b>
<b>3</b>	<b>Experimental apparatus</b>	<b>13</b>
3.1	Vacuum chamber	13
3.1.1	Potassium oven	13
3.1.2	Zeeman slower	15
3.1.3	Main chamber	15
3.1.4	Objective	17
3.1.5	In-vacuum coils	17
3.1.6	Compensation coils	19
3.1.7	Electrodes	20
3.2	Lego optics mounts	20
3.3	MOT setup	21
3.3.1	MOT laser	21
3.3.2	Optical setup	23
3.3.3	Zeeman slower	25
3.3.4	Imaging laser	25
3.3.5	Characterisation	26
3.4	Grey molasses cooling	28
3.4.1	Grey molasses laser	28
3.5	Dipole trap	29
<b>4</b>	<b>Single atoms in tweezers</b>	<b>31</b>
4.1	Optical setup and SLM	31
4.2	Loading and imaging single atoms	33
4.2.1	Tweezer arrays	35
4.2.2	Atom lifetime	35

4.3	State preparation . . . . .	37
4.4	Trap depth measurement . . . . .	40
4.5	Raman sideband cooling . . . . .	41
4.5.1	Experimental setup . . . . .	42
4.5.2	Experimental sequence . . . . .	44
4.5.3	Sideband spectroscopy . . . . .	44
4.6	Rampdown . . . . .	46
4.6.1	Measuring the survival probability after rampdown . . . . .	46
4.6.2	Simulating the survival probability after rampdown . . . . .	47
4.7	Switchoff . . . . .	48
4.8	Driving ground state transitions . . . . .	50
4.8.1	Laser setup . . . . .	50
4.8.2	Characterisation . . . . .	51
<b>II</b>	<b>Rydberg atoms</b>	<b>55</b>
<b>5</b>	<b>UV laser system</b>	<b>57</b>
5.1	Seed laser . . . . .	57
5.2	Reference cavity . . . . .	58
5.3	From the IR to the UV . . . . .	61
5.3.1	Theory of frequency doubling . . . . .	61
5.3.2	Experimental setup and SHG stages . . . . .	67
5.3.3	Characterisation . . . . .	70
5.3.4	Linewidth and phase noise . . . . .	72
5.4	Optical setup for the UV light . . . . .	73
5.5	Rydberg spectroscopy . . . . .	75
5.5.1	Electric field spectroscopy . . . . .	76
5.5.2	Linewidth and thermal broadening . . . . .	77
<b>6</b>	<b>Interacting Rydberg systems</b>	<b>81</b>
6.1	Single-atom Rabi oscillations . . . . .	81
6.1.1	Decay of coherent oscillations . . . . .	83
6.2	Rydberg blockade and superatom . . . . .	89
6.3	Rydberg dressing . . . . .	93
6.3.1	Theory of Rydberg dressing . . . . .	93
6.3.2	Dressed interactions . . . . .	96
<b>7</b>	<b>Conclusion and outlook</b>	<b>101</b>
7.1	Conclusion . . . . .	101
7.2	Outlook . . . . .	102
<b>A</b>	<b>Potassium 39 level scheme</b>	<b>105</b>
A.1	Light shifts of the excited states . . . . .	106

---

<b>B Histograms and discrimination for single tweezers</b>	<b>109</b>
<b>Danksagung</b>	<b>111</b>
<b>References</b>	<b>111</b>



## Chapter 1

### Introduction

The techniques for slowing and cooling atoms from several hundred to below one thousandth of a Kelvin and for trapping the cold atoms, developed in the 1980s, started the field of cold atomic physics [1, 2]. The development of additional techniques in the 90s, such as evaporative cooling, advanced the field further by reaching record low temperatures and enabling the realisation of novel states of matter, such as Bose-Einstein-condensates or degenerate Fermi gases [3–5]. Rapid advances allowed measuring and controlling individual atoms, a possibility that just a few decades before was considered unachievable by Erwin Schrödinger [6]. This control enabled the study of fundamental and puzzling aspects of quantum mechanics and additionally pushed the records of precision measurements [7, 8]. Today, newest generations of clocks using cold atoms, together with trapped ions, are the most precise frequency standards in the world, even being able to observe effects of relativity in a laboratory.

To trap cold atoms, a variety of techniques was developed over the years. One such technique uses laser light in optical dipole traps and optical lattices [9]. These are a standard in cold atom experiments nowadays, used to engineer potentials and study quantum-mechanical problems. One impressive advance of the field are quantum gas microscopes. Here, quantum systems made of perfectly arranged single atoms are created using optical lattices and used to study problems of quantum mechanical many-body systems [10–14]. High optical resolution enables precise manipulation and reliable detection of every individual atom. Using optical lattices, atoms can tunnel between individual sites, enabling quantum simulation of many-body problems, realising the dream of Richard Feynman of simulation quantum mechanics using quantum systems [15]. The supreme control, accessible time scales and increased length scales make these systems perfect for quantum simulation of solid state systems, that cannot directly be observed or manipulated with this precision.

Disadvantages of quantum gas microscopes are the relatively long cycle times of tens of seconds and expensive and intricate experimental setups. In recent years, new techniques to generate arrays of single atoms have gained increasing interest. Instead of optical lattices, arrays of tightly focussed optical beams are used to trap and manipulate single particles. This ‘bottom-up’ approach enables direct loading of single atoms, which not only reduces the experimental resources needed, but further makes fast cycle times well below one second possible, enabling measurements with good statistics. By employing spatial light modulators, atoms can be prepared in arbitrary one-, two- or even three-dimensional geometries [16–18]. Control of individual atoms allows for arranging them, creating per-

fectly filled flexible geometries [19–21].

In contrast to optical lattices, tunneling in optical tweezers has not been realized so far on larger scale systems [22, 23]. In order to investigate many-body physics, interactions between particles can instead be implemented using Rydberg states, which are states with a large principal quantum number. Due to their large dipole moment, long-range interactions between Rydberg atoms can be induced. Typical distances of atoms in optical tweezer arrays on the order of several micrometers and strong interaction shifts of Rydberg atoms on the same length scale make Rydberg atoms a perfect fit to induce interactions in optical tweezer systems. This enables quantum simulation of spin systems and together with the high fidelity control of Rydberg states that was achieved over the last years, makes this platform a promising candidate for large-scale quantum simulation and computing [24–39]

A variety of different schemes exist which utilise the properties of Rydberg atoms to induce interactions in cold atomic systems. Direct excitation to the Rydberg state, for example, allowed the realisation of quantum magnets and studies of topological ordering [36, 39]. The deterministic generation of entanglement between atoms in the context of quantum gates has also been studied [28, 34].

Another interesting scheme is Rydberg dressing, where the Rydberg state is off-resonantly coupled to a ground state, admixing only a small part of the interacting Rydberg character to the ground state atoms. This allows engineering of interactions to study a variety of quantum many-body systems. Rydberg dressing was used, for example, to realise Ising quantum magnets or quantum gates [40–43].

This work describes a novel experiment, trapping potassium atoms in optical tweezers to enable studies of quantum many-body systems, using Rydberg dressing as a resource for engineered long-range interactions. This work presents the first realisation of cold potassium atoms, trapped in optical tweezers. Potassium features a small ground state energy splitting that allows for easy implementation of simultaneous Rydberg dressing of both ground states, called double dressing [44]. This enables, for example, the study of frustrated quantum magnets. Fast cycle times will enable experiments with high statistics which are not feasible in optical lattice setups.

---

## Outline

This thesis is structured as follows:

In the first part, the experimental setup for the generation of large arrays of single potassium atoms is introduced.

In [Chapter 2](#), a short introduction to Rydberg physics in the context of quantum simulation with single trapped atoms is presented. We also discuss the advantages of potassium for such systems.

In [Chapter 3](#) the experimental apparatus that was designed and built during the work of this thesis is introduced. We discuss all relevant parts like the vacuum setup and the lasers used to cool and trap atoms.

Lastly, in [Chapter 4](#) the generation of arrays of optical tweezers is presented and the traps are characterised. We introduce techniques to prepare atoms in a defined quantum state and cool them close to their motional ground state. Raman transitions are used for coherent ground state control, completing the experimental toolbox for trapping and manipulation of arrays of single potassium atoms.

The second part focusses on excitation to Rydberg states and the use of such states to implement long-range interactions.

In [Chapter 5](#), the high power laser system for Rydberg excitation with ultra-violet light is introduced, starting from the seed laser and a discussion of the two cavity enhanced non-linear frequency doubling stages. We perform spectroscopy of Rydberg states as a first characterisation of the system.

In [Chapter 6](#), coherent Rabi oscillations between ground and Rydberg states are presented. We discuss imperfections and limitations and compare those to simulations. Rydberg blockade is used to induce interactions between atoms, the first realisation of an interacting many-body system in our setup. Lastly, the first experimental results of Rydberg dressing are presented.

## Publications

The following articles have appeared in the context of this thesis:

***Raman Sideband Cooling in Optical Tweezer Arrays for Rydberg Dressing***

Nikolaus Lorenz, Lorenzo Festa, Lea-Marina Steinert, Christian Gross

[SciPost Phys. 10, 052 \(2021\)](#)

***Motion assisted facilitated excitation of Rydberg atoms in optical tweezers***

Lorenzo Festa, Nikolaus Lorenz, Lea-Marina Steinert, Zaijun Chen, Philip Osterholz, Robin Eberhard, Christian Gross

[arXiv:2103.14383 \(2021\)](#)



---

## Chapter 2

### Rydberg physics with optical tweezers

Optical tweezers have gained increasing interest over the last year, as they are a promising platform for large-scale quantum simulation and quantum computation. To put the work of this thesis into context with the current advances in the field, we discuss different approaches of optical tweezer platforms and then introduce Rydberg atoms as a way to induce many-body interactions between atoms. We focus on the choice of potassium since this work presents the first demonstration of single potassium atoms in optical tweezers. For the first demonstration of optical tweezers for single atom trapping and imaging, a single Gaussian beam was focussed using a lens with high numerical aperture, creating a single trap [45]. Light assisted collisions cause parity projections, allowing for efficient preparation of single atoms with a probability of about 50 % [46]. Using additional techniques the energy gain in such collisions can be controlled, increasing the loading probability of single atoms up to 90 % [47–49]. To generate arrays of optical traps, a variety of techniques has been demonstrated: Acousto optical deflectors (AODs) [19, 50], spatial light modulators (SLMs) [16–20], digital mirror devices (DMD) [51] and micro-lens arrays (MLAs) [21] have successfully been used. To create arrays with near unity filling, AODs can be used to sort atoms. In 1D they can be used simultaneously for generation of the array and sorting, in two dimensions often SLMs for generation of arbitrary patterns and AODs for arranging of atoms are used in combination [19–21]. In an alternative approach sorting of atoms by dynamically changing the pattern of the SLM has been demonstrated, but is so far limited by computational resources [17].

These advances have for example enabled quantum simulation of Ising chains, studies of the Su-Schrieffer–Heeger (SSH) model, observation of topologically protected edge states and studies of quantum scars [28, 36, 39, 52, 53]. While most of these experiments have been performed with alkali atoms, mainly rubidium and caesium, in the last years trapping and control of alkaline earth atoms in optical tweezer arrays has also been demonstrated [32, 54, 55]. Recently quantum simulators with hundreds of atoms in fully programmable arrays and strong interactions have been demonstrated, showing the rapid advances in the field [52, 56, 57].

#### 2.1 Rydberg atoms

Rydberg states are states with large principal quantum number  $n$ . Rydberg atoms are used and studied not only in the context of optical tweezers, but also in bulk systems [43, 58–61], optical lattices [62–64], ions [65] or even solid state systems [66]. Here, we want to

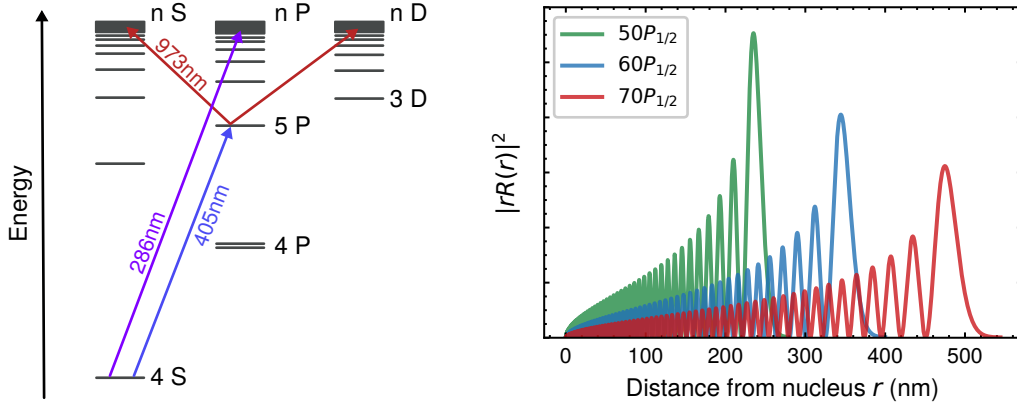


**Fig. 2.1** **Left:** Level scheme of potassium (energy axis to scale) with the direct one-photon excitation scheme and two-photon excitation scheme via the intermediate  $5P$  state, indicated by arrows. The individual transitions are marked with the wavelength for excitation of  $n = 60$  Rydberg states. **Right:** Radial wave function  $r|R(r)|^2$  of different Rydberg states, illustrating the drastically increased size of Rydberg atoms. For comparison, the ground and first excited states  $4S$  and  $4P$  wave functions have a radial extent on the order of 1 nm.

introduce the properties and scalings of alkali Rydberg atoms, where the exaggerated properties such as a large extent of the electron wave function and large dipole moments cause long range interactions over micrometer scales. The choice of principal quantum number and angular momentum enables to tune these interactions both in strength and angular dependence [67, 68]. Interactions between Rydberg states can be induced either via long range dipole-dipole interactions with an  $1/r^3$  scaling or the van-der-Waals (vdW) interaction with a  $1/r^6$  scaling, where  $r$  denotes the interatomic distance. A detailed discussion of Rydberg atoms can be found in References [69, 70].

Rydberg atoms have one electron in a high-lying energy state, which makes their behaviour and description similar to that of the well-know hydrogen atom. In contrast to the hydrogen atom, where the atomic core is simply one proton, for alkali atoms the the small wave function overlap of low angular momentum states with the ionic core has to be taken into account. The binding energies  $E$  can then be described with the quantum defect  $\delta_{nlj}$  as

$$E_{n^*} = -\frac{R_\infty}{(n - \delta_{nlj})^2} = -\frac{R_\infty}{n^{*2}}. \quad (2.1)$$

For potassium and  $n = 62$  the quantum defects are  $\delta_S = 2.18$ ,  $\delta_P = 1.71$  and  $\delta_D = 0.28$  for the S, P and D states. For  $F$  and all higher angular momentum  $l$  states the quantum defect is  $\delta_{l \geq 3} < 0.01$ , due to the low overlap of high angular momentum states with the core. For high principal quantum numbers the defects  $\delta$  can be assumed slowly varying with  $n$ . Using the effective quantum number  $n^* = n - \delta_{nlj}$ , the properties of Rydberg atoms can be described, as shown in Table 2.1.

To excite alkali atoms to Rydberg states, either the direct transition in the UV or a two-

Property	Symbol	Scaling	value for $4P_{3/2}$	value for $62P_{3/2}$
Binding energy	$E_n$	$n^{-2}$	4.34 eV	3.74 meV
Level spacing	$E_{n+1} - E_n$	$n^{-3}$	350 THz	29 GHz
Coupling to $4S_{1/2}$	$\langle 4S d nP \rangle$	$n^{-3/2}$	5 ea <sub>0</sub>	0.001 ea <sub>0</sub>
Lifetime (T = 0 K)	$\tau$	$n^3$	26 ns	841 $\mu$ s
Lifetime (T = 300 K)	$\tau_{BB}$	$n^2$	26 ns	162 $\mu$ s
vdW coefficient	$C_6$	$n^{11}$	-	-116 GHz $\cdot$ $\mu$ m <sup>6</sup>

**Tab. 2.1** Properties of Rydberg states and scaling laws. Values are given for the first excited state  $4P$  and the Rydberg state  $62P$  for potassium. For the Rydberg state the lifetime  $\tau$  is reduced due blackbody radiation, which couples transitions to other nearby Rydberg states. All properties were calculated with the python package ‘alkali rydberg calculator’ ARC [71].

photon transition can be used. Higher-order multi-photon transitions have also been demonstrated, but are not commonly used [72]. In Fig. 2.1 the level scheme for potassium with the direct transition in the UV and one possible two-photon transition is shown. One advantage of the two-photon excitation scheme are the experimentally easily accessible wavelengths. Due to angular momentum selection rules both  $S$  and  $D$  states can be addressed. Besides the high achievable Rabi frequencies, Doppler shifts can be partially cancelled in counter-propagating configurations. However, scattering caused by the intermediate state reduces the effective lifetime of the Rydberg state. The direct excitation scheme enables addressing of  $P$  states, but is technically more challenging due to the low wavelength radiation. This also limits achievable Rabi frequencies. Since no scattering at an intermediate level occurs, this scheme is advantageous for experiments of Rydberg dressing, where the Rydberg state lifetime limits the maximal interaction time scales. Hence Rydberg dressing experiments are usually performed with the direct excitation scheme [42, 43, 64, 73, 74].

## 2.2 Why potassium?

Next, we take a look at our choice of element. While a variety of elements are used for cold atom and optical tweezer platforms, this work is the first demonstration of potassium atoms trapped in optical tweezers. The main differences, especially to the commonly-used elements rubidium and caesium, are the smaller fine and hyperfine splittings.

These properties of potassium pose difficulties for the implementation of cooling schemes such as optical molasses, grey molasses and evaporative cooling [12, 75–78]. However, those can be solved, allowing us to capitalize on the advantages of the smaller level splittings, which we now discuss.

### 2.2.1 Advantages of a small fine structure splitting

We first look at the effect of the fine structure splitting of the first two excited states, in our case  $4P_{1/2}$  and  $4P_{3/2}$ , for optical tweezer experiments.

To create optical tweezers, trapping light is strongly focussed down to a waist on the order

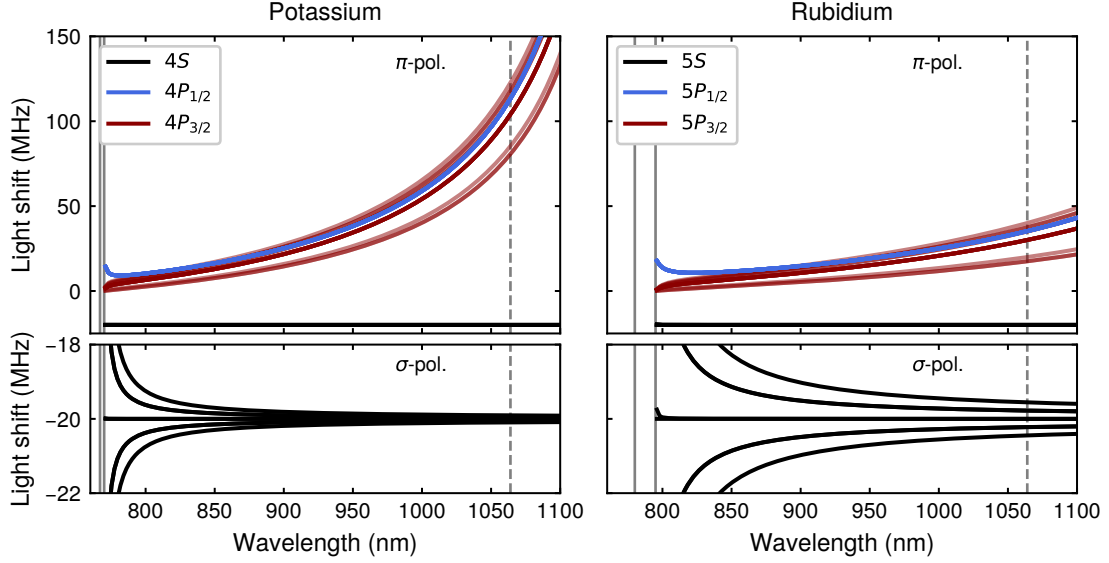


**Fig. 2.2** Comparison of the light shifts for ground and excited states for potassium (**left**) and rubidium (**right**): Light shifts of all  $m_F$  hyperfine states of the ground and first excited state manifolds as a function of the trap wavelength for an optical tweezer with a waist of  $1 \mu\text{m}$ . For each wavelength the optical power is chosen such that the shift of the  $F = 2m_F = 0$  ground state is constant at  $-20 \text{ MHz}$  ( $\approx 1 \text{ mK}$ ). **Top:** Ground and excited state shifts for linear polarisation. Vertical solid grey lines indicate the resonances of the D1 and D2 transitions, the trapping wavelength of  $1064 \text{ nm}$  that we use is indicated by a grey dashed line. **Bottom:** Ground state shifts for circular polarisation cause splitting of the  $m_F$  levels and fictitious magnetic fields in tight optical traps.

of  $1 \mu\text{m}$ . Usually, linearly polarised light is used. Due to the strong focussing, light that is off-centre at the position of the waist acquires some degree of circular polarisation. Since circularly polarised light causes differential light shifts of the ground state  $m_F$  states, this polarisation gradient over the optical tweezer has the same effect as a magnetic field gradient. Hence those shifts are often called ‘fictitious magnetic fields’ and can be used to mimic the effects of strong and local magnetic fields. In optical tweezers this is undesired, as it limits coherent manipulation and cooling [79, 80].

While the polarisation gradient is caused by the fact that light is strongly focussed, the effect on the ground state shift depends on the level structure of the atom and the wavelength of the trapping light. The vector light shift  $V_{\text{vec}}$  is

$$V_{\text{vec}}(r) = -V(r) \frac{\delta_2 - \delta_1}{\delta_2 + 2\delta_1} \mathbf{C}(r) \cdot g_F \mathbf{F} \quad (2.2)$$

where  $\delta_1$  and  $\delta_2$  are the detunings from the D1 and D2 line,  $U$  is the scalar dipole trap potential and  $\mathbf{C}$  quantifies the direction and degree of ellipticity of the light, with  $|\mathbf{C}| = 1$  for circular and  $|\mathbf{C}| = 0$  for linear polarisation [79].  $\mathbf{F}$  is the total angular momentum operator. A smaller fine structure splitting  $\delta_2 - \delta_1$  thus reduces the vector light shifts. For potassium

this splitting is 1.5 THz, a factor of 5 smaller compared to the often-used rubidium with 7.4 THz. The effect of differential splittings of the ground state levels as a function of trap wavelength is shown in Fig. 2.2 for potassium and rubidium. This makes potassium a good choice for the implementation of ground state qubits with coherent ground state control at high fidelity.

### 2.2.2 Advantages of a small ground state splitting

So far we have looked at the effects of a small fine structure splitting. Here, we discuss the advantage of the hyperfine splitting of  $^{39}\text{K}$  of  $\Delta_{\text{HFS}} = 462$  MHz. This splitting can be bridged well by commercially available acousto-optic-modulators (AOMs). While this is convenient for the setups used for molasses, gray molasses and Raman sideband cooling, it becomes very important for more complicated setups such as the high power UV laser used for direct Rydberg excitation. Theoretical proposals introduced the idea of so-called ‘double dressing’, where two UV fields are used to couple the  $F = 1$  and  $F = 2$  ground states simultaneously to Rydberg states [44]. Using two AOMs, this can be conveniently realised with potassium. Elements like rubidium or caesium with splittings of several GHz would require significantly more complex setups. Note that  $^{41}\text{K}$  with  $\Delta_{\text{HFS}} = 254$  MHz would also allow for this scheme.

While lithium features small level splittings of both fine and hyperfine structure, it causes difficulties for cooling and trapping due to its low mass. In addition, the transition for direct Rydberg excitation with 230 nm is considerably lower than for potassium, making it more difficult to construct a high power laser system. The same is the case for sodium with its transition at 240 nm. This makes potassium the best choice for our implementation of Rydberg dressing in optical tweezers.

### 2.2.3 Excited state shifts

For optical dipole traps the choice of the trapping wavelength affects the experiment in multiple ways. The trap depth  $V_0$  scales as  $U_0 \propto \Delta^{-1}$  and the off-resonant scattering rate  $\Gamma$  as  $\Gamma \propto \Delta^{-2}$ . Far detuned traps are thus desirable for low heating rates and long atom lifetime in traps [9]. Additionally, traps with a closer detuning cause stronger differential shifts of the  $m_F$  ground states, as discussed above.

A common choice in many cold atom experiments is a wavelength of 1064 nm for the optical dipole trap, since high power lasers up to 100 W are commercially available and the wavelength is far detuned for all alkali elements, reducing the scattering rate.

One challenge when working with a trap wavelength of 1064 nm for potassium is the strong anti-trapping of the excited  $4P$  states, used for cooling and imaging. This is caused by the  $4P_{1/2} \leftrightarrow 3D$  and  $4P_{3/2} \leftrightarrow 3D$  resonances at 1170 nm and 1178 nm. The strong light shifts close to those resonances are shown in Fig. 2.2. The excited states are anti-trapped by a factor of about 6 compared to the ground state light shift. Exact values for all excited states are given in Appendix A.1.

These strong shifts prevent direct laser cooling of potassium atoms in optical tweezers, an issue which can be solved by chopping the trapping and cooling light, as described in

[Section 4.2 \[81\]](#). The strong light shifts further pose challenges for the implementation of Raman sideband cooling, where the anti-trapping causes heating while repumping the atoms. This can be solved by careful choice of detunings and was successfully implemented for quantum gas microscopes and is described in [Section 4.5](#) for our setup [12].

In summary, established techniques for cooling and trapping atoms or Raman sideband cooling for potassium can be used. The smaller level splittings are advantageous for reduced vector shifts of the traps and enable the construction of a high power UV setup for Rydberg dressing or ‘double dressing’ schemes. This enables engineering of complex interactions between atoms and perform quantum simulation of, for example frustrated quantum magnets [30, 44, 82–89].

## **Part I**

# **A potassium optical tweezer platform**



---

## Chapter 3

### Experimental apparatus

The following chapter describes the experimental setup, which was developed and built during the work of this thesis. We build on the well established techniques for laser cooling and trapping. A general discussion can be found in References [90–92]. A detailed discussion regarding the exact implementation for potassium is given in References [75, 76, 93] for trapping and sub-doppler molasses cooling and in References [77, 78] for grey molasses cooling.

First, the experimental setup to trap and cool atoms is introduced, starting with the vacuum chamber in Section 3.1. Then the laser for both magneto-optical trap and Zeeman slower is described in Section 3.3. Grey molasses cooling is used to further cool the atoms to sub-Doppler temperatures, described in Section 3.4. The MOT and Zeeman slower setup as well as the GM setup are described in detail in the thesis of Marcel Duda [94] for an earlier stage of the experimental setup. A dipole trap with a single focussed beam is described in Section 3.5. This is used for first characterisations of the system and allows for single shot optimisation of experimental parameters.

#### 3.1 Vacuum chamber

The main chamber of the vacuum system is one of the central elements of the experiment. It is one of the first parts that has to be planned when setting up a new experiment and cannot be changed later. The design needs to be flexible and allow for a variety of possibilities, as the setup is intended to remain unchanged beyond the scope of this PhD thesis. In addition to optical tweezers the setup was designed to allow for optical lattices in all three dimensions and evaporative cooling using Feshbach resonances. The main goal when designing the experiment was to have just one vacuum chamber without transport of the atoms, to allow for a fast cycle time on the order of one Hertz rather than tens of seconds, which is a typical time for state of the art quantum gas experiments. In the following we will first look at the potassium oven and the Zeeman slower and then take a detailed look at the main chamber.

##### 3.1.1 Potassium oven

The first part of the vacuum chamber, as shown in Fig. 3.1, can be divided in two parts: First, the oven itself which is attached to a pumping chamber with a cooled copper shield,

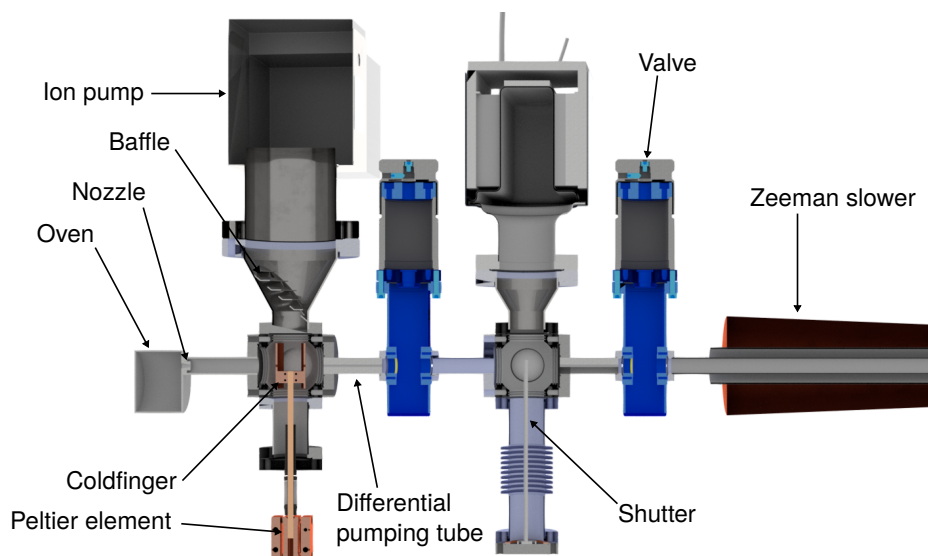


**Fig. 3.1** First part of the vacuum chamber: The oven (left) is attached to a first chamber with a cooled copper shield, called the coldfinger, to reduce the vapour pressure. To protect the ion pump a baffle blocks the direct line of sight into the pump. A differential pumping tube connects to a second chamber with a mechanical shutter, which is used to block the atomic beam. A second differential pumping stage then connects to the Zeeman slower. Both pumping chambers can be separated with in-line valves.

the coldfinger, and a second pumping chamber with a mechanical shutter. Both chambers are separated by a differential pumping tube and valve. A second differential pumping tube and valve connect this part to the Zeeman slower.

The oven follows a simple design and is made of a short stainless steel tube with an outer diameter of 40 mm. We filled the oven with 20 g of potassium<sup>1</sup>. The oven was filled in an argon-fluxed glove box to prevent oxidation of the potassium sample. An inset with a 3 mm diameter hole, called the nozzle, is mounted at the front of the oven tube. We heat the nozzle to 90 °C to prevent clogging, but due to the insulation, the whole oven heats up to  $\approx 80$  °C.

As many other groups already reported problems of failing ion vacuum pumps due to high vapour background pressure of alkali atoms, several safety measures were taken to prevent this [95]. The first pump used has a special design<sup>2</sup> where the pumping filaments are not oriented towards the flange of the pump. In addition, a baffle between the chamber and the pump blocks the direct line of sight towards the pump.

To reduce the vapour pressure directly, a copper shield with two 3 mm holes is installed directly after the oven. The whole copper part is connected to a high current copper feed-through, acting as a thermal connection to the outside of the vacuum chamber. On the outside, a water-cooled peltier element is attached to the feed-through, cooling the whole

<sup>1</sup>STREM chemicals, potassium (99.95%), in a pre scored ampoule

<sup>2</sup>Varian classic style VA-060-DD-M from Duniway

shield to  $-5^{\circ}\text{C}$ .

A 65 mm long differential pumping tube with a diameter of 3 mm connects to the next chamber. Due to the bad experience with rotational shutters, which failed and got stuck after some time of operation [96], we installed a simple bellow with a long metal rod as a mechanical shutter of the atomic beam. The bellow is pushed a few millimetres by a pneumatic piston. This design proved to work reliably over long times in other experiments [95]. However, it proved not to be necessary to operate the shutter for normal operation of the experiment.

### 3.1.2 Zeeman slower

To slow down the atoms exiting the oven, we use a spin-flip Zeeman slower. Having a non-zero field at the end of the slower ensures that the laser is not resonant with atoms inside the MOT. A Zeeman slower has several advantages compared to direct loading from the background or loading from a 2D MOT: The long distance separates the oven section from the main chamber, saving space for the optics close to the chamber and keeping the hot oven separated from temperature sensitive optics. A slower is also relatively easy in design and alignment, with only a single power supply needed and only one beam having to be aligned. The design of the slower is described in detail in the thesis of Marcel Duda [94]. The slower has two parts, one large coil for the decreasing field and two small coils for the spin flip region. The largest field at the entrance of the slower is 320 G. With a laser detuning of 205 MHz the capture velocity is  $\approx 350$  m/s. This is comparable to the mean velocity of the atoms exiting the oven of 450 m/s.

The slower is wound onto a 40 mm diameter non-magnetic stainless steel tube using a 4 by 3 mm rectangular hollow copper wire with an inner diameter of 2.1 mm. Each layer is glued<sup>3</sup> and isolated with Kapton tape. The decreasing field part is divided into 5 layers of roughly equal length. The tubes of each block are electrically connected to form one coil, but separated for the water cooling to allow for sufficient flow<sup>4</sup>. The two smaller blocks are wound using two separate tubes.

In contrast to the description in [94], we do not use the two smaller coils of the spin-flip region any more. It turned out that the field of the MOT coils is strong enough to also act as the spin flip part of the slower. Since the Zeeman slower does not cool the transverse velocity components, the slow atoms will diverge quickly when exiting the slower. The shorter the distance between slower and MOT, the less critical this effect is. Using the MOT coils as final part of the slower thus allows for an efficient capture of slowed atoms in the MOT.

### 3.1.3 Main chamber

The main chamber is not only the central part of the vacuum system, but of the whole experiment. Many parts such as the magnetic coils, the objective and the electrodes are

---

<sup>3</sup>Polytec Duralco 128

<sup>4</sup>The on-line calculator [www.druckverlust.de](http://www.druckverlust.de) is very useful for quick checks of flow and pressure drop when setting up water cooling in the lab.

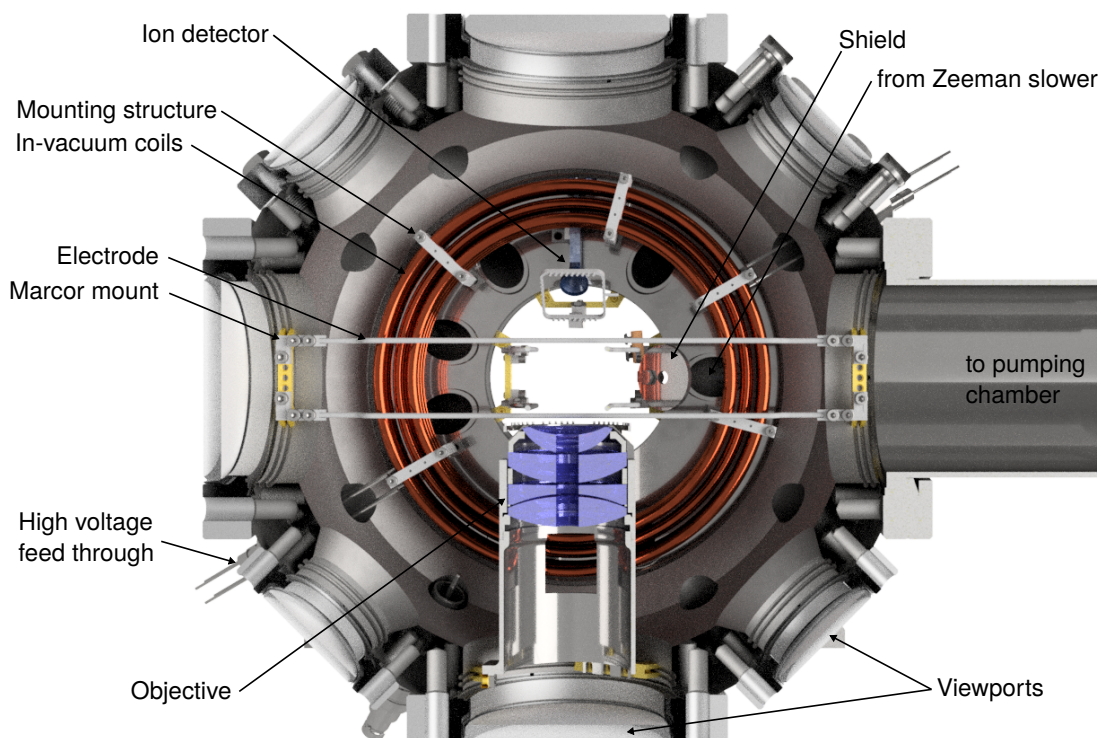


**Fig. 3.2** Cut through the main vacuum chamber. The focus of the objective is the center of the chamber. A shield with a 5 mm hole prevents coating of the objective with potassium. Eight electrodes are placed with a spacing of approximately 2 cm. The water-cooled in-vacuum coils are mounted on two CF 160 flanges. Six CF 63 and four CF 40 viewports allow for optical access. Twelve CF 16 viewports allow for additional access from various angles. Not shown are two RF coils and the pumping chamber with a titanium sublimation and ion pump.

placed inside this steel chamber<sup>5</sup>, as shown in Fig. 3.2. A pumping chamber with CF 63 flanges is attached at roughly 45 degrees to the Zeeman slower. A titanium sublimation pump on a CF 100 flange as well as an ion pump on a CF 63 flange are attached to this pumping chamber.

Using a steel chamber, compared to glass cells, has the advantage of large distances to dielectric surfaces, which can have patch charges. This is important for experiments using Rydberg atoms which are sensitive to electric fields.

To allow for fast experimental cycles the atoms are not transported, such that oven, Zeeman slower and focus of the objective are aligned. The alignment was tested during the assembly of the vacuum system using a reference laser beam.

All main components such as the high resolution objective, the high-current coils and the electrodes are mounted in-vacuum. Additionally, two small RF antennas and an ion detector<sup>6</sup> are mounted inside the chamber, but have not been used so far. An ion detector

<sup>5</sup>Kimball MCF800-SphSq-G2E4C4A16

<sup>6</sup>SJUTS KBL 10RS/45

allows for direct detection of ionised Rydberg atoms or in combination with electric fields also for state sensitive ionisation spectroscopy [97–99].

The chamber has six CF63 viewports, two per main axis. Four CF 40 viewports allow for a diagonal access on 45 degrees in the x-z plane. All of these viewports are anti-reflection (AR) coated for the following wavelengths: 285 to 290 nm for the single-photon Rydberg transitions, 405 and 985 nm for the inverted two-photon excitation scheme via the  $5P$  state, 750 to 775 nm for the D1 and D2 line and 1064 nm for the dipole traps and tweezers. The glass itself is tilted inside the flanges by 0.5 degrees to prevent interference from back-reflections.

Twelve small CF16 viewports with AR coatings for 1064 and 532 nm allow for bi-chromatic square lattices in the x-y plane and vertical confinement in the z direction, but were not used for the experiments described in this thesis.

### 3.1.4 Objective

The objective<sup>7</sup> is one of the central elements, used both for generation of the tweezer traps as well as for single-atom imaging. The objective is mounted inside the vacuum chamber. The numerical aperture is 0.6 with an effective focal length of 33 mm and a working distance measured from the front surface of the mount to the focus of 16.75 mm. The objective is designed and coated for diffraction limited performance at 767 nm and 1064 nm. The performance was measured by the manufacturer with a Strehl ratio of 0.69, which is the ratio of measured to ideal peak intensity of a diffraction limited spot.

The special feature of the objective is a 8 mm diameter central hole through the whole objective. So far this hole has been used for the vertical MOT beams, but it makes a dipole trap, optical lattice or UV beam along the vertical direction possible.

While the hole will disturb the point spread function, the actual imaging resolution is only weakly affected. The effect of a central hole can be understood as a low pass filter in the k-space of the image, thus not removing sharp features or affecting the numerical aperture or resolution of the objective.

Patch charges on dielectric surfaces can cause unwanted stray electric fields. Due to the proximity of the objective to the plane of the atoms, it is the most critical part. We placed a coarse mesh of gold wires<sup>8</sup> with 50  $\mu\text{m}$  diameter, mounted on a steel ring, on top of the objective, to shield the atoms from patch charges. Gold has a high reflectivity in the infra-red, preventing heating of the mesh from the trapping light. Another often used solution to prevent patch charges are indium tin oxide (ITO) coatings, which have the disadvantage of a reduced transmission of approximately 90 % [100].

### 3.1.5 In-vacuum coils

The in-vacuum coils, referred to as the main coils, are used to generate the magnetic field gradient of the MOT, but were also designed as Helmholtz coils, allowing for strong homo-

---

<sup>7</sup>Special Optics 54-40-33 @ 770,1064nm

<sup>8</sup>TPT Wire Bonder H70-24

geneous fields for Feshbach resonances or to provide a quantisation axis. The current of one coil can be inverted using relays<sup>9</sup>.

In-vacuum coils, even though technically more challenging than coils outside the vacuum, have several advantages: Coils outside the chamber would need to be much larger, which requires more windings or much higher currents to achieve the same magnetic fields, thus causing a higher thermal load. Additionally, the switching time of the in-vacuum coils is expected to be shorter, since no eddy currents between coils and position of atoms can be induced. We measure a settling time of the magnetic field with spectroscopy of the atoms of 2 ms after a fast current switch of 100 A.

The coils are wound from a 4.6 mm diameter OFHC copper tube with an inner diameter of 2.5 mm. Each coil has 8 turns in total on 3 layers, with no inner winding on the middle layer. The turns are spaced by 6.2 mm. The radius of the smallest turn is 59 mm and the distance between the innermost turns of both coils is 53.6 mm.

The maximum reachable magnetic field is 215 G at 200 A, which corresponds to the maximum current of the supply<sup>10</sup>. In a gradient configuration with reversed currents the maximal gradient is 40 G/cm along the strong axis (20 G/cm in the weak axes).

The coils are fixed using stainless steel clamps and are isolated using standard Kapton<sup>®</sup> foil<sup>11</sup>. We first tried to use parts made from Macor<sup>®</sup>, a machinable ceramic that is also suited for ultra high vacuum applications<sup>12</sup>, to fix the coils and isolate them. Since Macor is very brittle this did not work and the mounts broke while fixing them. We still use Macor for fixing and isolating the electrodes, where less mechanical stress is applied.

The copper tubes are connected to hollow copper vacuum feed-throughs with an inner diameter of 4.6 mm. The hollow copper tubes of the coils reach a few millimetres into the hollow feed-throughs and are soldered together to form a vacuum-tight and electrically conductive connection. After soldering the flux material formed a glassy structure on the copper tubes, which was removed carefully before assembling the vacuum system. On the outside the coils are connected to the water cooling system of the lab at 6 bars and to the current supplies. Both coils are connected in series to the same supply. It should be mentioned that the ceramic feed-throughs are very sensitive to mechanical force. Leakage due to broken ceramics occurred several times during the bake-out, requiring a partial disassembly of the vacuum system and re soldering of the feed-throughs each time.

## Switching circuit

For fast switching and precise current control of the main coils, we use a home-built circuitry as sketched in Fig. 3.3 [101]. The whole circuit including the power supplies is placed in a separate room next to the lab and four cables<sup>13</sup> connect it to the main lab. This reduces both acoustic noise from the supplies as well as electrical noise from the current

---

<sup>9</sup>TE Connectivity / Kilovac EV200AAANA

<sup>10</sup>TDK Lambda GEN6-200

<sup>11</sup>DuPont Kapton HN / RS 536-3968

<sup>12</sup>LIGO Vacuum Compatible Materials List: <https://dcc.ligo.org/LIGO-E960050-v12/public>

<sup>13</sup>Cables with 240 mm<sup>2</sup> cross-section are used between the rooms, all other cables are 70 mm<sup>2</sup>

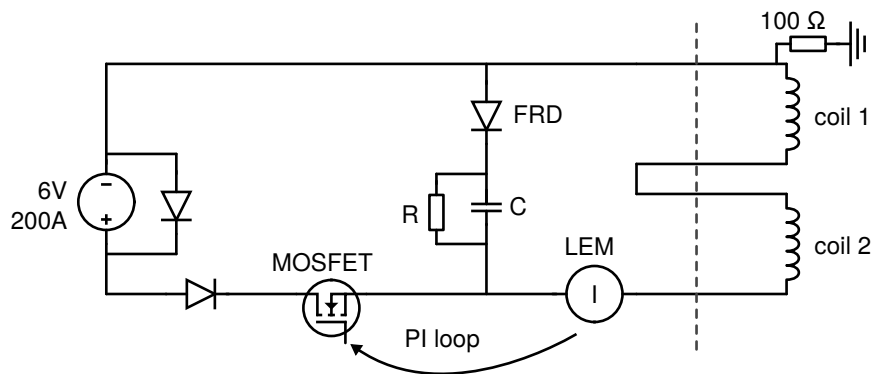


**Fig. 3.3** Control and switching circuit for the in-vacuum coils. A current transducer measures the current and a PI loop feeds back to four MOSFETS. A capacitor in series with a fast recovery diode is used for fast switch-off of the magnetic field. A  $100\ \Omega$  resistor ensures a defined potential to the ground of the main chamber. The dashed line indicates the separation between the two rooms.

transducers. A current transducer<sup>14</sup> measures the current and a homebuilt PI controller adjusts the current using four MOSFETS<sup>15</sup> that are connected in parallel. For fast switching off, a capacitor<sup>16</sup> forms an LC circuit in combination with the coils. After a quarter oscillation the current is stopped by a diode<sup>17</sup>, allowing for a very fast switch off in  $100\ \mu\text{s}$ . A resistor<sup>18</sup> discharges the capacitor with a time constant of  $\tau = RC = 80\ \text{ms}$ . Ramping up the current however is limited to 3 ms by the power supply. All components are dimensioned with enough overhead to allow for much larger currents and fields in the future. In the experiments, we observe a settling time after switching the coils of 2 ms. This is likely limited by eddy currents in the objective. Thus, in most sequences the current is ramped over 3 ms instead of a fast switch off.

A  $100\ \Omega$  resistor connects the coils to the optical table to keep them on the same ground potential as the chamber. This was done to prevent electric fields between the otherwise electrically floating in-vacuum coils and the grounded chamber. A lower resistance caused oscillations when switching due to the additional capacitances between cables and grounds.

### 3.1.6 Compensation coils

Three pairs of coils, called compensation coils or offset coils, are mounted outside the chamber, screwed directly onto the CF63 flanges. Those are used to compensate ambient magnetic fields, move the MOT (i.e. the zero field position) or to apply a quantisation axis. The coils in the z and y axes are identical whereas the x coils are slightly smaller due to space constraints. The coils are made of isolated copper wire<sup>19</sup> with a total of 85 turns (40

<sup>14</sup>LEM IT 400-S Ultrastab

<sup>15</sup>Semikron SKM111AR

<sup>16</sup>Wima GTOMQ05300GF00KS00,  $C = 60\ \mu\text{F}$

<sup>17</sup>Vishay VS-SD1053C22S20L

<sup>18</sup> $R = 1.36\ \text{k}\Omega$

<sup>19</sup>2 by 1 mm wire for y and z, 1.6 by 1 mm wire for x

in  $x$ ). At the maximum current of 15 A this allows for fields of 22 G (16G in  $x$ ). All coils are wound on a thin brass mounting structure which has one loop of copper tube attached for water cooling. The coils are not in Helmholtz configuration due to space constraints. The calculated inhomogeneity in a  $1\text{ cm}^3$  region around the center is  $\approx 1\%$ .

Linear power supplies<sup>20</sup> are used to avoid high-frequency noise, a common problem of switch-mode power supplies. A water-cooled precision resistor<sup>21</sup> is used for current sensing and regulation of the supplies.

### 3.1.7 Electrodes

Rydberg atoms are very sensitive to electric fields. To be able to compensate stray electric fields or apply defined electric field, we use eight electrodes made of 2 mm diameter non-magnetic stainless steel rods. The four rods along the  $x$  direction are spaced by 28 mm in  $y$  and 21 mm in  $z$ . The four rods along the  $y$  direction are slightly further apart to not touch the other electrodes with spacings of 32 mm in  $x$  and 27 mm in  $z$ . The electrodes are fixed to the chamber close to the viewports, using small Macor mounts for electric isolation. A copper wire connects the electrodes to high voltage feed-throughs. On the outside, the electrodes are connected to shielded coaxial cables and are grounded using  $50\ \Omega$  resistors for most of the experiments. Although electrode shapes can be optimised for field homogeneity [97], we focused on optical access, keeping the design simple. Simulations of the electric field showed inhomogeneities of 2% in a  $1\text{ mm}^3$  region at the position of the atoms, mainly limited by a vertical gradient which is caused by the electrically conductive objective.

## 3.2 Lego optics mounts

As a short preface to the description of the optical setup, we will have a quick look at the mounting system we use in our lab. The experience of our group at the MPQ from other experiments, especially the Rubidium [11] and Lithium quantum gas microscopes [13] showed that space for mounting optics becomes limited. In many labs, optics are mounted on optical tables using posts that are clamped using M6 screws on a 25 mm grid. This is a very bulky solution, considering that the laser beams are usually only few millimetres in diameter.

We chose a custom miniaturised version instead, called the ‘Lego system’, in our lab, shown for a part of the MOT setup in Fig. 3.4. This system was developed during setting up of the experiment and is used for all optical setups in the lab. Other experiments in our group have now switched to this system for new optical setups [102].

All setups are mounted on custom 20 mm thick aluminium breadboards using M3 screws. The threads are on a 12.5 mm grid with one additional thread in the middle between four threads, called a ‘double density pattern’. The beam height for nearly all setups is 35 mm. If possible  $1/2$  inch optics were used, which allows for very compact setups. While the actual mirror mounts are standard components, the bases are designed such that a laser beam

---

<sup>20</sup>Servowatt DCP 390,  $\pm 15\text{A}$ , 25V

<sup>21</sup>Isabellenhuetten A-H2-R050F1-K2-0.1

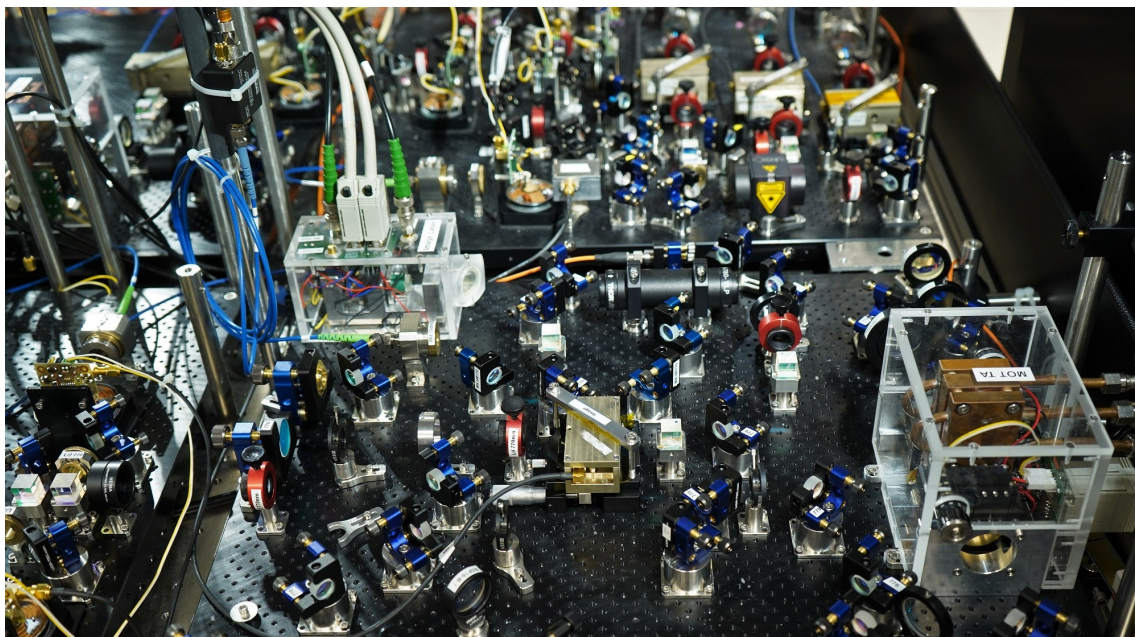


**Fig. 3.4** Picture of the optical setup using the custom 'Lego system'. Shown is a part of the MOT and Image laser setup with the home-built tapered amplifier of the MOT setup (bottom right) and the image laser (middle left). In the back the three AOMs for MOT cooler, repumper and Zeeman slower beam are visible.

which is aligned with a row of threads hits the optics centred. This allows for fast and easy alignment of new setups. Most parts are made of stainless steel, where care was taken to use non-magnetic alloys.

The breadboards for the MOT and GM setup described below as well as many boards around the vacuum chamber have one loop of copper tube for water cooling attached on the bottom. This keeps the setups thermally stable. We saw an improvement in long term stability over 12 hours of the fibre coupling efficiency, if the additional air conditioning for the optical tables was switched off.

### 3.3 MOT setup

In the following, the Laser setup for slowing and cooling potassium atoms is described. This is the first step in every experimental sequence, providing a cloud of cold atoms. Additionally, the image laser used for absorption imaging is described.

#### 3.3.1 MOT laser

The MOT laser is a homebuilt external cavity diode laser with an interference filter as wavelength selective element and a separate partially reflective mirror to form an external cavity [103]. This design is referred to as 'cat-eye' or 'linear' laser.

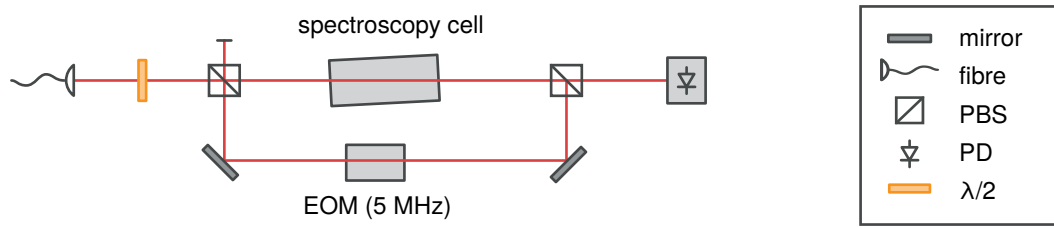


**Fig. 3.5** Modulation transfer spectroscopy used for the MOT (D1 line) and the 770 Master laser (D2 line). The probe beam passes the heated vapour cell counter-propagating to the pump beam. The modulation of the probe is detected on a homebuild photodiode. An EOM adds sidebands of  $\approx 5$  MHz to the pump beam.

### MTS lock

The laser is locked using a potassium vapour cell. A variety of methods for spectroscopy and generation of an error signal of hot alkali vapour cells exist. Often Doppler free spectroscopy or the here described Modulation transfer spectroscopy (MTS) are used. In an earlier stage of the experiment we used a frequency modulation Doppler free spectroscopy, but later switched to MTS, as described below.

MTS was first described in 1982 [104] and is an often used technique nowadays [93]. The basic idea is as follows: Two counter propagating beams, the 'pump' and 'probe', are used. The pump beam with a laser frequency  $\omega$  is frequency modulated with a radio frequency  $\Omega$ , creating sidebands at  $\omega \pm \Omega$ . Both pump and probe beam are overlapped inside a spectroscopy cell and the modulation of the probe beam is detected. This can be understood in the picture of four-wave-mixing, where two frequency components of the pump, the carrier and one of the side bands, and the probe field create two new fields. Those fields interfere with the probe beam and the beating is detected on a photodiode. The main advantage of this scheme is the insensitivity to background signal which can be caused by residual linear absorption of the Doppler broadened sample.

The setup used is shown in Fig. 3.5. The potassium cell is heated to  $60^\circ\text{C}$  inside an aluminium tube and tilted slightly to prevent etalon effects due to the uncoated windows. The beam from the MOT laser is first split by a PBS into the 'pump' and 'probe' beam. The probe then directly passes through the cell and a second PBS and is detected on a photodiode. A resonant EOM is used to generate sidebands of  $\approx 5$  MHz on the pump beam. The pump is overlapped with the probe in the second PBS such that both beams are counter propagating inside the cell. The signal of the photodiode is demodulated with the same RF frequency used to generate the EOM sidebands.

The resulting error signal is sent to a homebuild lockbox with two branches. After a first amplification, a PI loop is used for fast feedback to modulate the laser current using a field-effect transistor. A second branch integrates this signal again, creating a (PI)I filter and feedbacks to the piezo, changing the cavity length to compensate slow drifts.

The laser is locked to the  $4S_{1/2}F = 1, F = 2$  crossover to the  $4P_{3/2}$  transition. Due to the unresolved hyperfine structure in the  $4P_{3/2}$  state of potassium we can not assign a defined  $F'$  quantum number of the excited state for the lock [93].

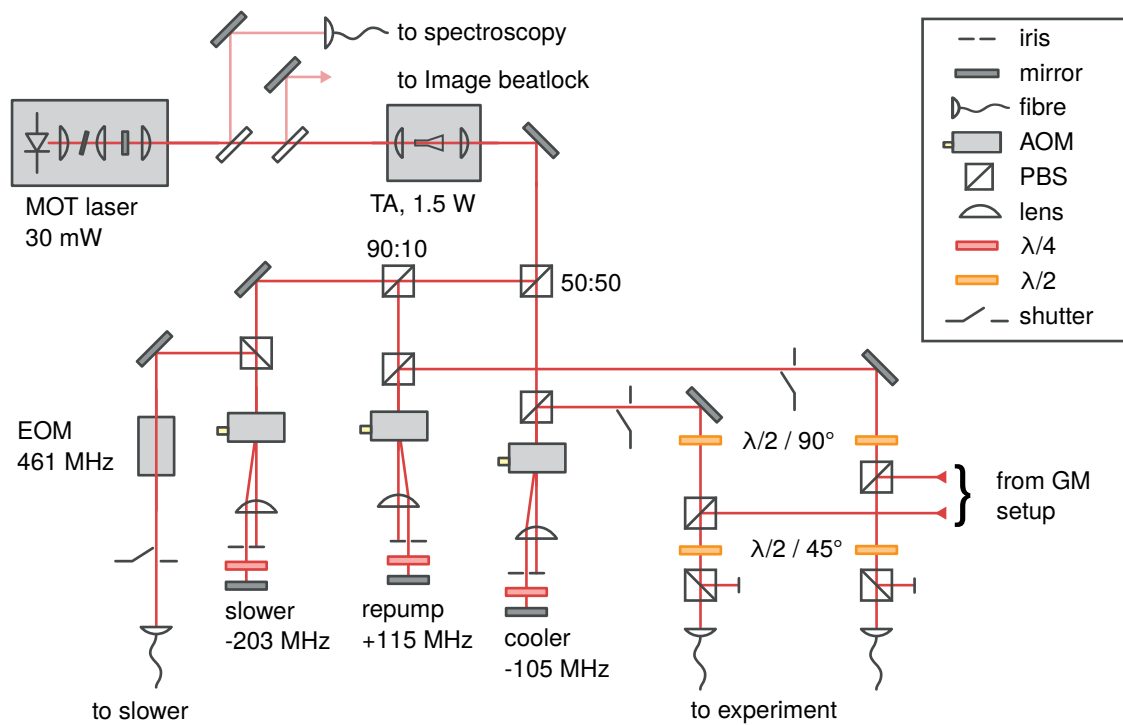


**Fig. 3.6** Setup of the MOT laser: The linear laser is locked to a MTS spectroscopy and amplified using a tapered amplifier (TA). Three AOMs in double pass are used for amplitude and frequency control (1st and -1st orders used, frequencies given are AOM frequencies for resonance of the respective transitions). The Zeeman slower beam is modulated at 461.7 MHz using a resonant EOM. The cooler and repumper beams are overlapped with the corresponding GM beams using half wave plates and polarising beam splitter cubes (PBS). Polarisation maintaining optical fibres connect to the experiment.

As mentioned above, we first used a slightly simpler setup for FM spectroscopy. A beam with sidebands of 60 MHz was sent through the vapour cell, retro reflected and sampled out using a quarter wave plate and polarising beam splitter. The signal was detected on a photo diode and demodulated. We experienced drifts of lock point and a strong sensitivity to the temperature of the EOM. Even though an upgrade of this setup using separate 'pump' and 'probe' beams and a differential detection might have solved these problems, the MTS lock turned out to be simpler and robust.

### 3.3.2 Optical setup

All beams for the MOT and the Zeeman slower are derived using AOMs, shown in Fig. 3.6. This is possible since the ground state hyperfine splitting of  $^{39}\text{K}$  with 461.7 MHz can be bridged using AOMs with frequency shifts in the range of 100 MHz. The laser is amplified to  $\approx 1.5$  W using a tapered amplifier. The beam is then split in three branches for the cooler, repumper and the Zeeman slower beam. The cooler is shifted by  $-210$  MHz in a double

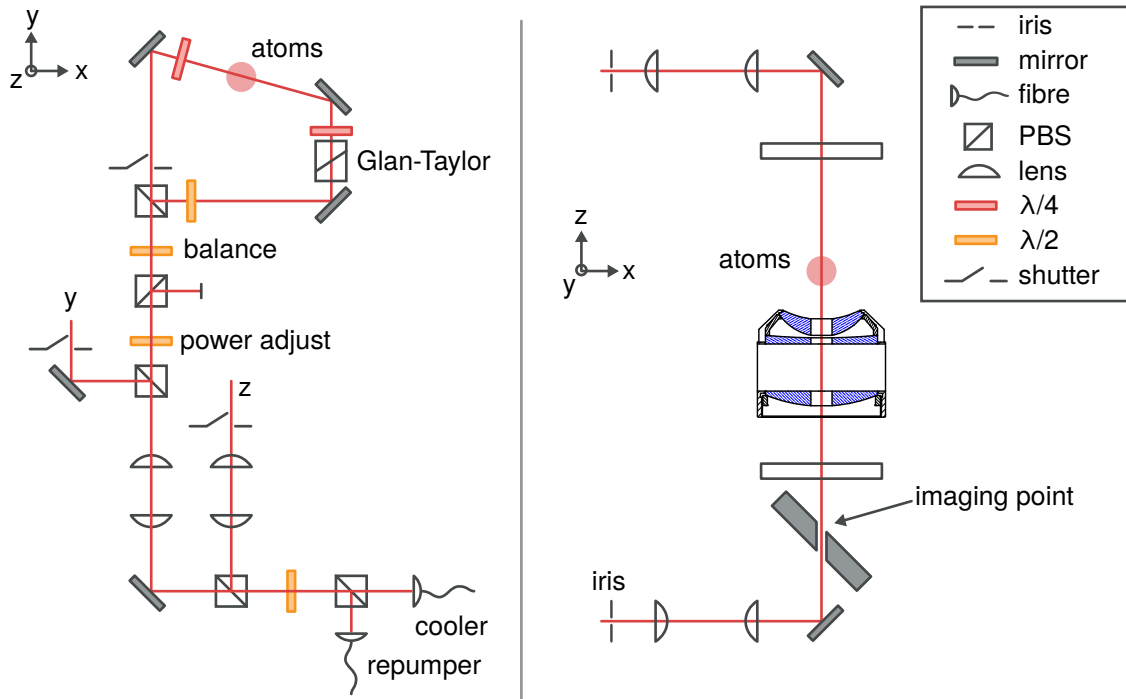


**Fig. 3.7** Optical setup for MOT and GM beams around the chamber. **Left:** cooler and repumper beams are overlapped and magnified. Cubes are used for independent power adjustment and beam balancing of each axis (only shown for x axis, identical for y and z axis). **Right:** Alignment of the vertical z beams through the hole of the objective. The irises are imaged onto the mirror with a hole using two 4-f telescopes to reduce stray light on the sCMOS camera.

pass configuration to address the  $4S_{1/2}, F = 2$  to  $4P_{3/2}, F = 3$  transition. The repumper is shifted by +230 MHz, addressing the  $4S_{1/2}, F = 1$  to  $4P_{3/2}, F = 2$  transition. The RF frequencies for the AOMs are generated using voltage controlled oscillators<sup>22</sup>.

Both MOT cooler and repumper are overlapped with the GM cooler and repumper and sent to the experimental table using polarisation maintaining fibres. Two polarising beam splitter cubes and a half wave plate at 45 degrees are used to spatially overlap both beams with the same polarisation. Note that in this process half the optical power is lost, since the output of the second port of the last PBS is not used.

We also tested using interference filters, identical to the ones used in the lasers, to overlap MOT and GM without any power loss. This solution was not used due to the very sensitive alignment, caused by the steep tuning curve of the filter.

On the experimental table both repumper and cooler are overlapped with the same HWP and PBS setup used before, shown in Fig. 3.7. After this point all MOT and GM beams are overlapped with the same polarisation. One port of the PBS is used for the z MOT beams and the other part is split for the x and y beams. Two telescopes magnify the beams to

<sup>22</sup>Homebuilt amplifiers with Minicircuits POS-150

$1/e^2$  diameters of 3 mm in z and 7 mm in x and y. Each axis can be individually adjusted in power and power-balance using wave plates. Using mounts with micrometer screws for the wave plates turned out useful for precise control, especially for alignment of the optical molasses. To allow for better optical access the MOT beams in the x direction have an angle of 14.5 degrees with respect to the x axis.

Since the MOT beams are also used for fluorescence imaging of single atoms, it is important to suppress stray light from those beams. Especially the vertical beams which are sent through the objective are critical, as any scatter on the hole of the objective or the hole of the last mirror are visible on the few photon sensitive sCMOS camera. Both vertical beam paths have irises to block the wings of the Gaussian beams. The irises are then imaged onto the mirror with the hole, directly under the objective, using two lenses in 4-f-configuration. A hollow inset in the hole of the mirror, made of structured and blackened steel, further prevents scatter and reflections towards the camera.

### 3.3.3 Zeeman slower

As described above the beam for the Zeeman slower is also derived from the MOT laser. The beam is resonant with the atoms inside the slower, but is detuned at the position of the MOT due to the spin-flip design. With a detuning of  $-205$  MHz from the  $4S_{1/2}, F = 2$  to  $4P_{3/2}, F = 3$  resonance and a maximum magnetic field of  $\approx 320$  G at the beginning of the slower, the capture velocity is  $\approx 330$  m/s. The frequency is shifted with a 200 MHz AOM in double pass configuration. For efficient optical pumping from the  $m_F = 2$  to  $m_F = -2$  state in the spin flip region (a magnetic field flip inverts the quantisation axis), an EOM modulates sidebands at 461.7 MHz. We measure an amplitude of the sidebands of  $-16$  dBc with a beat note of slower beam and image laser.

### 3.3.4 Imaging laser

A second laser, identical to the MOT laser, is used for absorption imaging. In principle light from the MOT laser can be used for this purpose, but this approach would limit the frequency tuning range to the AOM bandwidth. A second laser allows for a significantly larger frequency tuning range. The optical setup is depicted in Fig. 3.8.

The image laser is beat locked (or 'offset locked') to the MOT laser as follows: Light from both lasers is overlapped using a non-polarising 50:50 cube. The beat note of both lasers is detected on a photodiode<sup>23</sup> and locked to a reference frequency using a home-built digital phase-frequency lock<sup>24</sup>.

A double pass AOM shifts the laser by 400 MHz and is also used for amplitude control. The laser is locked to the  $4S_{1/2}, F = 2$  to  $4P_{3/2}, F = 3$  transition at a beat note frequency of 190 MHz. The beam is then split and sent to the experiment via three fibres, used for imaging on all three axes.

For all measurements presented in this work, only the x axis imaging was used, however,

<sup>23</sup>Thorlabs DET025AFC

<sup>24</sup>based on an Analog Devices AD9901 frequency detector

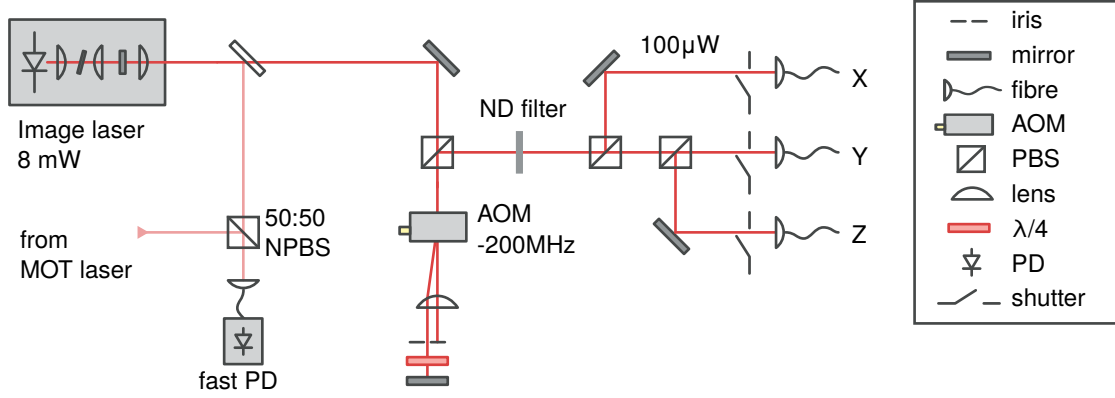


**Fig. 3.8** Image laser setup: The laser is identical to the MOT laser. Using a non-polarising 50:50 beam splitter cube (NPBS) image and MOT laser are overlapped and the image laser is locked using the beat note. An AOM is used for amplitude control. The signal is attenuated (neutral density (ND) filter with 25 % transmission) and split for imaging on each axis. One or multiple axis can be selected using optical shutters.

	MOT	cMOT	red molasses
Cooler detuning	$-5 \Gamma$	$-3 \Gamma$	$-1.5 \Gamma$
Cooler intensity ( $I_{sat}$ )	20	19	6
Repumper detuning	$-4 \Gamma$	$-1.5 \Gamma$	$0 \Gamma$
Repumper intensity ( $I_{sat}$ )	20	0.4	1
Zeeman slower detuning	$-34 \Gamma$	-	-
Zeeman slower intensity ( $I_{sat}$ )	100	-	-

**Tab. 3.1** Experimental parameters for the MOT stage. Cooler detunings referenced to the  $4S_{1/2}, F = 2$  to  $4P_{3/2}, F' = 3$  transition and repumper to the  $4S_{1/2}, F = 1$  to  $4P_{3/2}, F' = 2$  transition. Intensities are given per beam in units of the saturation intensity with  $I_{sat} = 1.75 \text{ mW/cm}^2$  for the D2 line of potassium. The gradient from the in-vacuum coils is  $20 \text{ G/cm}$  on the strong axis. Due to the spin-flip design, the Zeeman slower is detuned in the MOT.

imaging on all axes was used for alignment. On the experimental table the beam is collimated<sup>25</sup> to  $7.5 \text{ mm}$  ( $1/e^2$  diameter) and aligned onto the atoms.

An uncoated spherical lens<sup>26</sup> images the atoms onto a CCD camera<sup>27</sup> for absorption imaging. Since also UV and the dipole trap pass through this lens, it is not coated.

### 3.3.5 Characterisation

To prevent confusion with the grey molasses [77], the optical molasses on the D1 line [75] is referred to as *red molasses*. The experimental sequence for loading the MOT and char-

<sup>25</sup>Thorlabs F810APC-780

<sup>26</sup>Thorlabs LB4941 ( $f = 100 \text{ mm}$ ), uncoated

<sup>27</sup>Ximea MD028CU-SY

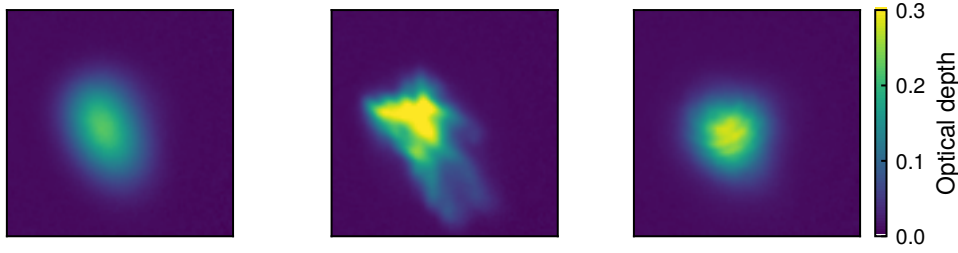


**Fig. 3.9** Absorption pictures after loading the MOT for 2 s (**left**), after the red molasses (**middle**) and after the grey molasses (**right**). The total number of atoms is about  $1 \cdot 10^6$ . The shape of the red molasses depends strongly on the exact alignment of optical beams and magnetic fields. The MOT picture appears weaker due to the non-zero magnetic field, which decays over several milliseconds after switching off the coil current.

acterisation is as follows: First cooler and repumper as well as the Zeeman slower are switched on. After two seconds of MOT loading, the Zeeman slower beam and coil are switched off. For loading single atoms, as described later, 250 ms of MOT loading time are sufficient. After 50 ms the detunings and intensities are ramped in 1 ms to spatially compress the MOT (cMOT), as shown in Table 3.1. After 10 ms the cooling beams and magnetic field gradient are switched off. The atomic cloud expands during a time of flight and an absorption picture  $X_{\text{abs}}$  with an  $50 \mu\text{s}$  imaging pulse ( $0.1 I_{\text{sat}}$ ) is taken. The atoms are repumped ( $1 I_{\text{sat}}$ ) during imaging. A second reference picture  $X_{\text{ref}}$  without atoms and a third background picture  $X_{\text{bcg}}$  without imaging light are taken with 100 ms delay. The optical density of the cloud  $D = -\ln [(X_{\text{abs}} - X_{\text{bcg}})/(X_{\text{ref}} - X_{\text{bcg}})]$  is calculated per pixel, shown in Fig. 3.9.

The size of the atomic cloud  $\sigma$  increases with the time of flight  $t$  as  $\sigma(t)^2 = \sigma_0^2 + k_B T t^2 / m$  with the initial size  $\sigma_0$ , the temperature  $T$ , Boltzmann constant  $k_B$  and mass of the atoms  $m$  [75]. We determine  $\sigma$  from a Gaussian fit and extract temperatures of  $T_{\text{MOT}} = 230 \mu\text{K}$  after the MOT,  $T_{\text{cMOT}} = 150 \mu\text{K}$  after the compressed MOT stage and  $T_{\text{molasses}} = 35 \mu\text{K}$  after red molasses cooling.

Due to the small hyperfine splitting of the excited  $4P_{3/2}$  states in  $^{39}\text{K}$ , the red molasses in potassium only works for a small detuning range, given by the  $4P_{3/2}, F' = 2$  to  $F' = 3$  difference of 21 MHz [75]. This makes the molasses sensitive to experimental parameters such as detuning or magnetic fields.

Optical molasses cooling can be used directly after the MOT stage to cool the atom further. However, this requires dynamical tuning of intensities and detunings, making it sensitive to experimental drifts and imperfections [75]. We found that a short grey molasses stage after switching off the magnetic field gradient cools the atoms in a very robust way, being insensitive to residual magnetic fields. It might seem non-intuitive to first use grey molasses cooling before the red molasses stage, but since the red molasses is used for loading and imaging single atoms in tweezers, we found that this intermediate step improves the robustness of the experiment.

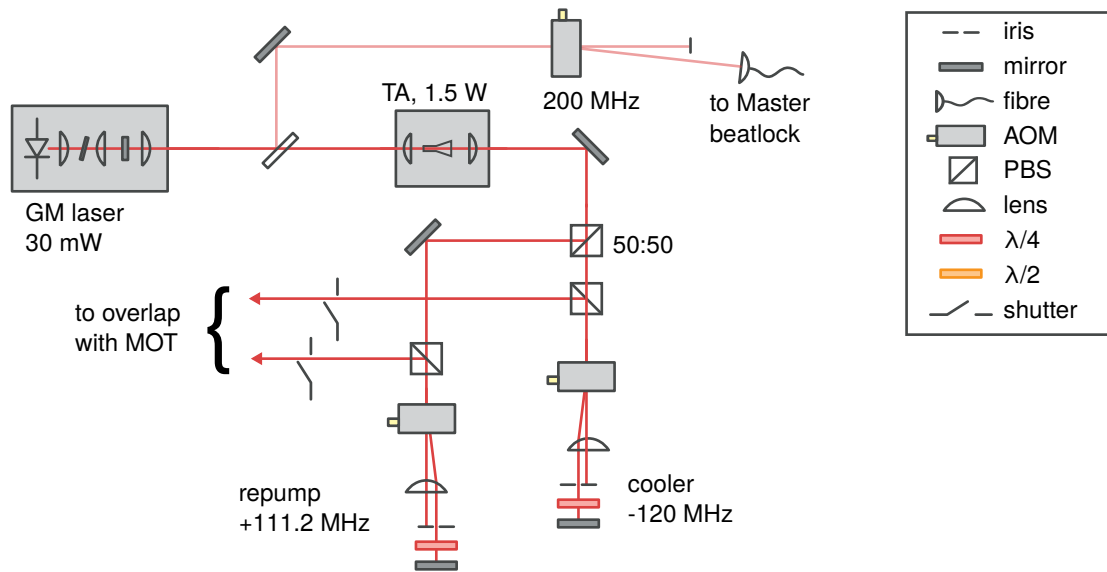


**Fig. 3.10** Optical setup of the grey molasses laser: The laser is amplified with a tapered amplifier (TA) and split into the cooler and repumper beam. Two AOMs in double pass bridge the ground state splitting. For frequency locking a part of the light is shifted by 200 MHz with an AOM and then locked to the beat note with the 770 Master laser.

## 3.4 Grey molasses cooling

The following section describes the grey molasses (GM) setup. While grey molasses cooling is in principle not necessary for direct loading of optical tweezers, it turned out to be a very useful technique. In comparison to the red molasses, we observe no influence due to decaying magnetic field gradients after the MOT coils are switched off, which makes it a robust cooling step. Additionally, this laser is used for all techniques requiring light on the D1 transition, as state preparation (Section 4.3), spectroscopy on the D1 line (Section 4.4), or repumping for Raman sideband cooling (Section 4.5).

### 3.4.1 Grey molasses laser

The optical setup of the grey molasses laser is shown in Fig. 3.10 and is similar to one of the MOT laser. The laser, besides lasing at 770 nm, is amplified using a TA and cooler and repumper beams are derived using two AOMs in double-pass configuration. As shown in Fig. 3.6 both beams are then overlapped with the MOT beams.

Besides the following differences MOT and GM laser setup are identical: The laser is not locked directly to a spectroscopy cell, but a second identical laser, called the 770 master is used, which is locked to the  $4S_{1/2}, F = 1, F = 2$  crossover to  $4P_{1/2}, F' = 1$  transition using a MTS spectroscopy lock, identical to the one shown in Fig. 3.5. A part of the GM light is sampled out and shifted by 200 MHz using an AOM. The GM laser is then locked to the master laser, using the same beat lock techniques used also for the image laser. This

allows to change the frequency of the GM laser by  $\approx 1$  GHz, only limited by the locking electronics used.

For all measurements, the detunings are referenced to the  $4S_{1/2}, F = 1/2$  to  $4P_{1/2}, F' = 2$  transition for cooler ( $F = 2$ ) and repumper ( $F = 1$ ). Only the common detuning  $\Delta$  of both beams is varied by changing the beat lock reference, keeping the Raman detuning  $\delta$  between cooler and repumper constant.

Since grey molasses cooling is sensitive to the Raman detuning of the two beams [77], we use two DDS<sup>28</sup> generators to supply the RF signals driving the AOMs, in contrast to VCOs which are used for most other AOMs.

For grey molasses cooling, we use the same experimental sequence as introduced in Section 3.3. The grey molasses light is switch on directly after the MOT beams are switched off. However, the magnetic field is ramped down linearly over 3 ms, which does not affect the cooling performance of the grey molasses. A detuning of  $\Delta = 6\Gamma$  is used, while the Raman detuning is  $\delta = 0$ . Each beam has an intensity of  $28 I_{\text{sat}}$ . We measure a temperature of  $29 \mu\text{K}$  after the grey molasses cooling.

### 3.5 Dipole trap

To improve alignment and for first characterisation measurements, a dipole trap with a single focussed beam is used. Even though this is not directly used for the measurements described, it turned out to be extremely useful for optimisation and alignment steps throughout the work of this thesis, including alignment of the Raman and UV beams or first spectroscopy measurements of the UV laser. An absorption measurement provides a good signal with only one single experimental run, in contrast to measurements with single atoms, which require much more statistics.

The setup is shown in Fig. 3.11. A part of the light from the 1064 nm laser, that is also used for the optical tweezer setup (Section 4.1), is split off. A shear mode AOM<sup>29</sup> is used for intensity control. Compared to the so far described 'compression mode' AOMs, shear-mode AOMs require substantially lower RF power, which reduces thermal drifts. Due to the lower velocity of the shear mode, the rise time and bandwidth of the intensity stabilisation is  $\approx 10$  kHz. The beam is focussed and imaged onto the position of the atoms. We measure a waist at the atoms of  $50 \mu\text{m}$ . The calculated trapping parameters for 6 W of power are a trap depth of  $200 \mu\text{K}$ , corresponding to a ground state light shift of 4.25 MHz and trap frequencies of  $\omega_{\text{rad}} = 2\pi \cdot 1.3$  kHz and  $\omega_{\text{ax}} = 2\pi \cdot 6$  Hz in the radial and axial direction.

The dipole trap is loaded using the grey molasses, where the trap is switched on during the GM cooling. Since the grey molasses is insensitive to the detuning  $\Delta$ , it will cool atoms both inside the trap and in free space, thus loading the trap.

The beam is overlapped with the x axis imaging beam and the UV beam, using dichroic mirrors. For alignment the narrow band filters in front of the camera are removed. The absorption of the atoms, the dipole trap and the UV beam are then imaged onto the camera,

<sup>28</sup>Homebuilt design, based on an Analog Devices AD9910 DDS

<sup>29</sup>Gooch & Housego I-FS080-2S2G-3-LV1

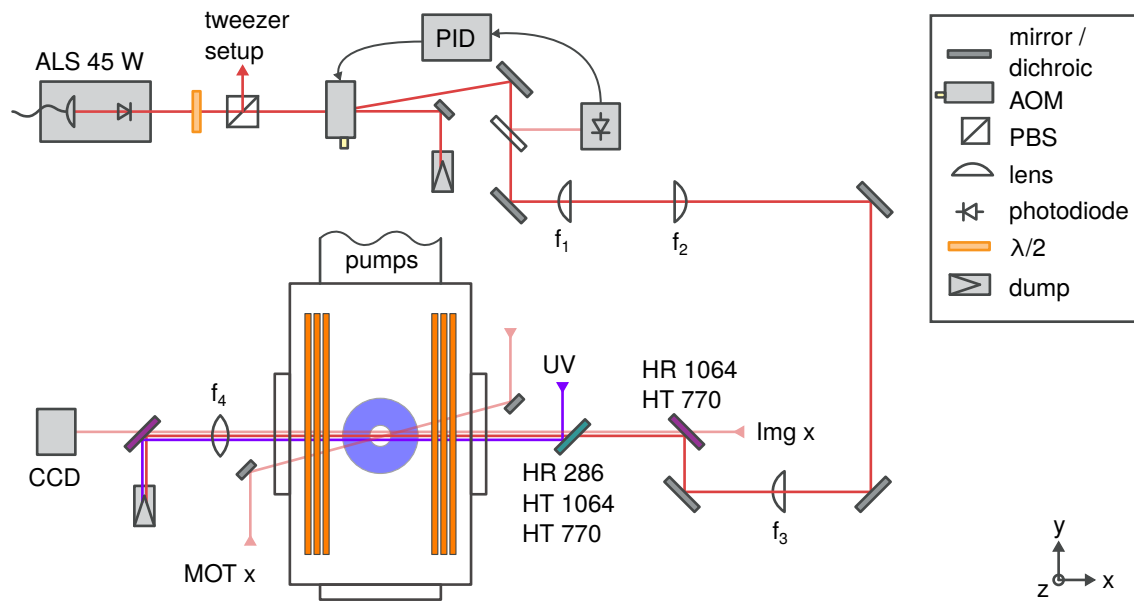


**Fig. 3.11** Setup of the dipole trap (X-trap): View from above onto the main chamber with the in-vacuum coils (orange) and the objective (blue). Light from the 1064 nm laser is split for the tweezers and dipole trap. An AOM is used for intensity stabilisation and control. The beam is focussed ( $f_1 = 200$  mm) and imaged ( $f_2 = 600$  mm,  $f_3 = 400$  mm) in a 4-f configuration onto the atoms. Dichroic mirrors are used to overlap the beam with the UV and imaging light (Img x). An uncoated lens images the atoms onto a CCD camera. This camera is used for absorption imaging or, if the last filter is removed, for alignment of all beams. The x MOT beams are tilted 14.5 degrees with respect to the x axis.

allowing one for an easy alignment of all beams.

## Chapter 4

### Single atoms in tweezers

In this chapter, we will focus on how to build on the setup introduced in [Chapter 3](#) to provide an array of trapped single atoms, cooled close to their motional ground state.

First, the setup for the generation of arrays of optical dipole traps, referred to as optical tweezers or simply tweezers, is explained in [Section 4.1](#). Afterwards, we discuss in [Section 4.2](#) and [Section 4.3](#) loading and imaging of trapped single atoms and how those can be prepared in a defined quantum state.

In [Section 4.5](#) we discuss the key ideas of Raman sideband cooling and how this is implemented in our setup to cool atoms close to the motional ground state of the trap. In [Section 4.6](#) and [Section 4.7](#) we characterise the improvements of side band cooling. The same techniques used for Raman sideband cooling are also used for coherent manipulation of the ground state atoms, described in [Section 4.8](#), completing our experimental toolbox for preparation and control of single atoms.

Only an overview will be given in the first part, especially of the SLM setup and tweezer array generation. A detailed description and characterisation can be found in the thesis of Lorenzo Festa [[105](#)].

#### 4.1 Optical setup and SLM

In the following, the experimental setup for generating arrays of optical tweezers is introduced.

A high power 45 W laser<sup>1</sup> at 1064 nm is used to generate the optical dipole traps. The lasers used for cooling and imaging are the same as those described in [Chapter 3](#). An AOM<sup>2</sup> is used for intensity stabilisation and control of the light. An RF generator<sup>3</sup> at 90 MHz is used to generate the radio frequency signal for this AOM.

Telescopes magnify the beam to an  $1/e^2$  diameter of 12 mm, matching the active area of the SLM<sup>4</sup>. The beam is then reflected by the SLM with a chip size of 12 by 16 mm and a resolution of 800 by 600 pixels.

A telescope in a 4-f configuration images and magnifies the SLM onto the objective, matching the diameter of the objective of 40 mm. In other words, the lens after the SLM creates a first image of the tweezer array in its focal plane and the second lens with the objective

---

<sup>1</sup>Azurlight Systems

<sup>2</sup>Gooch & Housego AOMO 3080-197

<sup>3</sup>AnaPico ASPIN

<sup>4</sup>Hamamatsu X10468-03WL

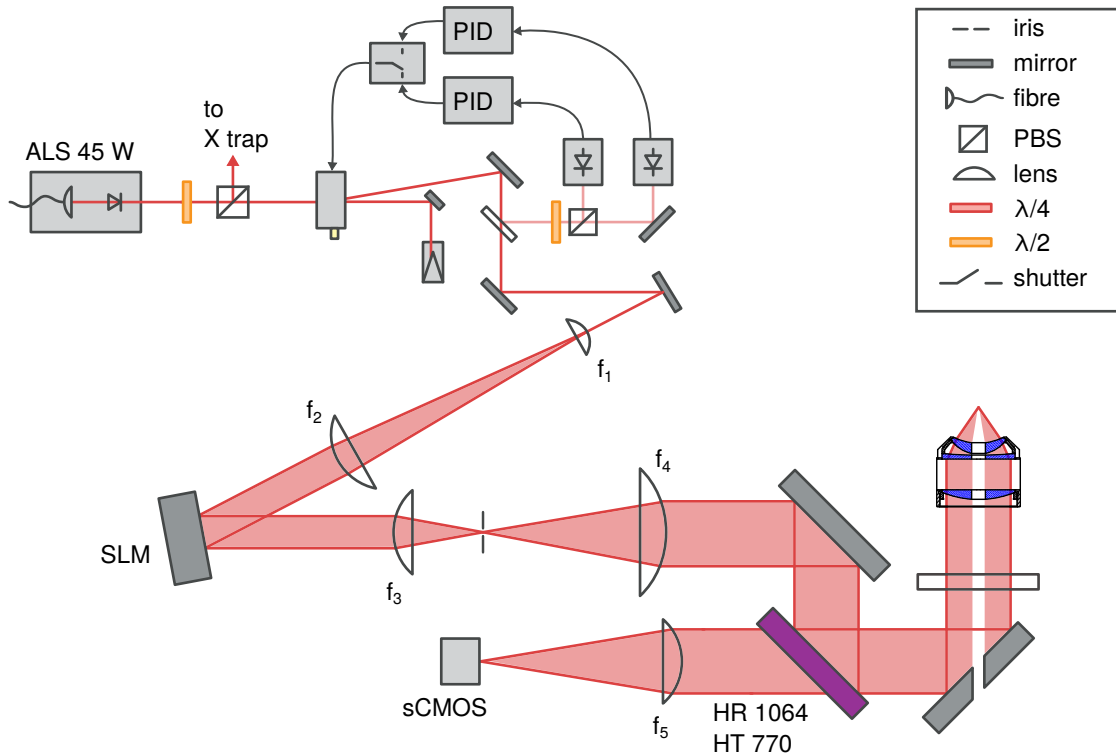


**Fig. 4.1** Setup for tweezer generation. An AOM is used for intensity stabilisation and chopping of the trapping light. Two intensity stabilisation loops can be used for power stabilisation, allowing for a high dynamic range. A switch allows for fast in-sequence change between both loops. Two telescopes (not shown:  $f = 50$  mm,  $f = 150$  mm and  $f_1 = 50$  mm,  $f_2 = 300$  mm) expand the beam to a  $1/e^2$  diameter of 12 mm to match the size of the SLM. The last telescope ( $f_3 = 250$  mm,  $f_4 = 800$  mm) images the SLM onto the objective. A blade at the focus of  $f_3$  blocks unwanted parts at the intermediate image plane. The fluorescence signal from the atoms is collected by the same objective and separated from the trapping light with a dichroic mirror. A lens ( $f_5 = 250$  mm) images the atoms onto a sCMOS camera.

demagnify and image this array onto the centre of the main chamber.

To increase the dynamic range for the intensity stabilisation of the trapping light, we use two independent stabilisation loops. Two photodiodes that differ by a factor of 100 in sensitivity are used. Each diode is combined with a homebuilt PID controller that feeds back to the AOM to stabilise the intensity. A switch allows to choose between two different control loops during the sequence, allowing for a high dynamic range of the stabilisation. A non linear stage in each loop further compensates the non linear AOM response.

Both the last mirror before the objective and the objective itself have a central hole, allowing optical access in the vertical direction. To prevent heating from or uncontrolled scattering due to the trapping light, we block any light, which would not be reflected by the mirror beforehand as follows: In addition to the phase pattern used to create the tweezers, we also use the SLM to change the angle of the light in the central part (with a radius at the

objective ( $r_{\text{objective}} < 6.5 \text{ mm}$ ) and the wings ( $r_{\text{objective}} > 20 \text{ mm}$ ) of the beam by overwriting the phase pattern with a grating. A blade in the first focus after the SLM then blocks those parts as well as higher diffraction orders from the SLM.

For imaging a dichroic mirror (HT 670 – 810 nm, HR 950 – 1100 nm) is placed in the path of the 1064 nm laser before the objective. Fluorescence light from the atoms is collected and collimated by the objective and transmitted through this dichroic mirror. A lens images the atoms onto a few-photon-sensitive camera<sup>5</sup>. One camera pixel corresponds to approximately  $0.86 \mu\text{m}$  by  $0.86 \mu\text{m}$  in the focal plane of the objective.

Since the MOT beams for the z axis are aligned through the hole of the objective, they can cause significant levels of scattered light going onto the camera. The light levels scattered onto the camera can be of comparable intensity to the fluorescence of a single atom, making it impossible to detect the signal of single atoms above the noise. Several measures were taken to reduce this: As shown in Fig. 3.7, two irises in the z beams are imaged onto the position of the hole of the mirror, cutting the wings of the Gaussian beam profile. In addition a tube-like inset of blackened steel with a structured surface to prevent specular reflections is inserted into the hole of the mirror.

## 4.2 Loading and imaging single atoms

The principle of loading and imaging single atoms in optical tweezers is the same as cooling atoms in free space. In many experimental setups an optical molasses is used to cool atoms that are trapped in an optical dipole trap. The scattered light is then used for single atom imaging. As shown in Section 2.2 this is not possible in our case due to the very strong anti-trapping of the excited  $4P$  states in potassium, when using 1064 nm light.

A way to circumvent this problem is by alternating trapping light and cooling light [81]. If the light of the dipole trap is chopped much faster than the trap frequency, the atoms experience an averaged trapping potential. If the molasses light is chopped interleaved to the trap, as shown in Fig. 4.2, the atoms are cooled, but experience no light shift or anti-trapping during the cooling phase. To avoid parametric heating, the chopping frequency has to be much larger than the trap frequency. We chop the light at a frequency of 1.4 MHz, which is limited by the rise time of the AOMs. For loading and imaging, the axial trap frequency is  $\approx 150 \text{ kHz}$ , one order of magnitude lower than the chopping frequency.

A disadvantage of the chopping technique is the larger peak power required, since the atoms only experience an averaged potential. This is not a limitation for the work presented here, but limits the total number of tweezers for a given laser power to approximately 100 traps with our current setup.

If this becomes a limitation in future work, the chopping scheme can be improved as follows: Shorter rise and fall times of the light during chopping would allow for a very unequal duty cycle where the trapping light is switched off only briefly. This reduces the peak power requirement to be only slightly larger than the average power. Faster rise times can be realised by focussing the beams in the AOMs or by using EOMs for chopping [106]. The

---

<sup>5</sup>Andor Zyla 4.2 sCMOS

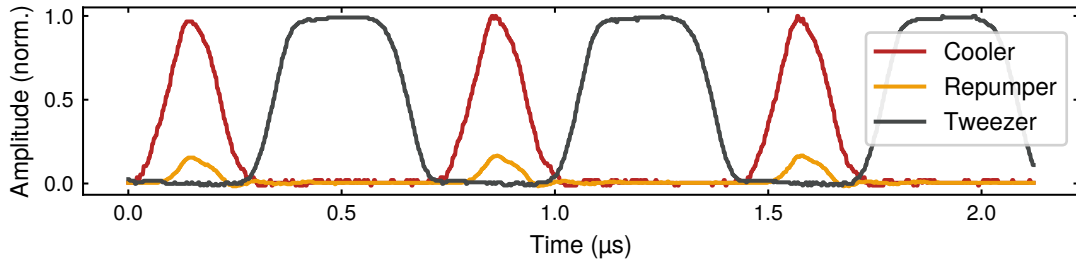


**Fig. 4.2** Photodiode signals of the MOT cooler, repumper and tweezer light during imaging. Cooler and tweezer signals are normalised while the ratio of cooler to repumper is as in the sequence. The repetition rate is 1.4 MHz, limited by the risetime of the MOT AOMs.

resulting lower effective scattering rate during imaging is not limiting, since it can be compensated by longer imaging times, which are 10 ms and short compared to all other steps in our sequence.

Higher chopping frequencies would reduce residual heating, however we did not observe any limitations due to chopping so far.

For intensity stabilisation of the tweezer power the photodiode signal is lowpass filtered<sup>6</sup> at a cutoff frequency  $f_c = 600$  kHz. The cutoff  $f_c$  is much higher than the loop bandwidth of the stabilisation with about 200 kHz, but suppresses the chopping frequency sufficiently. During chopping, the intensity stabilisation thus stabilises the average power. Therefore, the trap depth of the atoms is kept constant when switching from chopped to continuous mode.

The experimental sequence for loading and imaging a single atom is similar to that for loading atoms in the magneto-optical trap, as described in [Section 3.3](#). After 250 ms of loading atoms to the MOT and a short compressed MOT stage, the magnetic field gradient is ramped down and the grey molasses cools the atoms for a few milliseconds. The tweezer light and optical molasses are chopped for 40 ms to load atoms into the tweezers. A fluorescence picture is taken with 10 ms exposure.

Since the chopped molasses cooling is independent of the trap light shift, all parameters can easily be adjusted beforehand in a MOT sequence using absorption pictures. This allows for single-shot optimisation, enabling an optimisation of cooling parameters within minutes. Single atom signals would require much higher statistics due to the binary information gained in each shot.

We noticed a strong variation of the loading probability for the tweezers in an array, changing on a time scale of tens of minutes. The loading probability over time appeared as fringes moving through the array. Mounting one mirror in the MOT path onto a piezo allowed for a reproducible change of these patterns by a change of the piezo voltage. This can be explained by interference of the cooling beams. Even though in one dimension they show no interference due to the different polarisations, in three dimensions all six beams will create interference patterns. The size of the wave function in the tweezers is comparable to the

<sup>6</sup>Thorlabs EF506

length of the polarisation gradient ( $\lambda/2 = 385 \text{ nm}$ ) of the optical molasses, causing differences in cooling performance, depending on which part of the polarisation gradient the atoms experiences. This effect was also reported in similar experiments [10, 11, 107, 108]. To prevent it, we modulate one mirror on each axis of the MOT ( $x : 500 \text{ Hz}$ ,  $y : 450 \text{ Hz}$ ,  $z : 400 \text{ Hz}$ ) during loading and imaging. The modulation is fast compared to the total imaging time of 10 ms, but much slower than the scattering rate of the atoms. As a result of the modulation, the beam path in each axis is continuously changed by few micrometer, larger than the length scale of the polarisation gradient. An alternative solution would be to slightly detune the frequencies of each path of the MOT, resulting in a similar time averaging effect.

### 4.2.1 Tweezer arrays

A variety of methods to create arrays of optical tweezers were developed over the last years, including the here-used spatial light modulators (SLMs) [16–20], digital mirror devices (DMDs) [51], acousto optic deflectors (AODs) [19, 50] and microlens arrays (MLAs) [21]. The SLM is the most flexible approach both in terms of arbitrary array patterns as well as for aberration correction.

AODs on the other hand are well-suited for dynamic patterns and atom movement, allowing sorting of arrays of single atoms. In 1D they can be used for both pattern generation and sorting simultaneously [19]. In 2D many experiments nowadays combine multiple of the mentioned schemes [20, 21]. Direct in-situ rearrangement using SLMs was demonstrated, but is technically challenging [17].

We decided to use an SLM since it offers the highest flexibility. However, in a future upgrade, an AOD for sorting, selective light shifts of single atoms or spin selective imaging will be implemented [106, 109].

One challenge when using SLMs is the calculation of a phase pattern which creates the desired amplitude pattern, in this case a 2D array of optical tweezers. For this we use a modified Gerchberg-Saxton algorithm [17, 105, 109, 110]. This pattern is then sent to the SLM and stays static for all experiments presented within this thesis. This approach also allows further corrections of aberrations induced by optical elements, by adding correction patterns to the calculated phase pattern. For this we measure and correct aberrations after the SLM by adding Zernike polynomials to the phase pattern, as described in [109]. A selection of tweezer patterns used throughout this thesis is shown in Fig. 4.3.

### 4.2.2 Atom lifetime

One limitation for high fidelity preparation and detection is the lifetime of the atoms. While the total number of atoms which are held in an array decreases exponentially over time, the probability that one atom is lost after a time  $t$  is given by  $1 - \exp(-t/\tau)^N$ , with the lifetime  $\tau$  and the number of atoms  $N$ . When scaling systems to hundreds of atoms, this places a very strong requirement on the lifetime, since no atom loss should happen while the system is prepared and imaged.

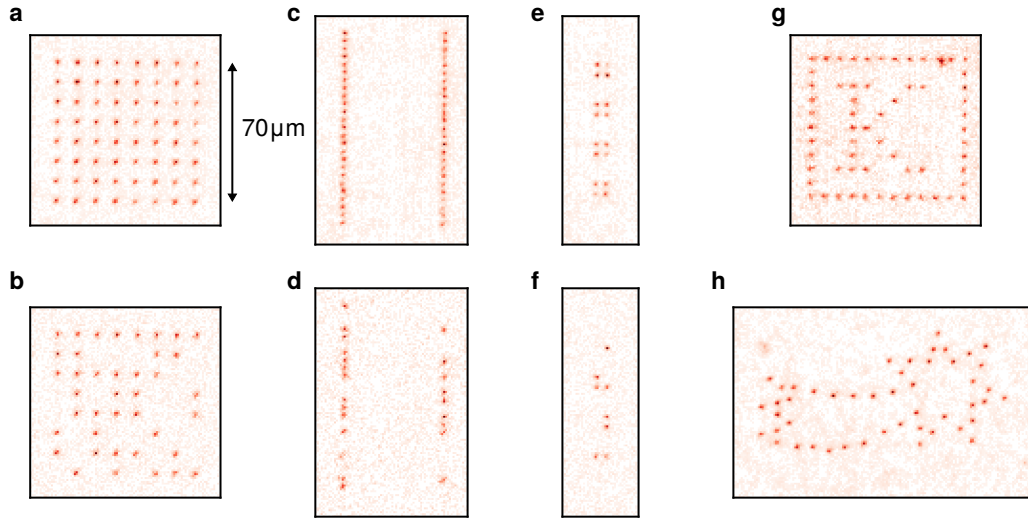


**Fig. 4.3** Averaged and single fluorescence images for different tweezer patterns: **a**. 8 by 8 pattern with  $10 \mu\text{m}$  spacing, used for the Raman sideband cooling measurements. **c**. Two rows of 25 traps each, for Rydberg dressing experiments. **e**. 2 by 2 blocks used for measuring Rydberg blockade. Multiple copies increase the statistics per experimental realisation. **b**, **d**, **f**: Single shot fluorescence pictures. **g** and **h**: Averaged fluorescence images, demonstrating flexible placement of traps.

To measure the lifetime  $\tau$  we load atoms and observe the loss depending on holding time. The lifetime is  $\tau = 80 \pm 8 \text{ s}$  with the traps continuously on and  $40 \text{ s}$  if we constantly chop the trap. In most experimental sequences the trap is only chopped during loading, state preparation and imaging, which takes  $\approx 100 \text{ ms}$ . The lifetime of  $80 \text{ s}$  is even higher than the ones observed in similar experimental setups [100, 111].

We now discuss several factors which can limit the lifetime of atoms such as collisions with other atoms, heating from the off-resonant dipole trap or parametric heating caused by amplitude noise of the trapping light.

If the trapped atoms collide with atoms from the background gas at room temperature, dominated by hydrogen, the energy transfer is much larger than the trap depth of optical dipole traps. Such a collision thus causes a loss of the trapped atom [112]. The collision rate depends on the pressure in the UHV chamber. The use of a Zeeman slower and multiple differential pumping stages, as presented in Chapter 3 is a significant advantage compared to systems where the MOT is directly loaded from an alkali background gas, limiting the lifetime to a few seconds [21, 108]. Experiments including differential pumping stages observed atom lifetimes of up to ten minutes [113], which agrees with estimates of the loss rate caused by collisions with the background gas [112, 114].

Different experimental approaches are needed if the vacuum quality and background gas become a limitation. For example cryogenic systems can achieve orders of magnitude lower pressures, thus drastically reducing the background gas collision limited vacuum lifetime. It was also reported that collisions with the atomic beam can cause atom loss, depending

on the temperature of the atomic source [111]. While the atomic shutter was closed for the lifetime measurement after loading the MOT, in the usual operation of the experiment, the shutter is always open, since the design does not allow for fast shuttering in the Hertz range.

Another limiting factor can be heating from the optical trap, with a rate given by  $\dot{T} = 1/3 \cdot T_{\text{recoil}} \cdot \Gamma_{\text{scatter}}$  [9]. In our case we calculate a heating rate of  $\dot{T} = 2.1 \mu\text{K/s}$  with a recoil temperature of  $T_{\text{recoil}} = 777 \text{ nK}$  and a scattering rate of  $\Gamma_{\text{scatter}} = 2\pi \cdot 1.3 \text{ Hz}$  for a trap depth of 1 mK. This heating rate would imply an atom lifetime of up to about 10 minutes which does not agree with the observed lifetime of 80 s. We thus conclude that we are not limited by heating from the off-resonant trap.

Another heating mechanism is parametric heating, caused by amplitude noise. This is characterised by the relative intensity noise (RIN) spectrum of the light. Noise at twice the trap frequency  $\omega_{tr}$  can lead to parametric heating, driving transitions between vibrational levels of the trapping potential. Often AOMs are used for intensity stabilisation, which are limited to a band-width of about about 100 kHz. Typical radial trap frequencies in optical tweezers are in the same range, making it difficult to actively stabilise amplitude noise at twice the trap frequencies. Thus one has to rely on low RIN sources or use more involved stabilisation schemes [115]. We measured the RIN noise<sup>7</sup> of our trapping laser and calculate the heating rate  $\Gamma = \hbar\pi\omega_{tr}^3/4 \cdot S_{\epsilon}(2\omega_{tr})$  with the one-sided power spectral density  $S_{\epsilon}$  [116, 117]. The resulting rate  $\Gamma$  is on the order of 100 nK/s and is not limiting the atom lifetime in our case. Note that also amplitude and pointing noise caused by the spatial light modulator can heat the atoms [118].

In conclusion we achieved a lifetime which is one order of magnitude higher than the ones presented in other tweezer experiments [21, 100, 108]. We suspect to be limited by background gas collisions, as this loss mechanism agrees best with our measured loss rate. The higher rate compared to measurements from other experiments might be explained by the large amount of components and materials used inside the UHV chamber.

### 4.3 State preparation

Once single atoms are trapped, the next step is to prepare them in a well-defined single Zeeman  $m_F$  sub-state. This is an important requirement for coherent excitation to Rydberg states.

Usually one of the following pairs of states is used as a qubit: The stretched states  $F = 2, m_F = 2$  and  $F = 1, m_F = 1$  or the states with  $m_F = 0$ , which are insensitive to magnetic fields. The advantage of the stretched states is that they are also good states in the  $J$  basis, meaning that the  $m_F = 2$  state has a projection of the total angular quantum number of  $m_J = 1/2$ . This maximises the coupling to the Rydberg states, which are also described in the  $J$  basis. On the other hand the clock states with  $m_F = 0$  are first order insensitive to magnetic fields, suppressing magnetic field noise-induced decoherence and dephasing [34].

---

<sup>7</sup>High Finesse LWA-1k

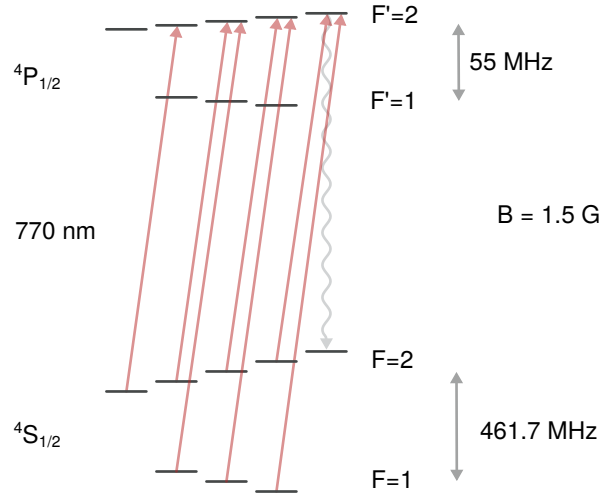


**Fig. 4.4** Level scheme for preparing the atoms in the  $F = 2, m_F = 2$  state. Light with a high degree of circular  $\sigma^+$  polarisation optically pumps the atoms to the  $F = 2, m_F = 2$  state. Atoms that decay to the  $F = 1$  ground states are repumped. A magnetic field of 1.5 G defines the quantisation axis.

We choose to use the  $m_F = 2$  states to maximise the coupling to Rydberg states. Here we restrict the discussion to  $m_F = +2$ , but a preparation of  $m_F = -2$  is analogous by rotating the quantisation field by 180 degrees, driving  $\sigma^-$  instead of  $\sigma^+$  transitions.

The scheme used is shown in Fig. 4.4. The laser couples  $\sigma^+$  transitions from  $F = 2$  to  $F' = 2$ . The atoms are successively pumped into the dark state  $F = 2, m_F = +2$ . Atoms that decay into the  $F = 1$  states are repumped with resonant light on the  $F = 1$  to  $F' = 2$  transition.

We use the GM laser on the D1 transition which is ramped from blue detuning during the GM cooling to resonance by changing the beat lock frequency. To achieve a well defined polarisation a quantisation field of 1.5 G along the MOT x beams (which is 14.5 degrees rotated to the x axis) is applied. The beams from the y and z direction are blocked with mechanical shutters<sup>8</sup> as well as the counter propagating beam on the x axis. A Glan Taylor polariser is used before the quarter waveplate to provide a high degree of circular polarisation. Similarly to the chopped loading and imaging, the state preparation is also chopped. The total duration is 300  $\mu\text{s}$  with intensities of  $0.3 I_{\text{sat}}$  for each beam.

We measure and optimise the preparation efficiency similar to References [108, 119]: We measure the optical pumping and depumping times  $\tau_{OP/DP}$ , as shown in Fig. 4.5. From those times we can extract the degree of polarisation and the steady state population in the  $F = 2, m_F = 2$  state, which corresponds to the preparation efficiency we want to determine.

The experimental sequence is as follows: After loading single atoms and state preparation,

<sup>8</sup>Uniblitz VS25 / VS14. We used Thorlabs SHB1T shutters before, which jammed several times and finally broke after one year of constant use.

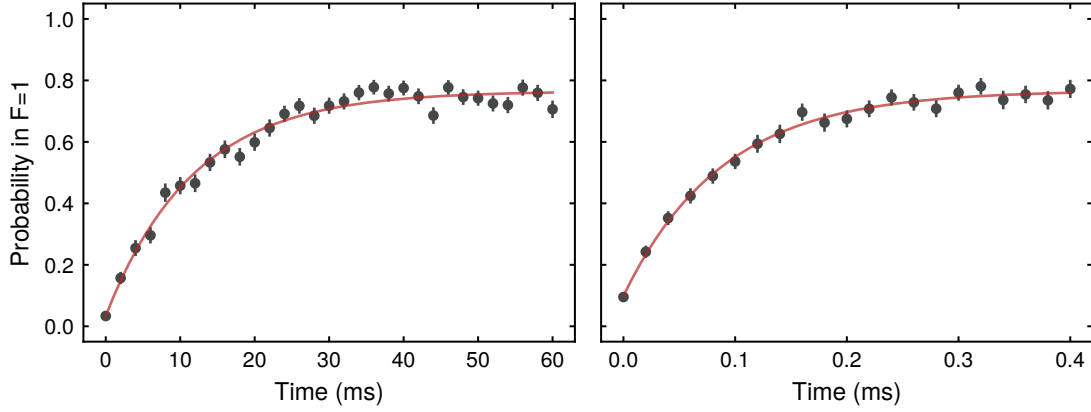


**Fig. 4.5** Characterisation of the state preparation fidelity: Measurement of the depumping time by preparing the atoms in the  $F = 2, m_F = +2$  state and using resonant light on the  $F = 2$  to  $F' = 2$  transition to depump the atoms. Only atoms in  $F = 1$  are detected. **Left:** Magnetic field aligned parallel to the pumping beams. The red line is an exponential fit with a time constant  $\tau_{DP} = 11.8 \pm 0.7$  ms. **Right:** Magnetic field rotated to mix the polarisations of the pumping light. The exponential fit shows a time constant of  $\tau_{OP} = 88 \pm 4$   $\mu$ s.

the light driving the  $F = 2$  to  $F' = 2$  transition is switched on again.

Since the atoms in  $m_F = +2$  are in a dark state for perfectly circular  $\sigma^+$  polarised light, any imperfect polarisation components will drive  $\sigma^-$  or  $\pi$  transitions. Since those transitions are not closed, the atoms will decay into the  $F = 1$  ground state after a few cycles. Afterwards we remove all atoms in the  $F = 2, m_F = +2$  state as follows: The trap is ramped to 20% of the initial trap depth. A resonant pulse on the  $F = 2, m_F = 2$  to  $F' = 3, m_{F'} = 3$  transition of the D2 line heats the atoms in  $m_F = 2$  and ejects them from the trap. Atoms in any other  $m_F$  state are not driven on a closed transition and will only scatter a few times before falling into the  $F = 1$  state. Taking a second fluorescence picture allows us to determine the depumping time  $\tau_{DP}$ .

This sequence is performed twice, where the second time the quantisation field for driving the  $F = 2$  to  $F' = 2$  transition after the state preparation is rotated by 45 degrees, mixing all polarisations. From those measurements the optical pumping and depumping times  $\tau_{OP}$  and  $\tau_{DP}$  can be extracted. Given those, the preparation efficiency can be estimated as  $P(F = 2, m_F = 2) = 1 - \tau_{OP}/\tau_{DP} = 99.25 \pm 0.06\%$  [119].

The observed fidelity is sufficient for experiments presented in this thesis. If required, the fidelity can easily be increased: It is mainly limited by the degree of polarisation of the beams. To optimise the fidelity we optimise the quarter waveplate by hand and orient the quantisation field to maximise the depumping rate  $\tau_{DP}$ . A more precise polarisation control, using for example multiple waveplates and precise automatised rotation mounts, would allow for further increase of the fidelity. The presented scheme for preparing single atoms with high fidelity in a defined quantum state set the starting point for all following measurements.

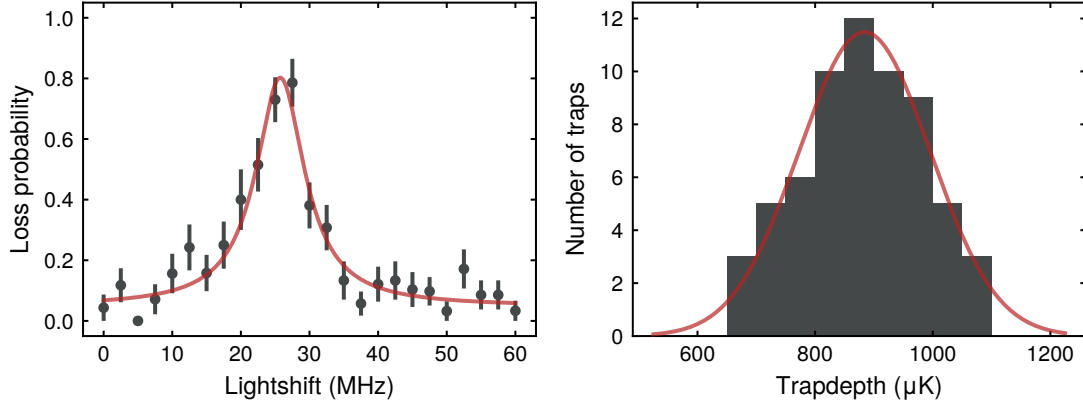


**Fig. 4.6** Spectroscopy of the trap light shift to measure the trap depth. **Left:** Spectroscopy of the  $F = 2, m_F = 2$  to  $F' = 2$  transition on the D1 line at 20% trap depth, compared to the one used for loading the atoms. The red line shows a Lorentzian fit. **Right:** Histogram of the trap depth in an 8 by 8 array. The trap depth for loading and imaging (100%) is  $906 \pm 103 \mu\text{K}$ , the red line shows a Gaussian fit, from which these numbers have been extracted.

#### 4.4 Trap depth measurement

We now determine the trap depth of the individual traps. Note that the light shift of the  $4S_{1/2}$  ground states is exactly the trap depth. We measure the AC stark shift of the  $4S_{1/2} F = 2, m_F = 2$  to  $4P_{1/2} F' = 2$  transition. With the ratio of ground to excited state shift, which we determine from a simulation (see [Appendix A.1](#)), we can extract the ground state shift. We load and prepare the atoms in the  $F = 2, m_F = 2$  ground state, as described in [Section 4.3](#). The magnetic field is rotated by 22.5 degrees and a short spectroscopy pulse on the  $4S_{1/2}, F = 2$  to  $4P_{1/2} F' = 2$  transition is applied. The rotated magnetic field mixes the polarisation and the atoms are pumped to the  $F = 1$  or other  $F = 2, m_F \neq 2$  ground states, if on resonance. Afterwards we again align the magnetic field along the direction of the laser beam and remove atoms in the  $F = 2, m_F = 2$  state with light resonant to the  $F = 2, m_F = 2$  to  $F' = 3, m_{F'} = 3$  cycling transition of the D2 line.

We calculate the ratio of the light shifts of the  $4S_{1/2}$  ground state to the  $4P_{1/2}$  excited state to be  $-5.66$  for linear polarisation at a trap wavelength of 1064 nm, as discussed in [Section 2.2](#). The minus sign indicates anti-trapping of the excited state. For a linear polarisation, both  $4S_{1/2}$  and  $4P_{1/2}$  have no differential shifts of the individual  $F$  and  $m_F$  states. We do not use the D2 line for spectroscopy, since for the  $4P_{3/2}$  manifold all  $F$  and  $m_F$  states show strong differential shifts, even for linear polarisation. The spectroscopy signal for a single trap and a histogram of the trap depth of 64 traps in an 8 by 8 pattern are shown in [Fig. 4.6](#). We measure a mean trap depth of  $906 \pm 103 \mu\text{K}$ , where the error denotes the standard deviation of averaging the 64 traps. We suspect that aberrations in the optical path of the SLM cause the observed inhomogeneities of the trap depth of 11.4%.

## 4.5 Raman sideband cooling

With the molasses cooling and state preparation described so far, single atoms in a defined  $m_F$  Zeeman sub-state state can be prepared, which is sufficient to perform first experiments with Rydberg states. However, the atoms are still in a thermal state and occupy many vibrational levels of the trap, described by a Poissonian distribution. This is a limitation for several reasons:

- **Doppler shift:** For experiments where the trap is switched off, e.g. Rabi oscillations with Rydberg states, the Doppler shift  $\Delta_D$  of the atoms is given by  $\Delta_D = \mathbf{k} \cdot \mathbf{v}$  with the wave vector  $k = 2\pi/\lambda$  and the velocity of the atoms  $\mathbf{v}$ . This shift leads to a different detuning for every experimental realisation and the averaged signal will show a damping of the Rabi oscillation. Note that only the velocity component in the direction of the light is relevant. The root mean square (RMS) velocity in one direction is given by  $v = \sqrt{k_B T/m}$  with the Boltzmann constant  $k_B$  and the mass of the atom  $m$ . For typical temperatures of  $40 \mu\text{K}$  this is a shift of  $2\pi \cdot 160 \text{ kHz}$ . Using a two photon transition with counter propagating beams can partially compensate the Doppler shift, but due to the usually large difference in wavelength the shift does not cancel completely [111].
- **Thermal broadening:** Atoms in a thermal state occupy many vibrational levels of the trap with a Poissonian distribution. The mean vibrational quantum number  $\bar{n}$  is given by  $k_B \cdot T = \hbar\omega (\bar{n} + 1/2)$  with the trap frequency  $\omega$ . Hotter atoms will thus cause a thermal broadening of the optical transition.
- **Atom recapture:** For many experiments the trap is switched off to avoid anti-trapping of the Rydberg states in a dipole trap. The switch-off time before losing atoms is limited by the temperature.
- **Trap depth:** If experiments are performed while the atoms are trapped, for example in Rydberg dressing, it is favourable to lower the trap depth. This reduces absolute inhomogeneous shifts between different traps and also cools the atoms adiabatically [120]. The minimum achievable trap depth without atom loss is limited by the initial temperature.

In conclusion, further cooling of the atoms, ideally to the vibrational ground state, not only helps with direct limitations like Doppler shifts, but also indirectly helps to reduce other effects like inhomogeneous trap shifts.

Raman sideband cooling allows for fast and effective cooling to the vibrational ground state in tight optical traps [121–123]. For optical traps the trap frequencies  $\omega$  in radial and axial direction are

$$\omega_{\text{rad}} = \sqrt{\frac{4V_0}{m\omega_0^2}} \quad \text{and} \quad \omega_{\text{ax}} = \sqrt{\frac{2V_0}{mz_r^2}} \quad (4.1)$$

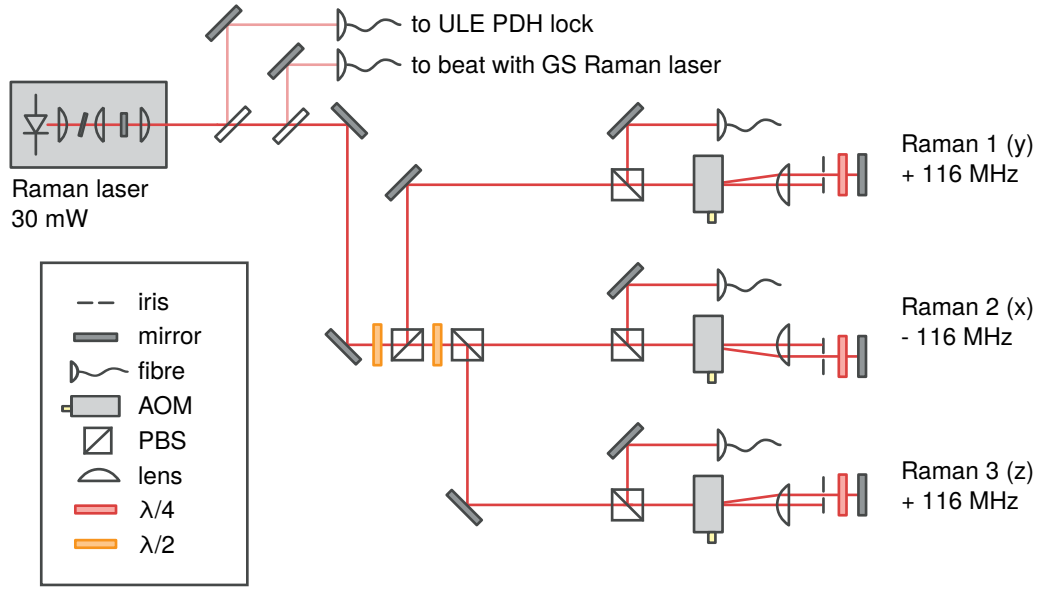


**Fig. 4.7** Raman laser setup. The laser is locked onto the ULE cavity and also used as reference for the lock of a second Raman laser for ground state manipulation. Three AOMs in double pass are used to bridge the ground state splitting of  $^{39}\text{K}$ . On the experimental table each beam is focussed to a  $250\ \mu\text{m}$  waist and onto the atoms.

with the trap depth  $V_0$ , the mass of the atoms  $m$  and waist of the beam  $\omega_0$ .  $z_r = \pi\omega^2/\lambda$  is the Rayleigh range. For tightly focussed tweezers with the waist on the order of the wavelength ( $\omega \approx \lambda$ ), the ratio of trap frequencies is  $\omega_{\text{rad}}/\omega_{\text{ax}} \approx 4.5$ . The weaker axial confinement cause breakdown of Lamb-Dicke regime, needed for efficient groundstate cooling. Most implementations of ground state cooling in optical tweezers used single or few atoms [79, 124–126]. Here we implement Raman sideband cooling for a large scale array of 64 individual traps. Ground state cooling also demonstrated for alkaline-earth atoms, where a narrow optical transition is used for direct sideband cooling [54].

#### 4.5.1 Experimental setup

The Raman laser is a linear interference filter stabilised diode laser, identical to the MOT laser, described in Section 3.3. The laser is locked to the reference cavity, described in Section 5.2, using a Pound Drever Hall locking scheme. The sidebands of 7 MHz for the lock are generated using an EOM.

The setup of the laser is shown in Fig. 4.7 and the orientation of the beams onto the atoms in Fig. 4.8.

For both Raman sideband cooling and sideband spectroscopy we use three orthogonal beams called Raman 1 (R1), Raman 2 (R2) and Raman 3 (R3). This allows to address either only the radial (R1 + R2) or both radial and axial (R2 + R3) trap axes. All beams are derived from the same laser using AOMs. Two independent RF sources are used to drive

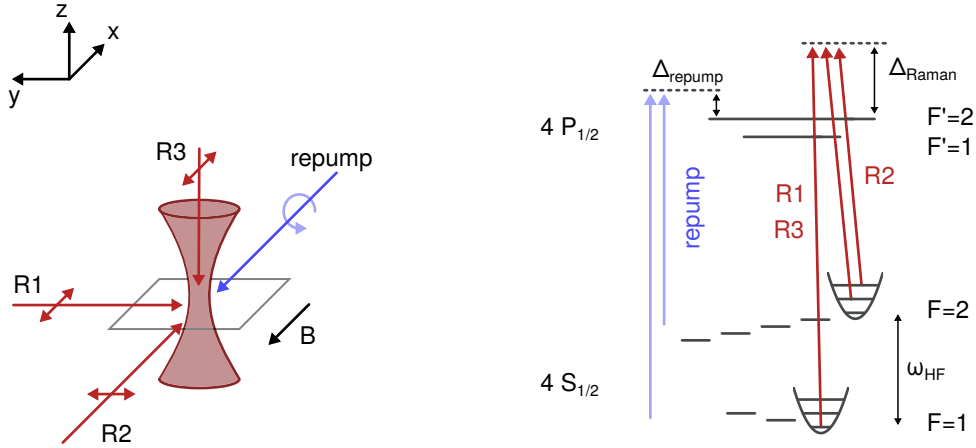


**Fig. 4.8** **Left:** Orientation of the Raman beams around the chamber. A quantisation field of 1.5 G is used along the  $x$  axis. The repumpers have circular polarisation and drive  $\sigma^+$  transitions. All Raman beams are linearly polarised to prevent vector light shifts. R1 and R2 are aligned in the  $x$ - $y$  plane and only couple radial sidebands. R3 is aligned along  $z$  and, with R2, addresses the axial sidebands. **Right:** Level scheme. The Raman laser drives transitions from  $F = 2, m_F = +2, n$  to  $F = 1, m_F = +1, n - \Delta n$ . In the radial directions the  $\Delta n=1$  transitions are addressed, in the axial direction the  $\Delta n=1$  to  $\Delta n=4$  sidebands are used for cooling. The Raman laser is blue detuned by 40 GHz from the D1 line. To reduce heating from the anti-trapped excited states, both  $F$  and  $m_F$  repumper are detuned by  $\approx 80$  MHz from the  $F = 2$  to  $F' = 2$  or  $F = 1$  to  $F' = 2$  transitions, respectively.

either the AOMs of R1 and R2 or R2 and R3 with the same frequency of 116 MHz, bridging the ground state transition from  $F = 2, m_F = +2$  to  $F = 1, m_F = +1$  of 464.7 MHz at 1.5 G quantisation field, shown in Fig. 4.8.

The laser is  $\Delta_R = 40$  GHz blue detuned from the  $4S_{1/2}$  to  $4P_{1/2}$  transition. All Raman beams have linear polarisation, aligned in plane (R1 and R2) or along the quantisation axis (R3), to prevent vector light shifts [12]. The beams for both  $F$  and  $m_F$  repumping are the same beams as for state preparation.

The beam waists at the atoms are  $250 \mu\text{m}$  with intensities of  $1.6 \text{ W}/\text{cm}^2$  (R2) and  $0.9 \text{ W}/\text{cm}^2$  (R1 + R3). We measure Rabi frequencies of  $2\pi \cdot 43 \text{ kHz}$  for driving the  $F = 2, m_F = +2$  to  $F = 1, m_F = +1$  ground state transition.

The optical repumpers (OP) for RSC are the same beams as used for state preparation, but blue detuned  $\Delta_{OP} = 80 \pm 30$  MHz from the in-trap  $4S_{1/2}$  to  $4P_{1/2}$ ,  $F = 2$  resonance, to prevent heating from the anti-trapped excited states [12]. The error denotes the standard deviation from averaging 64 individual tweezers. Each repumper has an intensity of  $4 \text{ mW}/\text{cm}^2$ .

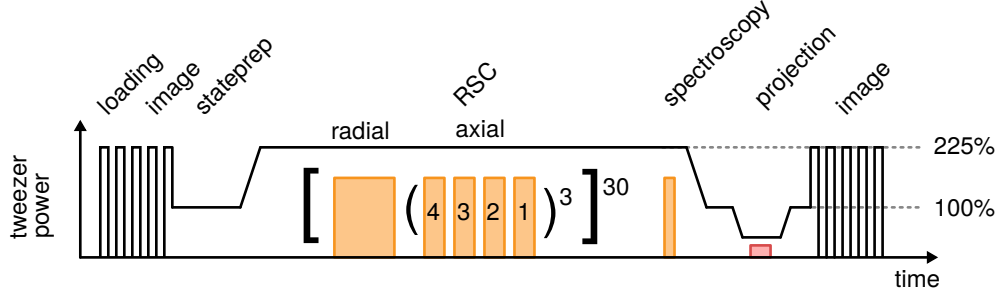


**Fig. 4.9** Experimental sequence. The chopping and ramps of the tweezer light (black lines), the Raman light for cooling and spectroscopy (yellow) and the projection pulse to heat atoms in  $F = 2, m_F = 2$  (red) are shown. The numbers for the axial Raman sideband cooling indicate the  $n^{\text{th}}$  sideband used for cooling, the brackets indicate the repetition of cooling cycles.

#### 4.5.2 Experimental sequence

In Fig. 4.9 the experimental sequence is depicted. Loading and imaging single atoms is performed chopped [75, 81]. For Raman sideband cooling and spectroscopy the trap is ramped to 225% of the initial power and not chopped, which increases the trapping frequencies by a factor of 1.5. The laser power when ramped to 225% is equal to the peak power during chopping for loading and imaging and thus imposes no limit for scaling the amount of tweezers. Raman sideband cooling consist of 30 cooling cycles. For each cycle we cool the radial axes for 2 ms with ten chirps of 200  $\mu\text{s}$  over 120 kHz to cover the inhomogeneities between the different traps. Then we apply three sub-cycles of axial cooling, each cooling for 200  $\mu\text{s}$  on the 4<sup>th</sup> to 1<sup>st</sup> axial sideband [126]. The whole process takes 150 ms, including switching times. The detuned optical repumpers for the  $F$  and  $m_F$  states are on during the whole cooling sequence.

#### 4.5.3 Sideband spectroscopy

To quantify the cooling efficiency, we perform spectroscopy of the motional sidebands. After Raman sideband cooling, we apply a spectroscopy pulse to transfer the atoms from the  $F = 2, m_F = 2$  to the  $F = 1, m_F = 1$  state. The spectroscopy is performed in the same conditions as cooling with the tweezers at 225% of the initial power. Afterwards the traps are ramped to 20% power and we remove atoms in  $F = 2, m_F = +2$  using resonant D2 light on the  $F = 2, m_F = 2$  to  $F' = 3, m_{F'} = +3$  cycling transition to only image the  $F = 1$  population. For radial spectroscopy we use a  $\approx \pi/2$  pulse on the carrier while for the axial spectroscopy we apply a  $\approx \pi$  pulse on the carrier. Both pulses are less than  $\pi/2$  pulses on the respective sidebands. The results for radial and axial spectroscopy are shown in Fig. 4.10. From the sideband asymmetry we calculate the mean vibrational quantum number  $\bar{n}$  by  $\bar{n}/(\bar{n} + 1) = I_{\text{blue}}/I_{\text{red}}$  with the strength of the blue and red sideband  $I_{\text{blue/red}}$  [121]. The radial axes are cooled to  $\langle \bar{n}_{\text{rad}} \rangle = 0.225 \pm 0.217$ , where  $\langle \cdot \rangle$  indicates the averaging over individual tweezers, which dominates the standard deviation. The large uncertainty is explained by the long-tailed distribution of the  $\bar{n}_{\text{rad}}$  with a median of 0.142. Due to the

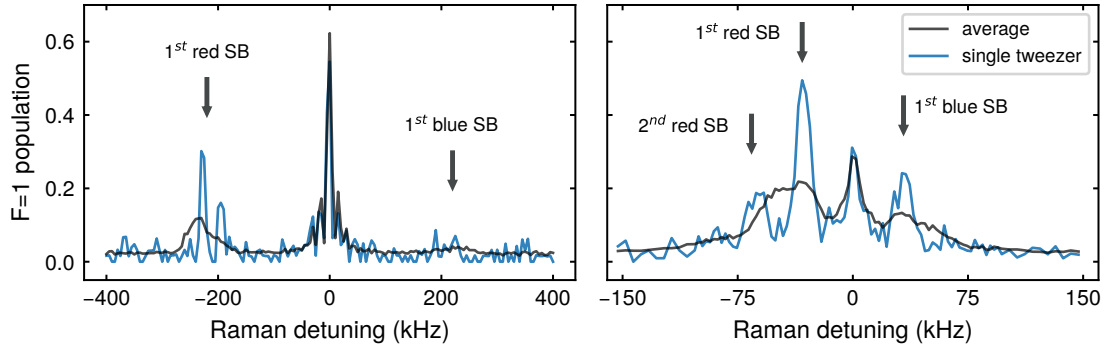


**Fig. 4.10** **Left:** Radial spectroscopy of a single tweezer of the array (blue) and the averaged signal over all tweezers (black). The two peaks indicate a slightly elliptic tweezer with different radial trap frequencies. **Right:** Axial spectroscopy for a single tweezer (blue) and averaged over all tweezers (black). For the single tweezer higher sidebands are also resolved.

lower trapping frequency in the axial direction we initially start outside the Lamb Dicke regime [126]. However, after cooling a clear asymmetry in the red and blue sideband is visible. The calculated mean vibrational quantum number is  $\langle \bar{n}_{ax} \rangle = 1.04 \pm 1.05$  (median of 0.742). The best cooling for a single tweezer is  $\bar{n}_{rad} = 0.13$  and  $\bar{n}_{ax} = 0.23$ , which gives a ground state probability of 69%. This is slightly lower than the best reported ground state occupations after Raman sideband cooling of  $\approx 90\%$ , achieved for single optical tweezers with rubidium and sodium [124, 126]. However, cooling is optimised for best average performance of the whole array in our setup.

Notably, we can also achieve comparable cooling performance using only two Raman beams. We apply the same sequence for cooling as before, but only use the beams with projection on all trap axes (R2 + R3) for both radial and axial cooling. However, this configuration is not optimal for radial spectroscopy in a non-sideband cooled case, since higher axial and radial modes will overlap. For all work done in this thesis we use all three Raman beams to individually address the radial or axial trap axes for both cooling and spectroscopy.

To determine the Rabi frequencies when driving the ground state transitions, we measure coherent Rabi oscillations on the carrier and red sideband, shown in Fig. 4.11. We see a clear improvement of coherent carrier oscillations for sideband cooled atoms. Oscillations on the motional sideband are only visible for cooled atoms. Due to the spread of trap frequencies it is not possible to drive all atoms on resonance simultaneously. We thus observe a strong damping of the oscillations when averaging all tweezers. However, single tweezers which are driven on resonance show less damped oscillations. We measure a Rabi frequency of  $2\pi \cdot 70$  kHz for the carrier and  $2\pi \cdot 22$  kHz on the sideband.

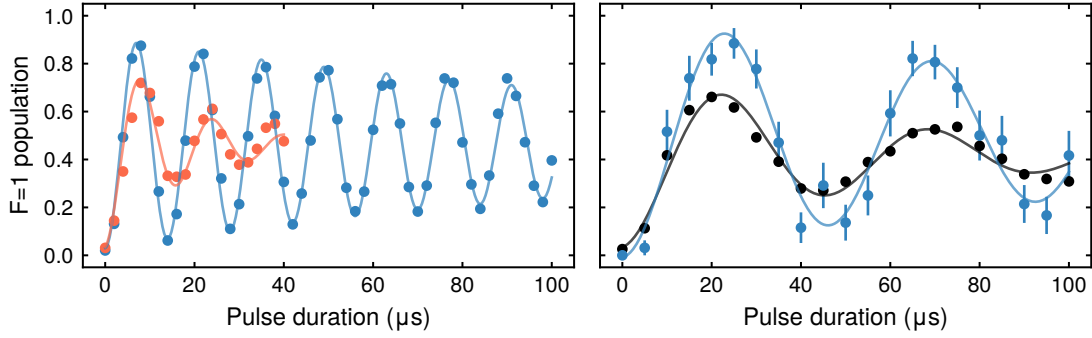


**Fig. 4.11** **Left:** Rabi oscillations on carrier (radial Raman beams) before (red) and after (blue) sideband cooling. **Right:** Rabi oscillations on the red radial sideband after RSC for a single tweezer (blue) and averaged for all tweezers (black)

## 4.6 Rampdown

An important measure is the lowest trap depth at which the atoms can be held. In our case a low trap depth is especially important for Rydberg dressing, which is performed in-trap. Lower trap depths have two advantages for those experiments: If the trap depth  $U_0$  is lowered adiabatically, the thermal distribution with temperature  $T$  will follow as  $T \propto \sqrt{U_0}$ , thus adiabatically cooling the atoms [120]. Furthermore, the absolute value of any inhomogeneous light shifts between individual traps will also decrease linearly with the light shift of the traps and thus linearly with the optical power. We can extract the temperature by comparing the survival probability as a function of the trap depth to a theoretical model.

### 4.6.1 Measuring the survival probability after rampdown

We initially confine atoms in traps of  $\approx 1$  mK. This is the same trap depth used for loading and imaging and will be referred to as the initial trap depth in the following. The trap power is lowered linearly in 50 ms and the atoms are held for additional 50 ms before the traps are ramped up again and a second picture is taken. Since for these measurements a high dynamic range of the stabilisation loop is crucial, we use the dual stage intensity stabilisation, as described in Section 4.1.

To avoid heating the atoms when changing the trapping potential, the ramps need to be adiabatic. In order to achieve adiabaticity, the change of the trap frequency  $\dot{\omega}$  needs to be much larger than  $\omega^2$  [111]. This is fulfilled even for the lower axial trap frequency at low powers, which are on the order of 1 kHz.

In Fig. 4.12 the survival probability as a function of the optical power is shown. If we do not apply any cooling, we start losing atoms at approximately 10% of the initial tweezer power, corresponding to a depth of about  $100 \mu\text{K}$ . While only cooling the radial modes improves this limit to a few percent of the initial power, full cooling of all axes allows us to hold the atoms even at about 5 permil of the initial power, at a trap depth of  $3.7 \mu\text{K}$ . This

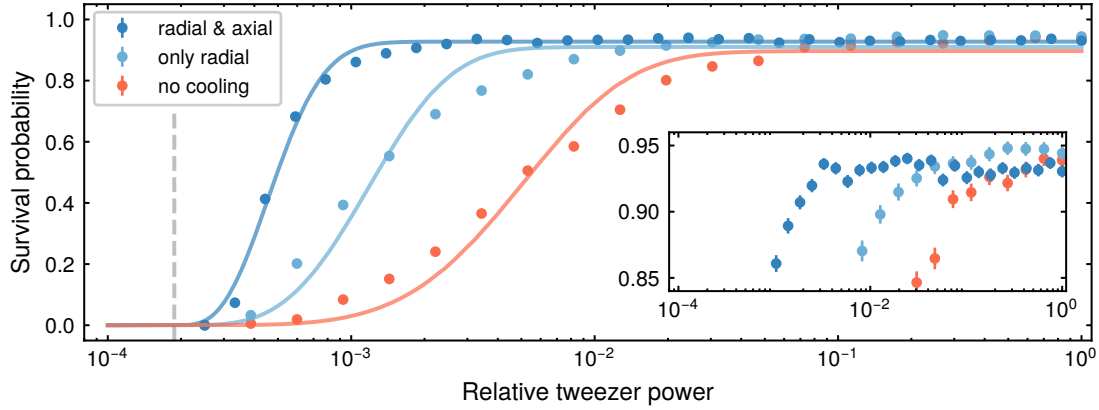


**Fig. 4.12** Survival probability for decreasing the trap depth compared to tweezer power for loading the atoms. The data is the average of 64 tweezers with RSC (dark blue), RSC only on the radial axis (light blue) and no additional cooling (orange). The solid lines are theory fits of a Boltzmann distribution, taking into account gravity. Due to gravity for powers lower than  $2 \cdot 10^{-4}$  (dashed grey line) the atoms are not confined in  $z$ . The inset shows a magnified part of the y axis.

is an improvement of two orders of magnitude compared to the uncooled case. The final trap depth is limited by gravity: For powers below  $2 \cdot 10^{-4}$  of the initial one the atoms are no longer confined in the axial direction. Further improvement would be possible by the addition of a vertical lattice [127].

#### 4.6.2 Simulating the survival probability after rampdown

To model the survival probability in the rampdown measurement, we exactly follow the analysis from Tuchendler et al. [120]:

We first calculate the trap depth as a function of the tweezer power, taking into account gravity in the axial direction. For trap depth lower than  $\approx 10 \mu\text{K}$  this starts to deviate from a linear scaling, as shown in Fig. 4.13. At a factor of  $2 \cdot 10^{-4}$  of the initial power  $P_0$  (with  $V_0(P_0) = 1 \text{ mK}$ ), gravity opens the trap and the atoms are not confined in the axial direction any more.

Secondly, we calculate the minimum trap depth  $V_{0,\text{esc}}$  at which the atoms are lost depending on their initial energy  $E_i$ . For this we numerically solve the constant action equation  $S(E_i, V_{0,i}) = S(V_{0,\text{esc}}, V_{0,\text{esc}})$ . The action  $S$  is defined as

$$S = \int_0^{x_{\text{max}}} \sqrt{2m[E - V_0(x)]} dx \quad (4.2)$$

with Energy  $E$  and axial potential  $V(x)$ .  $x_{\text{max}}$  is the point where the atom has no kinetic

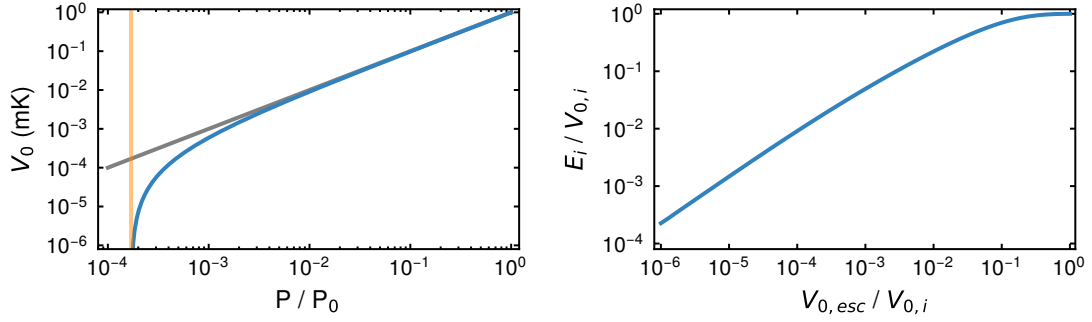


**Fig. 4.13** **Left:** Trap depth  $V_0$  as a function of power including gravity (blue) and without gravity (grey). For  $2 \cdot 10^{-4}$  gravity opens the trap and atoms are no longer confined in the axial direction (orange line). **Right:** Mapping from  $V_{0,esc}$  to  $E_i$ .

energy. The survival probability

$$P_{\text{surv}}(E) = \int_0^E f(E') dE' \quad (4.3)$$

is given by integrating the Maxwell Boltzmann distribution

$$f(E) = \frac{E^2}{2(k_B T)^{3/2}} \cdot \exp\left(-\frac{E}{k_B T}\right). \quad (4.4)$$

The fitted curves shown in Fig. 4.12 are the extracted survival probabilities for the average of all tweezers as a function of the optical power.

We attribute the slight differences between theory and measurements to inhomogeneities between the individual traps, which will broaden the measured survival probability.

We extract average temperatures of  $T = 3.31 \pm 0.08 \mu\text{K}$ ,  $11.8 \pm 0.8 \mu\text{K}$  and  $40.7 \pm 2.2 \mu\text{K}$  at the initial trap depth of  $V_0 = 906 \mu\text{K}$  for the fully Raman cooled, only radial Raman cooled and molasses-only cooled atoms, respectively.

## 4.7 Switchoff

For many experiments it is necessary to switch the traps off for a short duration of a few microseconds. This is for example done for resonant excitation to Rydberg states, which are anti-trapped by the tweezers and would be lost if the tweezers stayed on. Also for coherent Rabi oscillations between Rydberg and ground states, presented in Section 6.1, are performed with the trap switched off. We now want to characterise the survival probability of atoms if the trap is turned off temporarily and show the improvements when using RSC. In a first measurement, the traps are adiabatically ramped to 20% of the initial power. The traps are switched off for a variable time and the recaptured atoms are imaged. We measure the recapture probability for molasses cooled atoms after loading, for RSC only on

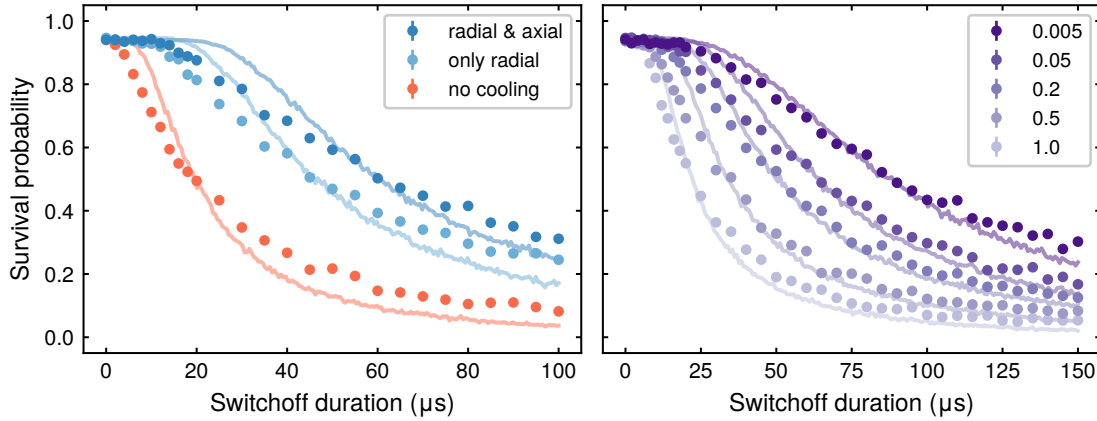


**Fig. 4.14** Survival probability for different trap-off times. **Left:** Comparison of atoms with RSC, with only RSC of the radial direction and with no additional cooling. **Right:** RSC of radial and axial axes, varying trap power before the switch off. Measurements are labelled by the rampdown factor from 1 down to 5 permil. The fits are numerical simulations of the survival probability.

the radial axis and RSC of the axial and radial axes, as shown in Fig. 4.14. In the molasses cooled case we can recapture atoms without additional loss up to  $2 \mu\text{s}$ , while RSC allows us to recapture the atoms without additional loss for times up to  $15 \mu\text{s}$ .

We simulate the recapture probability with a classical Monte Carlo simulation [100, 120, 128]. Given a temperature  $T$  we draw the initial position  $x$  of the atom from a normal distribution with a standard deviation of  $\sigma_x = \sqrt{k_B \cdot T / m \cdot \omega_i^2}$  with the Boltzmann constant  $k_B$ , the mass of the atom  $m$  and the trap frequencies  $\omega_i$  in the axial or radial direction. The initial velocity is drawn from a normal distribution with standard deviation  $\sigma_v = \sqrt{k_B \cdot T / m}$ . We calculate the final position after a time  $t$  with the classical equation of motion. The total energy at the time  $t$  is given by the sum of kinetic energy and potential energy, which is given by the trapping potential including gravity. An atom is lost if the energy is larger than the trap depth. This simulation is repeated for 5000 random realisations and the binary recapture value of all realisations is averaged. We fit this to the measurement by minimising the square of the residuals (least-square fit) with the temperature  $T$  as the only free parameter.

We extract temperatures of  $9.3 \mu\text{K}$  without and  $1.4 \mu\text{K}$  with RSC for a trap depth of  $V_0 \approx 200 \mu\text{K}$  before the switch off. Note that the temperature  $T$  scales with the trap depth  $V_0$  as  $T \propto \sqrt{V_0}$ , assuming an adiabatic change of the trap [120]. We measure this behaviour in a second switchoff measurement where we always apply RSC and vary the trap depth before switchoff down to a few permil of the initial one, as shown in Fig. 4.14. We clearly observe longer recapture times for lower trap depth and thus lower temperatures. At the lowest values of 5 permil we extract a temperature of  $\approx 200 \text{ nK}$ , consistent with the expected root scaling of the temperature. The atoms can be recaptured without additional loss up to  $25 \mu\text{s}$ , an improvement of one order of magnitude compared to the non sideband cooled case.

## 4.8 Driving ground state transitions

The same concept of Raman transitions as used for Raman sideband cooling can be employed for coherent ground state manipulation. Here a pair of co-propagating beams is used. The difference wave vector  $\Delta k \approx 10 \text{ m}^{-1}$  is given by the ground state microwave transition of 461.7 MHz. Hence the Lamb Dicke factor is negligible, since the wave vector  $\Delta k$  is orders of magnitude larger than the extent of the ground state wave function. Thus no motional sidebands can be driven, which allows for high fidelity coherent ground state manipulation. Note that coherent driving is also possible with the orthogonal Raman beams of the cooling setup, but strongly limited by off-resonant coupling to the motional sidebands. Alternatively one can directly use microwave radiation, coupled into the vacuum chamber via a horn or antenna to directly drive the ground state transition. We did not use this approach since many electronics and especially the high power ALS laser are very sensitive to radio frequency radiation [129].

### 4.8.1 Laser setup

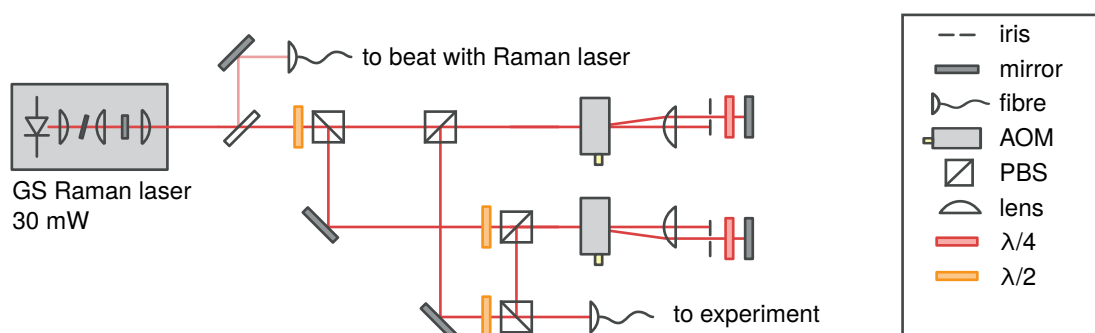


**Fig. 4.15** Raman laser setup for driving ground state transitions. The laser is frequency-locked to the Raman cooling laser, which is stabilised to the ULE reference cavity. Two AOMs in double pass configuration bridge the ground state splitting. One polarisation-maintaining fibre is used with orthogonal linear polarisations.

The Laser is identical to the one used for Raman sideband cooling. It is offset-locked by 50 MHz to the Raman cooling laser, which is locked to the ULE reference cavity, transferring the stability of the reference cavity to this laser.

In order to bridge the ground state energy difference two AOMs in double pass configuration are used. One RF generator<sup>9</sup> drives both AOMs. This allows for frequency and phase control of the light by phase modulation of the RF signal. A phase change of the AOM frequencies will also change the phase of the effective microwave field driving the atomic transition. Both beams are combined with orthogonal polarisations and sent to the experiment in a single polarisation maintaining fibre. The use of only one laser in addition with

<sup>9</sup>Stanford Research Systems SG382

a single RF source for both AOMs is inherently phase stable. The use of the same fibre cancels fibre-induced frequency noise in the Raman configuration.

The beams are aligned along the  $y$  axis with orthogonal linear polarisations. The use of linear polarisations prevent vector light shifts [12]. The quantisation axis is aligned along the  $x$  direction, such that ground state transitions with  $\Delta m_F = \pm 1$  are driven. If the quantisation field is aligned along the  $y$  axis we couple  $\Delta m_F = 0, \pm 2$  ground state transitions. However, for all experiments in this thesis the quantisation field was aligned along  $y$ , using the states  $F = 2, m_F = 2$  and  $F = 1, m_F = 1$  as qubit states.

To increase the homogeneity over the array, the beam is shaped using an anamorphic prism pair and has  $1/e^2$  diameters of  $500 \mu\text{m}$  along  $z$  and  $1000 \mu\text{m}$  along  $x$ .

### 4.8.2 Characterisation

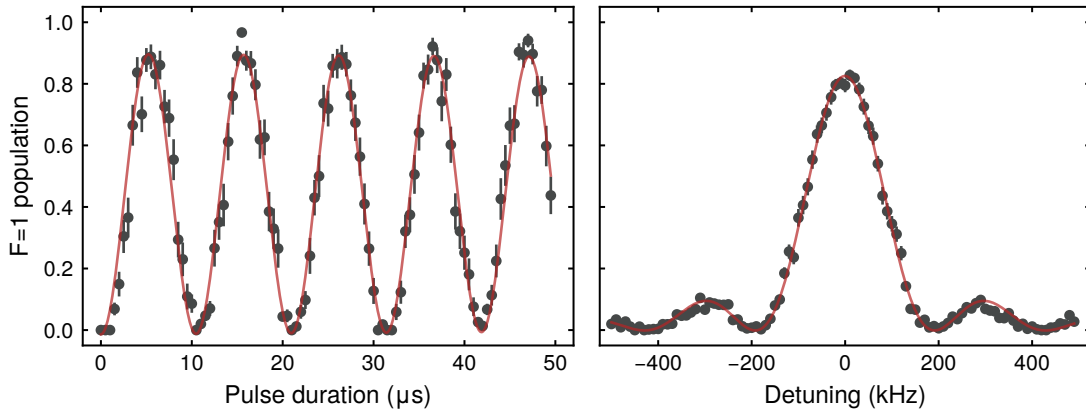


**Fig. 4.16** **Left:** Ground state Rabi oscillations between  $F = 2, m_F = +2$  and  $F = 1, m_F = +1$ . Averaged signal for 5 tweezers along the  $y$  axis. A fitted oscillation gives a Rabi frequency of  $2\pi \cdot 96 \text{ kHz}$ . **Right:** Frequency scan for a fixed pulse duration of  $5 \mu\text{s}$  for the same 5 tweezers. The fit shows the characteristic sinc function, as expected for rectangular pulses. The reduction in oscillation amplitude is caused by imperfections of the imaging, leading to an atom loss of about 5%.

Since the characterisation of the coherent ground state control was done at an earlier stage of building the experiment, a different Raman detuning of  $\Delta_R = 16.5 \text{ GHz}$  was used. We later changed this to  $40 \text{ GHz}$ , which was used for all other measurements presented in this thesis. However, the following results are still valid and a higher detuning can be compensated by increased laser power.

The sequence used for the following measurements is as follows: Atoms are trapped in a  $9$  by  $5$  array with  $15 \mu\text{m}$  spacing. The large spacing with an asymmetry along the  $x$  axis is chosen to be sensitive to spatial changes of the Rabi frequency due to the Gaussian beam profile. Depending on the experiment, several Raman pulses are applied, driving the  $F = 2, m_F = +2$  to  $F = 1, m_F = +1$  transition. To detect the population in the  $F = 1, m_F = +1$  state the tweezers are ramped to 20% power and resonant light on the

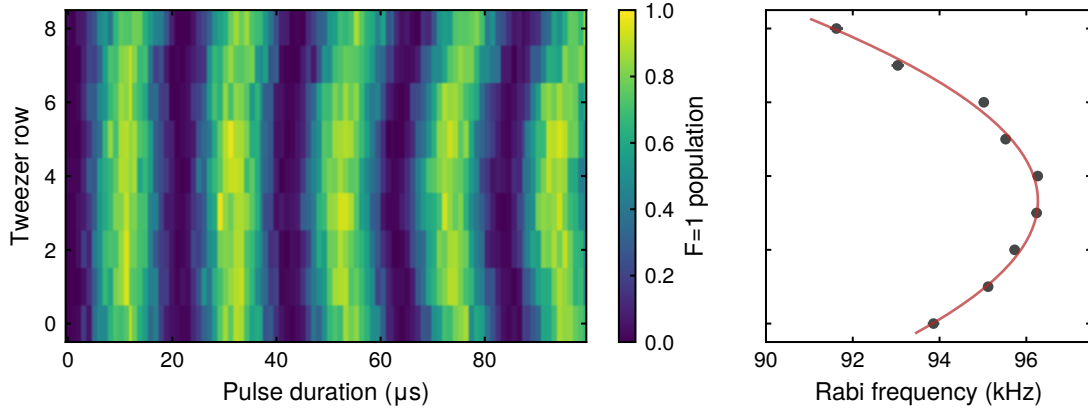


**Fig. 4.17 Left:** Rabi oscillations between the  $F = 2, m_F = +2$  and  $F = 1, m_F = +1$  states of a 9 by 5 tweezer array. Each row of tweezers is averaged. The intensity profile of the Raman beam that is aligned onto the center of the array is visible in the slightly different Rabi frequencies. **Right:** Rabi frequencies extracted from fits depending on the position. The root of a Gaussian profile gives a beam waist of  $417 \pm 11 \mu\text{m}$  along the x direction.

$F = 2, m_F = +2$  to  $F' = 3, m_{F'} = +3$  cycling transition is used to heat atoms out of the trap. Atoms in  $F = 2$  but  $m_F \neq 2$  are not kicked out but will decay to  $F = 1$  instead, creating an artificial constant offset. This error is small, as shown in Section 4.3.

In a first measurement we perform Rabi oscillations between the ground states, shown in Fig. 4.16. All Raman pulses are rectangular pulses. We always average rows of 5 atoms along the y direction, which are aligned along the propagation direction of the Raman beams. The measured Rabi frequency is  $2\pi \cdot 96$  kHz. Not visible is the dephasing of the oscillations which happens on a longer timescale of  $\approx 500 \mu\text{s}$ . This is likely limited by intensity fluctuations. Also shown is a detuning scan for a fixed pulse length of  $5 \mu\text{s}$  and a fit showing the characteristic  $\text{sinc}(f)^2$  shape, which we expect for rectangular pulses.

Due to the Gaussian beam profile of the Raman beams the Rabi frequency will vary along the x direction. When averaging the rows of the pattern the slight difference in the oscillation frequency becomes visible after several oscillations, as shown in Fig. 4.17. We fit the square of a Gaussian profile to the extracted Rabi frequencies and extract a beam waist of  $417 \pm 11 \mu\text{m}$ . The variation over the 9 rows of tweezers, corresponding to a distance of  $120 \mu\text{m}$ , is 2.8%.

We now want to characterise the dephasing and decay times, using Ramsey measurements. In a first experiment we measure the dephasing time. Two  $\pi/2$  pulses with a free evolution time between the pulses are applied, with a detuning of the Raman beams from the ground state resonance of 30 kHz. We observe oscillations at this detuning with a Gaussian decay of  $98 \pm 4 \mu\text{s}$ , shown in Fig. 4.18.

This measurement is limited by shot-to-shot changes of the magnetic field. Those fluctuations are usually caused by the 50 Hz power grid and can be modelled by averaging many oscillations with different frequencies that are drawn from a normal distribution. For a cen-

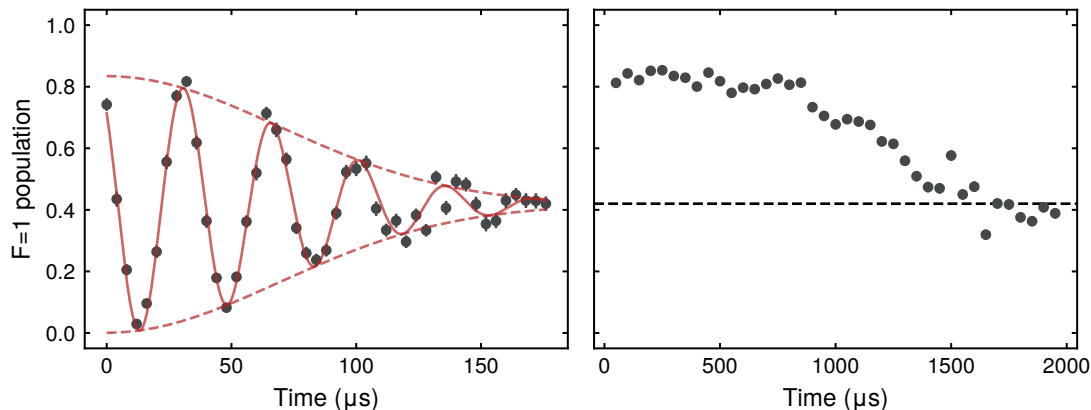


**Fig. 4.18** **Left:** Ramsey oscillations for a detuning from resonance of 30 kHz. The fit shows oscillation of 30 kHz with a Gaussian decay of  $98 \pm 4 \mu\text{s}$ , caused by magnetic field noise. **Right:** Spin echo signal with one  $\pi$  echo pulse. The phase of the last  $\pi/2$  pulse is changed by 180 degrees, resulting in a full population inversion for no decoherence. The signal decays on a longer time scale of  $\approx 1$  ms.

tre frequency of  $2\pi \cdot 30$  kHz and a standard deviation of  $2\pi \cdot 2.5$  kHz we predict a dephasing time of  $\approx 100 \mu\text{s}$ . The magnetic field sensitivity of the  $F = 2, m_F = +2$  to  $F = 1, m_F = +1$  transition is  $3 \cdot 0.7$  MHz/G, resulting in a magnetic field root mean square noise of 1 mG. Using a spin echo  $\pi$  pulse in between the  $\pi/2$  pulses these shot-to-shot fluctuations can be cancelled. Here all pulses are on resonance and the phase of the last  $\pi/2$  is 180 degrees with respect to the other pulses. As shown in Fig. 4.18, the echo pulse cancels any static changes and the signal decays on a time scale of 1 ms, ten times longer than for the Ramsey measurement. The rephasing is still limited by non-static fluctuations on this time scale, likely changes of the power grid at 50 Hz and harmonics. Using multiple echo pulses we can extend this time to 2 ms for 2 echos or 3 ms for 3 echos. A variety of so-called dynamic decoupling schemes exist, which build on this approach of quickly rephasing the system, but were not employed in this work [130].

The dephasing and decoherence time can be improved by the following techniques:

- As discussed in Section 4.3, the  $m_F = 0$  states can be used. The so-called clock transition with  $\Delta m_F = 0$  is first order insensitive to magnetic fields, allowing for much longer coherence times [34, 131].
- The experimental cycle can be paused before the field sensitive part, here the Ramsey sequence, to wait for a zero crossing of the mains 50 Hz oscillation. The sequence is then continued in-phase with the power grid, removing shot-to-shot variations. This so-called line-trigger has not been implemented in the experiment so far, but will be for future work.
- Active stabilisation of the magnetic field or feed-forward techniques can be used to actively stabilise the magnetic field [132].

In conclusion we have demonstrated coherent control of ground state atoms, using the  $F = 2, m_F = +2$  and  $F = 1, m_F = +1$  states as qubit states. We characterised experimental imperfections due to the Gaussian beam profile. By measuring the dephasing time in a Ramsey experiment, we estimated the magnetic field noise. Using a spin echo technique we showed how this time can be extended by one order of magnitude.

## **Part II**

# **Rydberg atoms**



## Chapter 5

### UV laser system

In [Chapter 4](#) we described trapping and manipulation of single atoms in optical tweezers. We demonstrated preparation in defined quantum states and cooling close to the motional ground state. Building on these results, we now use Rydberg states to induce interactions between single atoms, the key ingredient for quantum simulation. The long-range character of Rydberg atoms can induce interactions over several micrometers, exactly the length scale of the atom-to-atom distance in optical tweezers.

First the laser system for direct excitation to Rydberg states is introduced, starting from the seed laser in the infrared (IR) ([Section 5.1](#)) and the lock to a stable reference ([Section 5.2](#)). The key parts of this system are two cavity-enhanced frequency doubling stages to create light in the ultraviolet (UV) regime. We explain how the cavities were calculated and designed in [Section 5.3](#). In [Section 5.4](#) the optical setup for the ultra-violet light is described.

For the first experimental measurements with Rydberg atoms, presented in [Section 5.5](#), we look at a spectroscopy of Rydberg transitions, which were also the first signals of a working UV laser we observed in the laboratory.

#### 5.1 Seed laser

The first part of the UV laser system is the seed laser in the infrared, which is then amplified with a Raman fibre amplifier and frequency doubled twice to generate ultraviolet light. Hence the performance of this seed laser in terms of linewidth, long-term stability and phase noise is crucial, as it determines those parameters in the UV. Furthermore, the seed laser needs to be tunable in wavelength to address all Rydberg states from  $n \approx 20$  up to the ionisation threshold, corresponding to wavelengths of 285.5 nm to 288.5 nm in the UV and therefore 1142 nm to 1154 nm in the IR.

We use a home-built ECDL with an interference filter, but an improved design compared to the diode lasers introduced so far in this thesis. For the latter, we have observed a strong sensitivity to ambient noise or pressure changes when locking to high finesse optical cavities, e.g. from opening the door of the lab. Given the strong requirements for the seed laser as explained above, we have improved the design as follows: We use a monolithic and air-tight design to prevent or attenuate the impact of pressure changes and acoustic noise, as shown in [Fig. 5.1](#). Furthermore, we use a relatively long cavity of 70 mm to reduce phase noise [[133–135](#)].

The whole laser setup is mounted on a breadboard, which is isolated with Sobothane feet

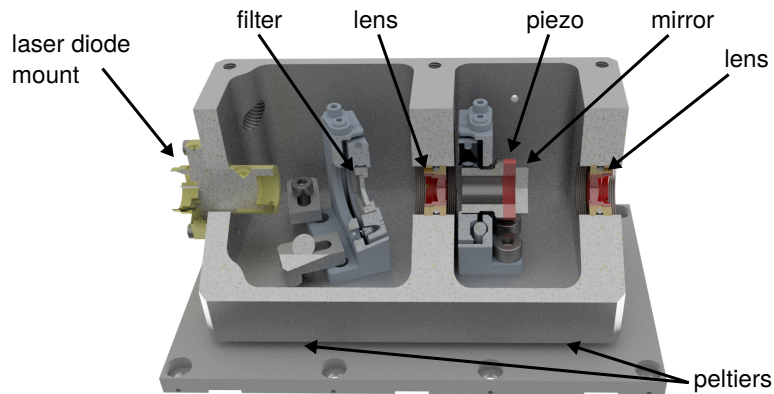


**Fig. 5.1** CAD model of the monolithic linear laser. The filter mount can be rotated to allow coarse wavelength adjustment by turning the filter. Laser diode and kinematic mounts are commercial parts, only the narrow-band filter ( $\delta_{\text{transmission}} \approx 0.5 \text{ nm}$ ) and partially reflective mirror ( $R = 30\%$ ) are custom-made. The aluminium lid with a rubber gasket as well as a plastic housing around the laser are not shown.

from the optical table and enclosed in a wooden box to further attenuate acoustic noise and thermal drifts.

## 5.2 Reference cavity

To provide a precise and long-term stable reference for both the UV seed at 1144 nm and the Raman laser at 770 nm, we use an optical cavity made of ultra low expansion glass (ULE). The cavity itself is 10 cm long with a round spacer and has a finesse of  $\mathcal{F} \approx 10\,000$  for the wavelengths used<sup>1</sup>. The cavity is mounted inside a vacuum housing, as shown in Fig. 5.2. The design of the housing with two inner copper shields is inspired by reference [133]. An outer vacuum housing with a large heat capacity acts as a thermal lowpass filter, attenuating thermal fluctuations.

A peltier element is used to thermally stabilise the outer copper box. Assuming perfect stability at the point of the thermistor, a change of the temperature of the vacuum chamber will cause a temperature gradient from the bottom where the thermistor sits to the top of the copper box, which is furthest away from the thermistor. The temperature at the top of the copper shield varies with the temperature of the outer housing on the order of 10 mK/K [133]. The outer copper shield thus attenuates thermal fluctuations by two orders of magnitude. A second copper shield further increases this suppression of thermal fluctuations. The second box is thermally only connected at a single point, close to the thermistor. Since the inner shield only sees the relatively small temperature gradient of the outer box, this dual shield construction allows to provide a very stable temperature for the ULE cavity. Note that without a defined thermal contact of inner and outer shield, the

<sup>1</sup>Advanced thin films. The finesse was calculated from measurements of the manufacturer.

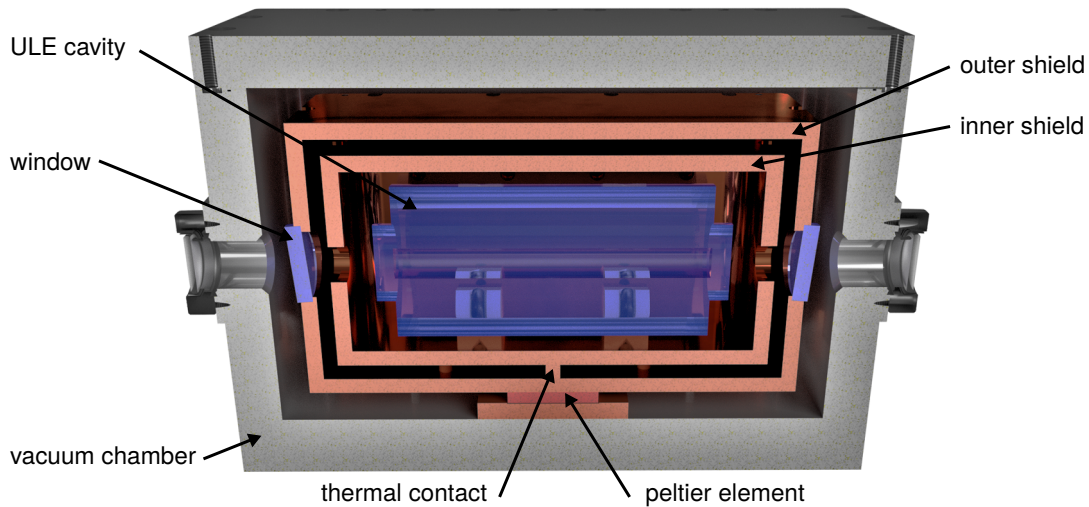


**Fig. 5.2** Cut of a CAD drawing of the ULE cavity housing with the outer vacuum chamber and the two inner copper shields. Two anti-reflection coated windows on the outer shield further reduce thermal radiative coupling to the outside. The ion pump, valve and electrical feed-through are not shown.

inner shield would just follow the average temperature of the outer shield without further attenuation of thermal changes. We do not use active dual stage temperature stabilisation for both copper shields, since two coupled stabilisation loops can cause instabilities. The whole assembly is mounted in a wooden enclosure for additional thermal and acoustic shielding.

To lock the seed laser to the cavity resonance we use the Pound Drever Hall (PDH) locking scheme [136]. A fibre EOM<sup>2</sup> is used to frequency modulate the laser light and create sidebands at 21.3 MHz. In order to tune the laser frequency in between the free spectral range between two cavity modes, we additionally modulate the light with the EOM with a frequency of 50 and 700 MHz, called the large side bands<sup>3</sup> [137]. The laser is not locked to the carrier but to one of the large side bands which is on resonance with the cavity mode, shown in Fig. 5.3. Since the laser frequency is doubled twice, this allows for a continuous frequency tuning range of 2.5 GHz in the UV. The light sent to the ULE cavity is intensity stabilised with an AOM to prevent amplitude noise to frequency noise conversion, which can be caused for example by imperfect alignment of the polarisation with respect to the EOM axes [133]. This conversion can shift the zero-crossing of the error signal.

ULE glass has an extremely low coefficient of thermal expansion with a zero crossing for a fixed temperature. If the spacer is kept at this zero expansion temperature  $T_c$ , the sensitivity to thermal changes is maximally suppressed. To determine the temperature  $T_c$ , we

<sup>2</sup>EOspace 10 Gb/s Lithium Niobate Phase Modulator at 1140-1160 nm - PM-0S5-10-PFA-PFA-1140/1160

<sup>3</sup>Electronic parts used for the EOM modulation and PDH lock (see Fig. 5.3):

DDS branch: trafo: FTB-1-1+, amplifier: ZFL-500HLN, doubler: MK-2, lowpass: SLP-800, amplifier: ZFL-1000H, combiner: ZFSC-2-2-S. Generator: Rigol DG1032.

Photodiode path: lowpass: SLP-50, amplifier: ZFL-1000LN, mixer: ZFM-3-S, lowpass: BLP-2.5

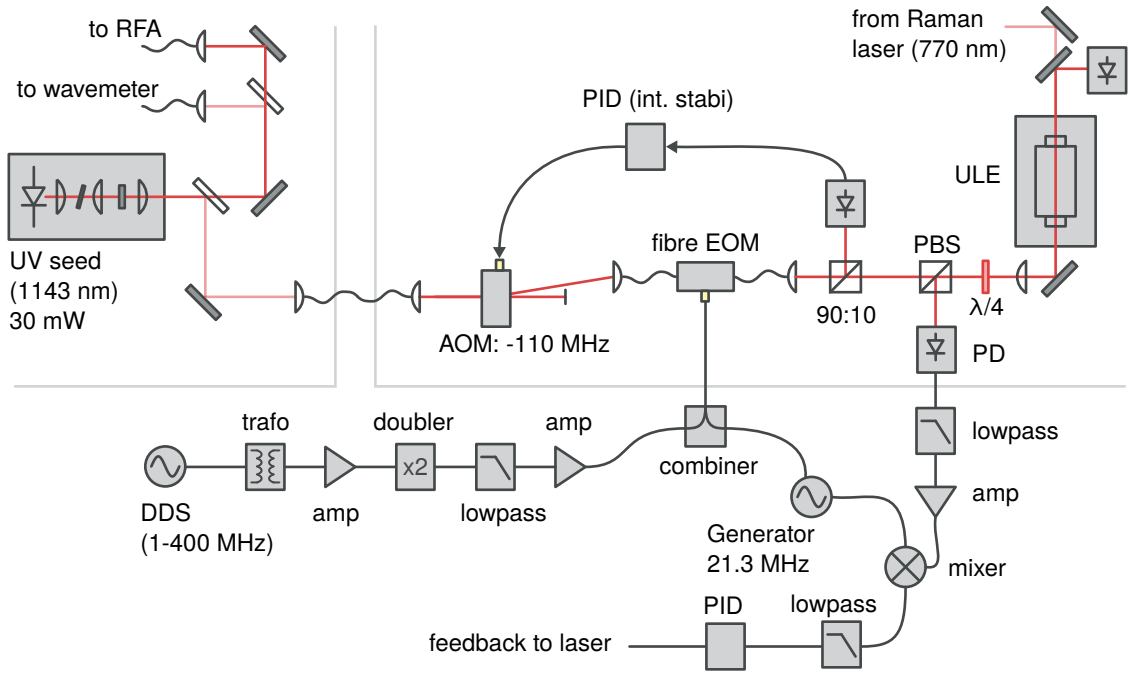


**Fig. 5.3** Optical and electrical setup of the UV seed and ULE lock: The laser is modulated with a fibre EOM at a variable frequency of 50 to 700 MHz. One of the side bands is then locked onto the ULE cavity. For the Pound Drever Hall locking scheme additional side bands at 21.3 MHz are used. The reflected light from the cavity is sent to a photo diode. The signal is lowpass filtered to remove signals arising from higher sidebands and demodulated to generate an error signal, which feeds back to the laser. The light sent to the cavity is intensity stabilised using an AOM.

measure the change of a cavity resonance for several temperatures as follows: We lock the Raman laser at 770 nm to the cavity and measure the beat note to a second laser at the same wavelength, which is stabilised to a second ULE cavity in another laboratory [138]. We allow the cavity to settle for 24 hours after each temperature change. For a linear change of the expansion coefficient we expect a quadratic change of the length and thus resonance frequency. This quadratic change is observed in our measurements, as shown in Fig. 5.4, and the beat frequency as a function of temperature is described by

$$f_{\text{beat}} = (0.28 \pm 0.01)\text{MHz}/\text{K}^2 \cdot (T - (23.28 \pm 0.08)^\circ\text{C})^2 + (72.1 \pm 0.1)\text{MHz}$$

with the errors from the quadratic fit. We estimate a thermal sensitivity of 56 Hz/mK in a temperature range of 100 mK around the zero expansion temperature  $T_c$ . This is ideal for experiments with Rydberg atoms which have typical linewidth of the transitions on the order of kHz. With the beat of a second stable laser, we have a fixed frequency reference, allowing us to determine the exact free spectral range of the cavity. We lock the laser to two neighbouring  $\text{TEM}_{00}$  modes and measure a difference in the beat note of 1497.561 MHz, as expected for a 10 cm long spacer.

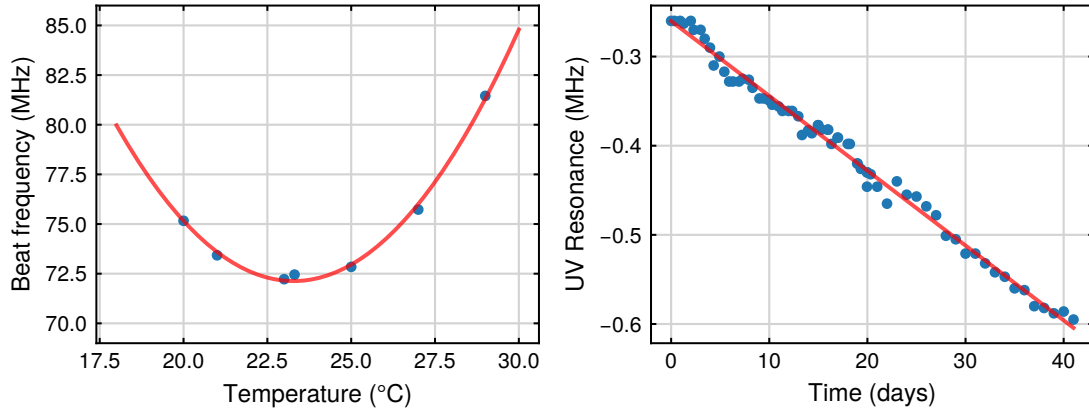


**Fig. 5.4 Left:** Measurement of the zero expansion temperature of the ULE cavity: Beat measurement between the Raman laser, which is locked to the ULE cavity and a second stable laser for different temperatures. The red line is a quadratic fit, showing a zero expansion temperature of  $T_c = 23.28$  C. **Right:** Measured resonance of the  $4S_{1/2} F = 2, m_F = +2$  to  $62P_{1/2} m_J = -1/2$  transition over more than one month. The linear fit shows a drift of 8.4 kHz/day.

To determine the long term drift we measure and record the frequency change of the  $4S_{1/2} F = 2, m_F = 2$  to  $62P_{1/2} m_J = -1/2$  transition on a daily basis for over one month, as shown in Fig. 5.4. This linear drift of  $8.4 \pm 0.1$  kHz/day ( $97 \pm 1$  mHz/s) in the UV corresponds to 4 times the drift of the seed laser. The linear drift is on the order of magnitude that is expected from the aging of the ULE spacer [133].

## 5.3 From the IR to the UV

In the following section, we introduce how light in the UV can be created from the seed light in the infrared with two consecutive doubling stages. The key points of the theory of second harmonic generation are explained, focussing on relevant parameters for this work. A detailed description and calculation for the setup used can be found in the thesis of Anne-Sophie Walter [139].

### 5.3.1 Theory of frequency doubling

For the general theory of non-linear optics and second harmonic generation we refer to the literature [140]. In the following the steps for calculation and design of the two cavity enhanced second harmonic generation stages are explained.

#### Phase matching

In a first part we look at the so-called phase matching which is a criterion for efficient frequency doubling in a non-linear medium: For efficient frequency doubling in non-linear

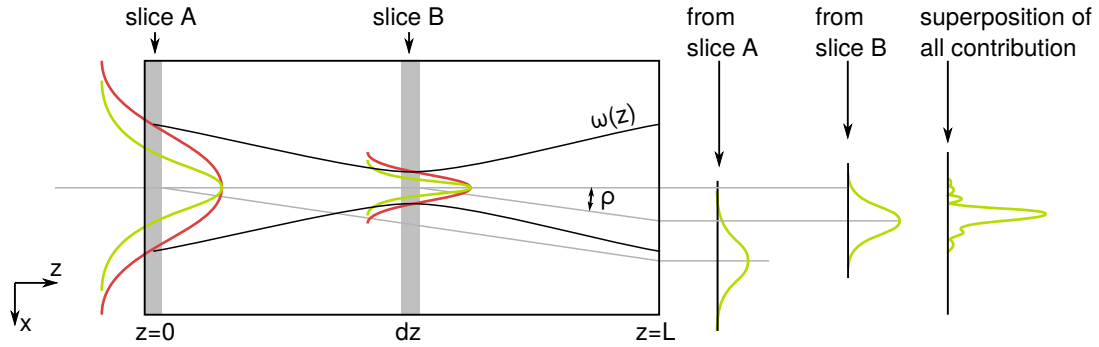


**Fig. 5.5** Second harmonic generation in a crystal of length  $L$  with a focussed Gaussian beam with waist  $\omega$ . The waist of the fundamental is shown in red, the created second harmonic in green. For illustration the effects for two slices A and B in the crystal are shown. The focussing leads to varying intensities and thus varying second harmonic conversion efficiencies over the length of the crystal. The generated second harmonic propagates with the walk-off angle  $\rho$  with respect to the fundamental, causing a non-Gaussian beam profile when adding the contributions of all slices. Maximising the Boyd Kleinman factor  $h$  yields optimal beam parameters for best single pass frequency doubling.

crystals, the refractive indices of the medium for the fundamental and second harmonic light have to be matched [140]. We assume a plane wave with frequency  $\omega$ . This wave creates a second harmonic with a frequency  $2\omega$  in a non-linear medium with finite length  $L$ . The intensity of the second harmonic is determined by the difference wave vector  $\Delta k$  of both beams as  $I_{2\omega} \propto I_{\omega}^2 \cdot L^2 \cdot (\text{sinc}(\Delta k L / 2))^2$ . Only if the refractive indices are matched, such that  $n(\omega) = n(2\omega) \Rightarrow \Delta k = 0$ , the harmonic light created at different positions inside the medium will interfere constructively. This condition is called phase matching. In the following the so-called 'type I' phase matching is considered, where the fundamental photons have the same polarisation and the second harmonic has a perpendicular polarisation. In addition we can distinguish between critical and non-critical phase matching. For non-critical phase matching, the polarisation is aligned along one axis of a birefringent non-linear crystal and the refractive indices are matched by changing the temperature of the crystal. This method is used for the first SHG stage in our setup, but is generally limited by the choice of crystals and feasible temperature ranges. For critical phase matching, the birefringent medium is rotated to find a position on the refractive index ellipsoid such that  $n(\omega) = n(2\omega)$  is satisfied. This is used for the second SHG stage.

### Boyd Kleinman equation

In contrast to the plane wave assumed above, a Gaussian beam is a better approximation of a laser beam. This is especially true since the beam will be strongly focussed inside the non-linear medium to achieve a high intensity which is needed for efficient second harmonic generation. A small focus yields high intensities, but a short Rayleigh range, causing a non-uniform intensity over the length of the crystal and thus a non-uniform conversion

efficiency. In addition the second harmonic light that is created will not propagate in the same direction as the fundamental, but instead in the direction given by the walk-off angle  $\rho$ , which depends on the crystal. The effects of focussing and walk-off are illustrated in Fig. 5.5. To determine the optimal beam parameters for second harmonic generation, we use the theory of Boyd and Kleinman, described in the following [141]: The power of the second harmonic light  $P_{SH}$  as a function of fundamental power  $P_F$  can be expressed as

$$P_{SH} = \underbrace{\frac{16\pi^2 L d_{\text{eff}}^2}{\epsilon_0 c \lambda_F^3 n_{SH} n_F}}_{\kappa} \cdot e^{-\alpha L} \cdot h(\sigma, B, \xi) \cdot P_F^2 = \kappa \cdot h(\sigma, B, \xi) \cdot P_F^2. \quad (5.1)$$

Here  $\kappa$  is a factor that depends on the non-linear coefficient  $d_{\text{eff}}$ , the length  $L$  of the crystal, the wavelength  $\lambda$  and refractive index  $n$  and absorption coefficient  $\alpha$ . The indices  $F$  and  $SH$  indicate properties of the fundamental or second harmonic.  $h$  is the Boyd-Kleinman factor, given by

$$h(\sigma, B, \xi) = \frac{1}{4\xi} \int_{-\xi}^{\xi} \int_{-\xi}^{\xi} \frac{e^{-i\sigma(\tau'-\tau) - B^2(\tau'-\tau)^2/\xi}}{(1+i\tau')(1-i\tau)} d\tau d\tau' \quad (5.2)$$

and depends on three parameters  $\sigma$ ,  $\xi$  and  $B$ .  $\sigma$  depends on the wave vectors of the beams as  $\sigma = \Delta k z_0/4$  with  $\Delta k = k_{SH} - 2k_F$ . The focussing of the beam in the medium is described by  $\xi = L/(2z_0)$  with the Rayleigh range  $z_0 = \pi\omega^2/\lambda$  with the waist  $\omega_0$ . The walk-off of the second harmonic is described by  $B = \rho\sqrt{Lk_F}/2$  with walk-off angle  $\rho$ , which depends only on crystal parameters and is fixed by the choice of the crystal. Optimising the Boyd-Kleinman factor  $h$  for  $\sigma$  and  $\xi$  yields the optimal beam parameters for second harmonic generation.

A particular crystal has to be chosen for both frequency doubling stages. For the first SHG stage, going from the infra-red to the green, we use lithium triborate (LBO). LBO has the advantage that non-critical phase matching for the desired wavelength range is possible for temperatures of 70 °C. Since both fundamental and second harmonic are polarised along the crystal axes, the walk-off angle  $\rho$  is small and vanishes for perfect matching. This enables us to use a long crystal, resulting in a high single pass conversion efficiency and good beam quality of the second harmonic. A good beam profile is especially important since the green light needs to be coupled into a second cavity.

For the generation of UV light beta barium borate (BBO) or cesium lithium borate (CLBO) are commonly used materials. Both differ in walk-off and non-linear coefficient. Even though BBO appears to be the better choice due to the higher conversion  $\kappa \cdot h$ , we chose CLBO for the following reasons: Due to the larger walk-off of BBO the spatial mode of the second harmonic is non-Gaussian leading to significant losses in the optical setup since only the gaussian contribution of the mode can be used. The smaller walkoff angle of CLBO leads to a better beam profile. Additionally the damage threshold of CLBO is higher. BBO was reported to irreversibly degrade at high optical UV powers [142–145].

For each SHG stage we furthermore need to decide if a plane crystal with anti-reflection coating or a Brewster cut crystal should be used. A Brewster cut allows for very low reflec-

	LBO	CLBO	BBO
Wavelength	1150 $\rightarrow$ 575	575 $\rightarrow$ 287	575 $\rightarrow$ 287
Refractive index ( $n(\omega) = n(2\omega)$ )	1.603	1.495	1.67
Walk-off angle $\rho$ (mrad)	0.39	36.4	83.6
Effective non-linearity $d_{\text{eff}}$ (pm/V)	0.84	0.71	1.84
Angle with optical axis $\theta$	90	54.3	42.9
Angle with second optical axis $\phi$	0	uniaxial	uniaxial
Crystal length (mm)	20	10	10
Temperature ( $^{\circ}\text{C}$ )	70	125	$\approx$ 80
optimised waist / used waist ( $\mu\text{m}$ )	29 / 50	21 / 36	20 / 34
optimised $h$ / used $h$	1.06 / 0.72	0.095 / 0.074	0.040 / 0.031
$\kappa$ ( $10^{-4}/\text{W}$ )	2.15	7.06	38.0

**Tab. 5.1** Parameters for the crystals lithium triborate (LBO), cesium lithium borate (CLBO) and beta barium borate (BBO), that can be used. Both optimal parameters for  $\xi = \xi_{\text{opt}}$  and parameters used in the setup for a doubled waist inside the crystal ( $\xi = \xi_{\text{opt}}/3$ ) are shown. BBO is shown in grey for comparison but was not used. All crystal parameters were calculated with the AS-photonics SLNO software [147].

tion losses of the fundamental, while anti-reflection coatings have small but finite losses. Due to the lower losses the Brewster cut results in higher intra-cavity power and higher conversion efficiency. However, since the polarisation of second harmonic is orthogonal to the fundamental, about 20% ( $n = 1.6$ ) of the second harmonic will be reflected at the surface of the crystal. An anti-reflection coated crystal will introduce a small loss of the fundamental which reduces the intra-cavity power, leading to lower conversion efficiency, but transmit the second harmonic with low losses. Both effects lead to comparable effective doubling efficiencies in our case.

For the LBO crystal we use an anti-reflection coating, since in the infra-red regime low-loss coatings are available. In contrast to a Brewster cut, for a plano crystal the beam is not projected onto an elliptical one when entering the crystal, leading to a symmetric gaussian beam profile of the second harmonic. Parameters for the discussed crystals are shown in Table 5.1.

For the second cavity we chose a Brewster cut crystal, to prevent damage or degradation to the coating [145, 146]. See also Section 5.4 for damage and degradation of optical components due to UV light.

The optimal waist from the Boyd-Kleinman theory is valid for single pass conversion. A larger waist reduces degradation, damage to the crystal and thermal lensing, but results in a lower conversion factor. If enhancement cavities are used, lower conversion of the fundamental will increase the finesse and intra-cavity power, partially compensating for the lower single-pass conversion. We thus reduce  $\xi$  by a factor of 3 compared to the optimised value, which roughly doubles the waist  $\omega_0$ . This only reduces the Boyd-Kleinman factor by  $\approx 25\%$ .

The discussed optimisation fixes the length of the crystal  $L$  and the waist inside the crystal

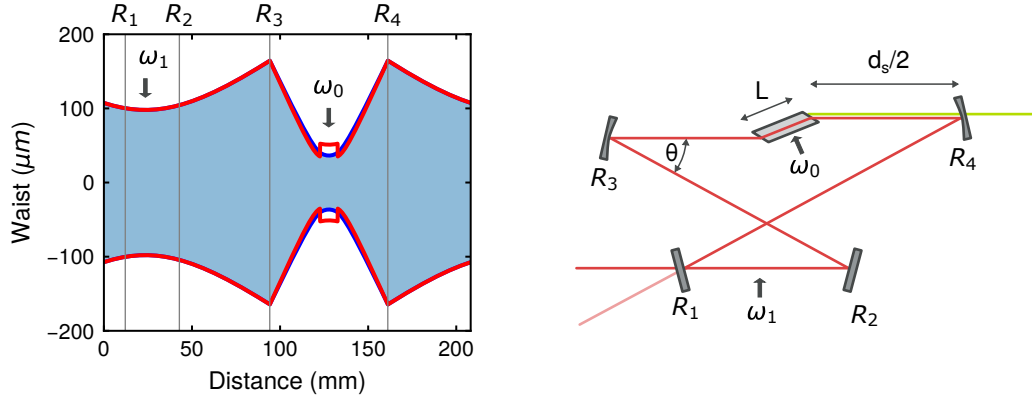


**Fig. 5.6** Beam profile and geometry of the second cavity. **Left:** Beam waist for sagittal (blue) and tangential (red) plane inside the cavity, calculated using the ABCD matrix formalism. The discontinuity of the tangential waist at the crystal position is due to the brewster cut crystal, which projects a circular onto an elliptical beam. The opening angle is chosen such that the second waists  $\omega_1$  are equal in both sagittal and tangential plane. Positions of mirrors and the two waists are marked. **Right:** Geometry of the cavity (to scale). The short arm length  $d_s$  is defined as the distance from  $R_3$  to  $R_4$  without the length of the crystal  $L$ . The long arm  $d_l$  is the distance  $R_4 - R_1 - R_2 - R_3$ .

	LBO (plane)	CLBO (brewster)
Radius of curvature $R$ (mm)	75	50
Short arm $d_s$ (mm)	75.8	57
Long arm $d_s$ (mm)	287.6	141.3
Opening angle $\theta$ (degrees)	15	28.6

**Tab. 5.2** Geometries of both doubling cavities, calculated with the ABCD matrix formalism.

$\omega_0$ . The single pass conversion efficiency as a function of fundamental power is known.

### Cavity geometry

After having decided which crystals to use, the next step is the design of the enhancement cavity, depicted in Fig. 5.6. The parameters for the curvature of the mirrors  $R_3$  and  $R_4$ , the length of the short and long cavity arms  $d_s$  and  $d_l$  and the opening angle  $\theta$  need to be optimised. Using the ABCD matrix formalism, each optical element can be described by a 2 by 2 matrix. For example, a free propagation  $M_d$  over a distance  $d$  or a reflection at a spherical surface  $M_R$  with radius  $R$  are given by

$$M_d = \begin{pmatrix} 1 & d \\ 0 & 1 \end{pmatrix} \quad \text{and} \quad M_R = \begin{pmatrix} 1 & 0 \\ -2/R & 1 \end{pmatrix}. \quad (5.3)$$

A Gaussian beam is described by the complex parameter  $q$  and the propagation of the beam with waist  $\omega$ , curvature of the wave front  $r$ , wavelength  $\lambda$  and refractive index  $n$  of

the medium is described by

$$q_{\text{final}} = \frac{Aq_{\text{initial}} + B}{Cq_{\text{initial}} + D} \quad \text{with:} \quad \frac{1}{q} = \frac{1}{r} - \frac{i\lambda}{\pi n\omega^2} \quad \text{for a matrix} \quad M = \begin{pmatrix} A & B \\ C & D \end{pmatrix}. \quad (5.4)$$

This allows us to describe the beam inside the cavity by multiplying the matrices of all optical elements. The waist inside the crystal is fixed to the before-optimised value. The waists inside the cavity and the chosen geometry are shown in Fig. 5.6.

The first criterion is the stability of the cavity. After one round trip the initial and final waist have to be the same, otherwise the beam would diverge after multiple round trips. This condition is given by  $q_f = q_i = q$  in Eq. (5.4). Any set of distances  $d_l$  and  $d_s$  and curvature of mirrors that fulfil this requirement form a stable cavity. The values chosen are shown in Table 5.2. An additional constraint is that the radius of curvature is not a continuous parameter but fixed by available substrates.

So far only the length of the cavity arms are fixed, but not the opening angle  $\theta$ . If an optical element such as a curved mirror has a finite angle of incidence  $\theta$ , this will induce astigmatism, causing different waists in the sagittal and tangential plane. This is described by replacing  $R \rightarrow R \cdot \cos(\theta)$  for the tangential and  $R \rightarrow R/\cos(\theta)$  for the sagittal plane in the matrix  $M_R$ . A Brewster cut crystal also causes astigmatism. The astigmatism of mirrors and Brewster cut crystal can compensate each other for a given angle  $\theta$  to ensure a round beam in the second waist between mirrors  $R_1$  and  $R_2$ . This simplifies incoupling of light into the cavity, which otherwise would need to be shaped elliptically.

For a plane crystal the astigmatism of the curved mirrors cannot be compensated, such that a small opening angle is favourable, minimising the astigmatism. This is only limited by mechanical constraints such as the size of mirror mounts. It is possible to use convex mirrors for  $R_1$  and  $R_2$  instead of plane mirrors, allowing one to compensate astigmatism [148]. However, this was not implemented as additional curved mirrors can induce further aberrations, increasing the sensitivity of the cavity to alignment errors.

### Impedance matching

The last parameter that needs to be optimised is the reflectivity of the incoupling mirror  $R_1$  of the cavity, called impedance matching. Optimal coupling of light into the cavity is only achieved, if the reflected electric field at  $R_1$  and the light leaking out of the cavity (transmission through  $R_1$  from inside the cavity) interfere destructively. Otherwise light incident to the cavity will be reflected. The circulating power  $P_{\text{circ}}$  inside the cavity is given by

$$\frac{P_{\text{circ}}}{P_{\text{inc}}} = \frac{1 - R_1}{\left(1 - \sqrt{R_1 R_{234}}(1 - \kappa P_{\text{circ}})\right)^2} \quad (5.5)$$

with the reflectivity of all mirrors  $R_{234} = R_2 \cdot R_3 \cdot R_4$  and the incoupled power  $P_{\text{inc}}$ . Given an input power  $P_{\text{inc}}$  and all losses from the mirrors or anti-reflection coating of the crystal,

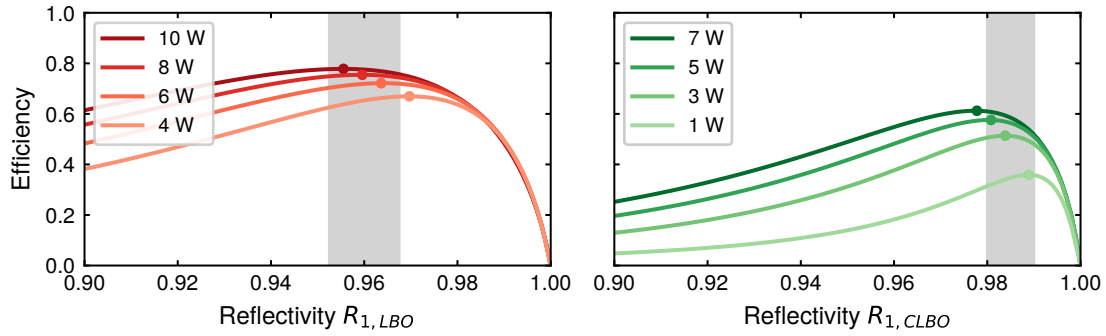


**Fig. 5.7** Doubling efficiency as a function of the reflectivity of the incoupling mirror  $R_1$  for several powers  $P_{\text{inc}}$  for the first (**left**) and second (**right**) doubling cavity. The optimal reflectivity for each power is marked. The chosen reflectivity including tolerances from the manufacturers is marked in grey.

the optimal reflectivity  $R_1$  can be calculated. For higher powers  $P_{\text{inc}}$  a lower reflectivity  $R_1$  is optimal. The circulating power  $P_{\text{circ}}$  and the doubling efficiency show a steep fall-off for high reflectivities ( $R_1 = 1 \Rightarrow P_{\text{circ}} = 0$ ), thus for this calculation the available optical power should not be underestimated [139]. The doubling efficiencies for both cavities in function of the reflectivity of the incoupling mirror  $R_1$  are shown in Fig. 5.7. The mirrors used have reflectivities of  $R_{1,LBO} = 96 \pm 0.75\%$  and  $R_{1,CLBO} = 98.5 \pm 0.5\%$ , where the error is the uncertainty from the manufacturing process. All other mirrors are  $R_{234,LBO} = (99.99\%)^3$  and  $R_{234,CLBO} = (99.95\%)^3$  for the fundamental wavelength and transmissive for the second harmonic.

This last step fixes all geometrical dimensions for the cavity such as the length of the arms  $d_s$  and  $d_l$ , the opening angle  $\theta$  and the reflectivity of the incoupling mirror  $R_1$ .

### 5.3.2 Experimental setup and SHG stages

We now look at the design and implementation of the two frequency doubling stages, using the optimised geometries and parameters. Both stages are identical in design and only the dimensions are adjusted to fit the different cavity geometries.

The first doubling stage is shown in Fig. 5.8. It is designed with an outer airtight chamber, which can be evacuated. This allows for stable operation, reduces acoustic noise and makes flooding with gases like argon or oxygen possible. Oxygen was reported to prevent degradation of crystals or contaminations of cavity mirrors [149, 150]. A 4 cm thick aluminium board is fixed with magnetic seats<sup>4</sup> inside the chamber. All mirrors and the crystal mount are fixed on this board, preventing mechanical stress and misalignment of the cavity if the outer chamber is evacuated.

The crystal is placed inside a copper mount and fixed with indium foil to increase heat contact and reduce mechanical stress onto the fragile crystal. The mount is heated and temperature stabilised using an electric heater and thermistor. The crystal mount is ther-

<sup>4</sup>Thorlabs KBS98

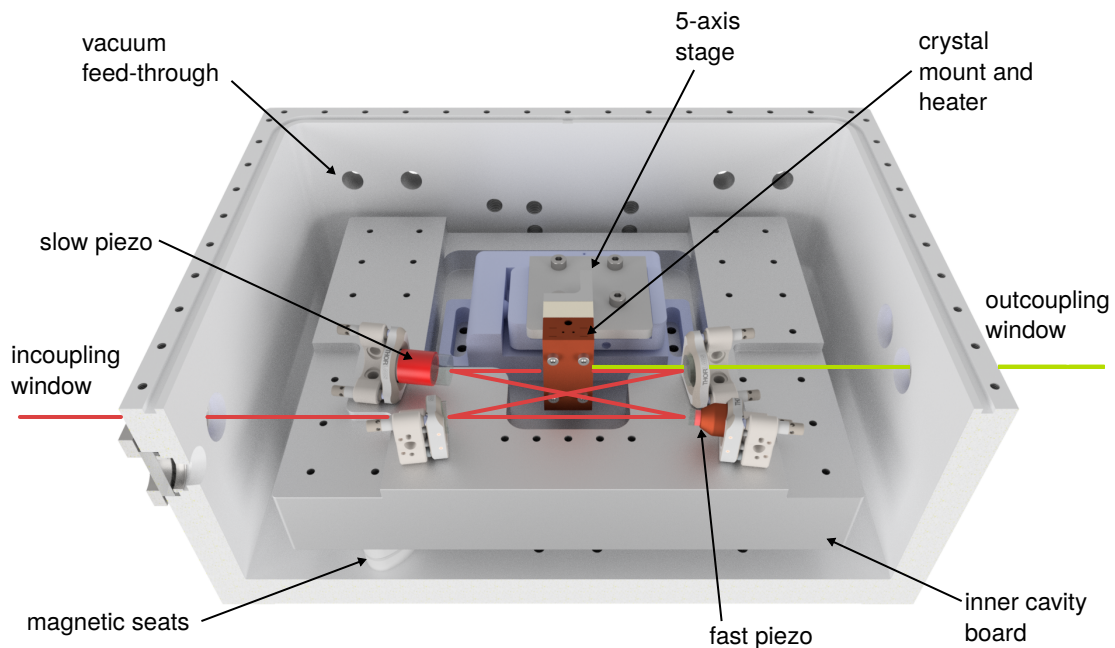


**Fig. 5.8** Rendered picture of the first frequency doubling stage with a 2 cm long AR-coated LBO crystal. The outer housing is air tight and all windows and electric feed-throughs are sealed with viton rings. The inner cavity board is decoupled from mechanical stress with magnetic seats. The mirror mounts are aligned with precision pins to the optimised cavity geometry. The lid is not shown.

mally isolated from a five axis alignment stage with a spacer made of Vespel, a thermally stable and low out-gassing plastic.

All mirrors<sup>5</sup> are mounted using stainless steel mirror mounts. To adjust the length of the cavity and lock a cavity resonance to the laser frequency, we use two piezo elements. One long piezo allows for a large range of motion of several micrometers using low voltages. Several free spectral ranges of the cavity can be scanned and long term drifts can be compensated. A second small piezo is used for fast stabilisation of the cavity length. Both fast piezo and mirror are 6 mm in diameter and 2 mm thick to minimise weight, increasing the feedback bandwidth. The piezo is mounted onto a conical copper part that is filled with lead to dampen mechanical resonances. This allows for a high bandwidth of the cavity lock of 50 kHz [151].

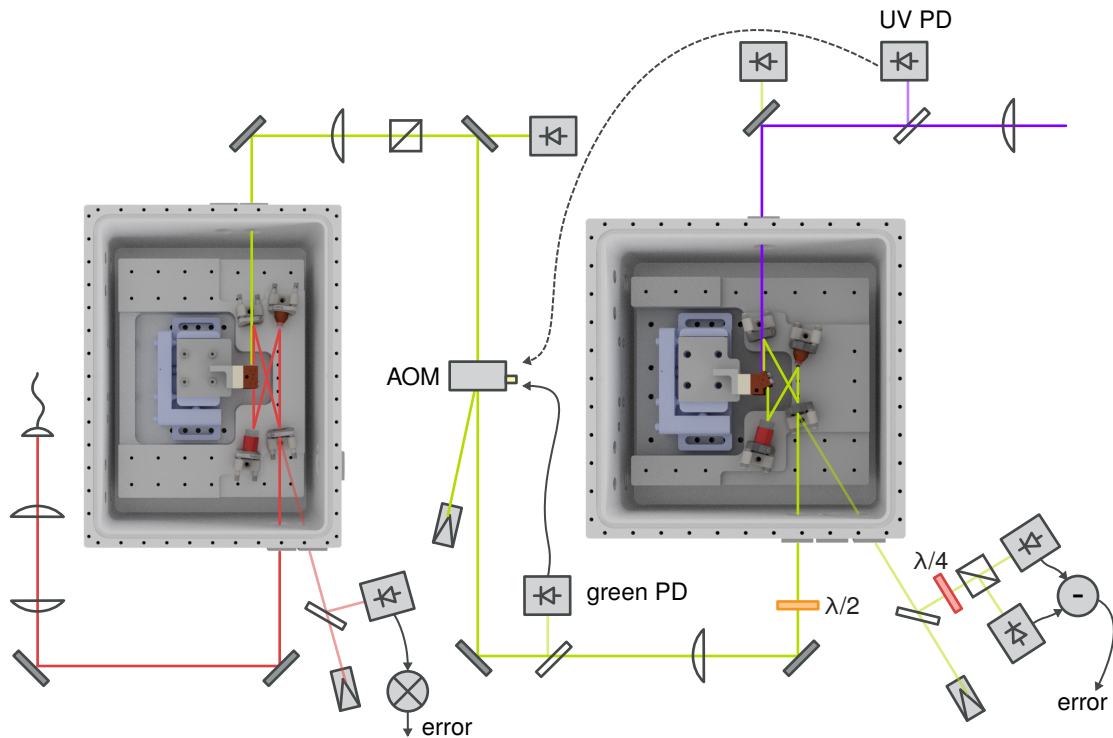


**Fig. 5.9** Setup of both resonant frequency doubling stages. The first cavity is stabilised with a Pound-Drever-Hall lock, the second one with a Hänsch-Couillaud scheme. An AOM allows for intensity stabilisation of either the green light or directly of the UV light.

### Frequency locking of the cavities

Two different techniques are used to generate an error signal for locking the cavities. The first cavity is locked using a Pound-Drever-Hall lock [136]. Side bands of 60 MHz are generated using a resonant EOM before the fibre amplifier of the seed laser. The error signal is generated by demodulating the cavity reflection signal with the same frequency used to drive the EOM.

As shown in Fig. 5.9, we use an AOM for intensity stabilisation. For most experiments the green light is intensity stabilised, but the UV power can also be stabilised directly. Stabilising the UV directly with the AOM in the green can cause crosstalk to the lock of the second cavity. Depending on the application, the most suitable stabilisation method is used.

For the second cavity we use a Hänsch-Couillaud lock [152]. This technique does not rely on side bands at a different frequency, but uses the fact that a polarising element, such

<sup>5</sup>If not stated otherwise, all mirrors are  $\varnothing = 12.7$  mm and 6.35 mm thick and coated on the front HR(1140-1154nm) >99.99% + HT(570-577nm)<97% [HR(570-578nm) > 99.95% + HT(285-289nm)>90%] and the backside AR(570-577nm)<0.5% + AR(1140-1154nm)<0.5% [AR(285-289nm)<1% + AR(570-578nm)<0.5%] for the first [second] cavity.

as a Brewster cut crystal, makes the transmission and reflection of the cavity polarisation dependent. The light before the cavity is linearly polarised but slightly rotated with respect to the cavity plane. The polarisation of the reflected light is detected by a quarter wave plate and a polariser with a differential photo diode, generating an error signal.

We chose this technique to ensure a negligible level of residual modulation in the UV light. In a PDH lock, modulation of the second harmonic can be caused by mixing of carrier and sideband in the non-linear medium. Avoiding this modulation by using the HC lock is especially important for off-resonant experiments such as Rydberg dressing, where residual modulation of the light can become resonant.

To generate a feedback signal for the piezo elements from the error signal, we use digital FPGA based<sup>6</sup> PID controllers [149, 153]. Each controller has two independent PID loops, used for the slow and fast piezo element.

The use of digital controllers, compared to commonly used analog circuits, offers the advantage of simple implementation of relock functionality: In addition to the error signal the intra-cavity power is used to determine whether the cavity is locked. If this power falls below a threshold, the controller disables the PID lock and starts scanning the slow piezo with increasing amplitude, starting at the last setting before the lock was lost. If it is close to resonance, the intra-cavity power exceeds the threshold and the PID lock is enabled again. For each experimental sequence, the second cavity is only locked 100 ms before the UV pulse and unlocked afterwards. At a cycle time of 1 Hz, this reduces degradation of the crystal and other optics by one order of magnitude. A digital locking solution allows easy implementation of software controlled lock-and-unlock into the experimental control. The first cavity is continuously locked. We observe stable operation of the whole UV system without need for manual intervention over weeks.

### 5.3.3 Characterisation

To characterise the performance of both cavities, we first measure the power of incoupled light  $P_{\text{inc}}$  and second harmonic light  $P_{\text{out}}$  and calculate the doubling efficiencies  $\eta = P_{\text{out}}/P_{\text{inc}}$ .

For the given reflectivities, losses and non-linear coefficients, the doubling efficiency  $\kappa$  can be calculated from Eq. (5.5), as shown in Fig. 5.10 for the second doubling stage.

For the first cavity we measure  $P_{\text{inc}} = 5.2$  W, including losses from the isolator after fibre amplifier and 80 % coupling to the Gaussian mode. With  $P_{\text{out}} = 3.3$  W of green light, the efficiency is  $\eta = 64$  %. The theoretical efficiency from Fig. 5.7 for this power is 70 %. Since not all imperfections are taken into account for the calculation, this shows a near optimal performance of the first doubling stage.

For the second cavity, the power in the UV light as a function of the input power is shown in Fig. 5.10. The efficiency for 1.8 W input power, including coupling efficiency to the Gaussian mode, is 33 %, lower than the calculated efficiency of 43 %. Assuming additional loss of 0.3 % in one cavity round trip, the theory from Eq. (5.5) fits well to the measured data,

<sup>6</sup>Red Pitaya STEMLab 125-14, firmware and interface from Fabian Schmid: <https://github.com/schmidf/rp-lockbox>

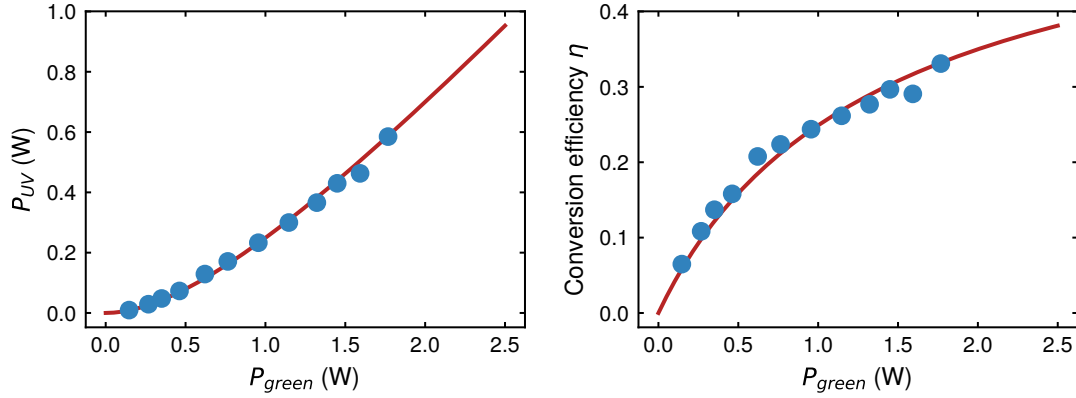


**Fig. 5.10** **Left:** Measurement of the second harmonic power in the UV  $P_{UV}$  depending on the incoupled power  $P_{green}$ . The incoupled power includes the coupling efficiency to the Gaussian mode. **Right:** Calculated conversion efficiency  $\eta$ . The theory from Eq. (5.5) with additional losses of 0.3% in one cavity round trip is shown in red.

	first cavity (LBO)	second cavity (CLBO)
Calculated FSR (MHz)	758	1405
Measured linewidth $\delta$ (MHz)	5.4	8.5
Measured finesse	141	165

**Tab. 5.3** Calculated free spectral range, measured linewidth and finesse for both cavities.

indicating additional losses inside the second cavity. Recently we achieved up to 800 mW output power in the UV, after improving the alignment and incoupling of the second cavity. To measure the finesse of the cavities, we scan the slow piezo and record transmission or reflection of the fundamental, error signal and second harmonic light for the first (Fig. 5.11) and second (Fig. 5.12) cavity. The free spectral range is calculated as  $FSR = c/L$  from the cavity length  $L$ , which is known with a good precision since the mirrors are aligned with reference to precision pins in the inner cavity board. We confirm this calibration for the first cavity with the sidebands of 60 MHz. We extract the linewidth of the cavities  $\delta$  as the full width at half maximum (FWHM) of Lorentzian fits to the transmission or reflection of the fundamental, shown for both cavities in Table 5.3. The second harmonic light is well fitted by a squared Lorentzian.

The Finesse  $\mathcal{F}$  of the cavity is given by the ratio of free spectral range and linewidth as  $\mathcal{F} = FSR/\delta$ . The finesse can also be related to the round trip losses  $R_{round}$  as  $\mathcal{F} = \pi \sqrt[4]{R_{round}} / (1 - \sqrt[2]{R_{round}})$ .

For the first cavity we calculate a finesse of  $\mathcal{F} = 82 \pm 8$ , where the error stems from the tolerance of the reflectivity of the first mirror. This is a factor two lower than the measured finesse of  $\mathcal{F} = 141$ , indicating either a higher reflectivity of the incoupling mirror or a reduced single pass conversion in the LBO crystal. Most likely is a reduced single pass conversion efficiency since the non-critical phase matching is temperature sensitive,

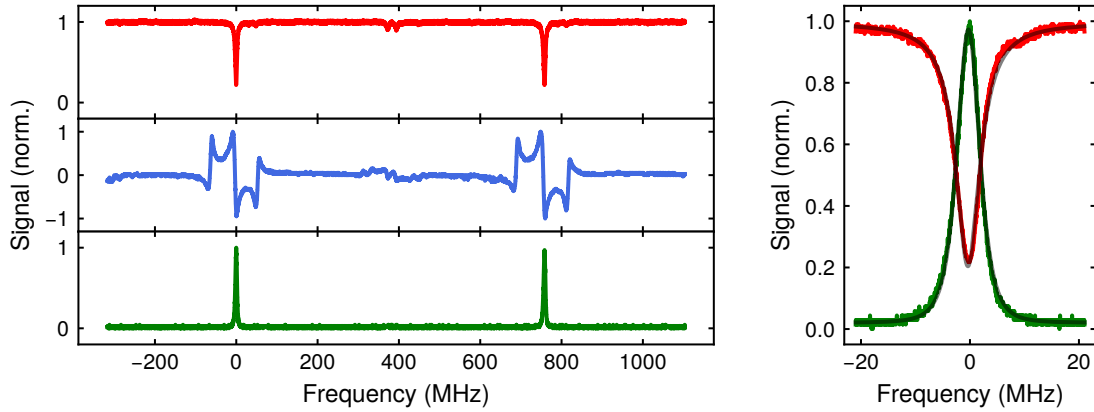


**Fig. 5.11** Characterisation of the first SHG cavity for the generation of green light. **Left:** Scan of the cavity length for the first cavity. Reflection (top), error signal for the PDH lock (middle) and second harmonic light (bottom) with the x axis calibrated to the free spectral range. **Right:** zoom of the reflection and second harmonic light. The reflection shows a Lorentzian linewidth of 5.4 MHz

increasing the walk-off factor and thus reducing the Boyd-Kleinmann factor for a non-ideal temperature of the crystal. However, the doubling efficiency would only be reduced slightly, since the higher circulating power can partially compensate a reduced single pass conversion.

For the second cavity we calculate a finesse of  $\mathcal{F} = 206 \pm 36$ , including the same additional losses of 0.3% as in Fig. 5.10. The error is calculated from the tolerances of the incoupling mirror. The measurement with  $\mathcal{F} = 165$  agrees with the theoretical calculations.

### 5.3.4 Linewidth and phase noise

The presented frequency doubling stages enable us to provide high power light in the UV, starting from a seed laser in the IR. As discussed in Section 5.1, this seed fixes the spectral properties like linewidth and phase noise. We now want to have a look on how those properties are affected in the two consecutive frequency doubling stages. A detailed analysis is given by Matveev et al. [133–135, 154] and only a short summary of relevant scalings is presented here.

If the frequency in the infrared is shifted, for example by changing the sideband frequency of the reference cavity lock, the frequency after a doubling stage will shift by twice the amount, as expected for frequency doubling.

However, the situation is different for phase noise of the laser. We assume the laser field to be  $E = E_0 \cdot \cos(\omega t + \phi(t))$  where  $\phi$  is the phase jitter with  $\langle \exp(i\phi(t)) \rangle_t = 0$ . We further assume that the residual phase noise is described by a normal distribution  $p(\phi) \propto \exp(-\phi^2/2\phi_{\text{rms}}^2)$ . The laser is approximated as a  $\delta$  function with no additional width, called the carrier.

The power in the carrier is then given by  $\eta = \exp(-\phi_{\text{rms}})$ . In the absence of noise ( $\phi_{\text{rms}} = 0$ ),

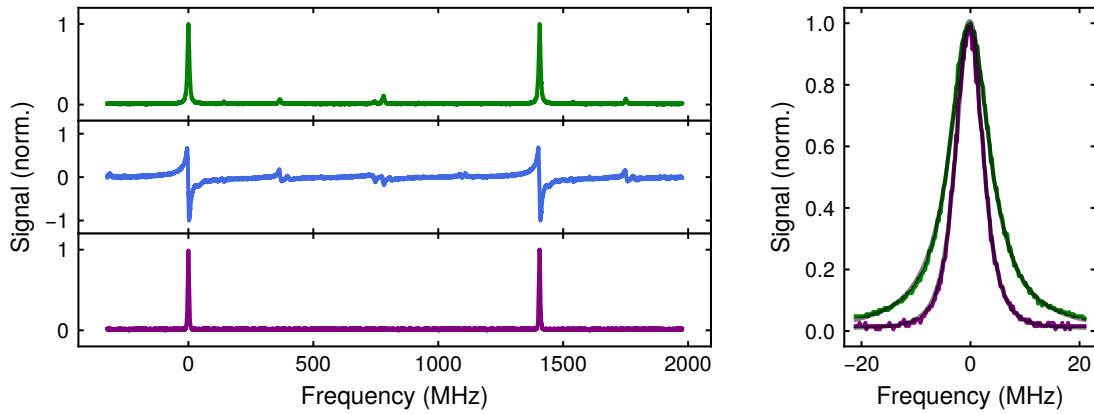


**Fig. 5.12** Characterisation of the second SHG cavity for the generation of UV light. **Left:** Scan of the cavity length for the second cavity. Intra-cavity power (top), error signal for the HC lock (middle) and second harmonic light (bottom) with the x axis calibrated to the free spectral range. **Right:** zoom of the intra-cavity power and second harmonic light. The cavity shows a Lorentzian linewidth of 8.5 MHz

all power is in the carrier ( $\eta = 1$ ). One can show that after frequency multiplication by a factor of  $n$  we get  $\eta' = \eta^{n^2}$ , in our case of two consecutive frequency doubling stages  $\eta' = \eta^{16}$ .

This unfavourable scaling is important, since phase noise can be a limitation in Rydberg experiments [111, 155]. This scaling of phase noise is also valid for multi-photon processes like the commonly used two-photon schemes for Rydberg excitation. Improving the phase noise of the seed laser, for example by replacing ECDLs with Titanium Sapphire lasers, which can have better spectral properties, or filtering the light using high finesse cavities, was shown to improve coherent Rydberg experiments significantly [56, 155].

We now turn to the width of the carrier, often just referred to as the linewidth of the laser. This scaling after frequency multiplication by  $n$  depends on the correlation time of the frequency fluctuations [135]. While for long correlation times, the width scales linearly in  $n$ , for short correlation times the linewidth scales as  $n^2$ .

The discussed scalings of phase noise and linewidth show the importance of low-noise lasers when using multi-photon processes [156].

## 5.4 Optical setup for the UV light

In this section the optical setup for the UV light is introduced. The setup is shown in Fig. 5.13. The diverging beam after the cavity is collimated and shaped using a set of spherical and cylindrical lenses. A single pass AOM is used for intensity control and fast pulses, using a low phase noise RF source<sup>7</sup>. The beam is focussed through a  $50 \mu\text{m}$  pinhole

<sup>7</sup>Rigol DSG815

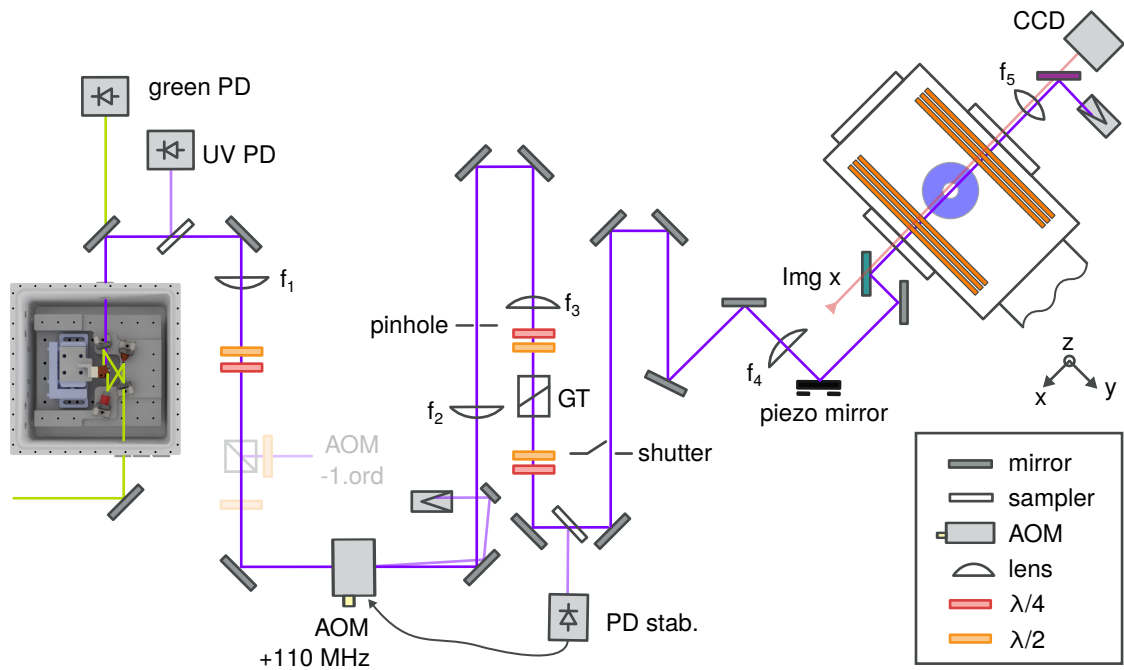


**Fig. 5.13** Optical setup in the UV. The diverging beam after the second cavity is collimated ( $f_1$ ). An AOM is used for intensity control and fast pulses. The beam is focussed ( $f_2$ ) onto a pinhole that is imaged in a 4-f-configuration ( $f_3$  and  $f_4$ ) onto the atoms. The polarisation at the atoms is circular, set by a Glan Taylor (GT) polariser and wave plates. For alignment the UV beam is overlapped with the x axis imaging beam (red line).

that is used as reference for alignment. The position of the pinhole is imaged in a 4-f-configuration onto the atoms with a waist at the atoms of  $20\ \mu\text{m}$ . The polarisation at the atoms is circular, adjusted with a Glan Taylor polariser and multiple wave plates. A piezo actuated mirror is used for precise alignment of the UV beam onto the atoms.

For short pulses with durations below  $20\ \mu\text{s}$ , the AOM in addition with a mechanical shutter after the pinhole is used for a sample-and-hold intensity stabilisation.

The setup is planned with the possibility of a second identical path, allowing for two UV beams. Using AOMs, a frequency difference in the range of 400 to 500 MHz for both beams can be realised, bridging the ground state splitting of  $^{39}\text{K}$ . This enables simultaneous Rydberg dressing of both ground states [44].

As shown in Fig. 5.13, both UV and imaging beam are overlapped using dichroic mirrors before the vacuum chamber. This enables alignment of the UV beam onto the optical tweezers by first loading a gray molasses and using a short resonant UV pulse before taking an absorption picture. The momentum kick from the UV light causes local atom loss, which allows alignment onto the position of the optical tweezers or the dipole trap. In a second step we use a piezo controlled mirror for precise alignment onto the optical tweezers.



**Fig. 5.14** Damage and deposition of optical elements due to UV light. Damaged wave plate (**left**) and coated beam sampler (**right**). The opaque layer can be removed by cleaning with isopropanol and acetone, indicating a surface contamination.

### Degradation of optical components

When operating the UV setup we experience damage and degradation of optical elements, visible as small opaque shadows on the optics, as shown in Fig. 5.14. Most optics can be cleaned using isopropanol or acetone, showing that the anti-reflection coating is not damaged, but the optics were coated with a lossy layer [157]. This can be caused if hydrocarbons are cracked by the UV radiation, causing deposition on the optics surface. We found that purging the optics with pure nitrogen ( $\approx 11/\text{min}$ ) solved this problem. Most parts of the setup shown in Fig. 5.13 are boxed. If possible large beam diameters are used to reduce the intensity and further reduce degradation. In general, care was taken to use non out-gassing materials such as vacuum compatible glues.

## 5.5 Rydberg spectroscopy

In a set of experiments we perform spectroscopy of Rydberg states for a first characterisation of the UV light and experimental setup.

The UV light couples  $S$  to  $P$  transitions, so starting from the  $4S_{1/2}$  state we can excite to the  $P_{1/2}$  and  $P_{3/2}$  states, as shown in Fig. 5.15. For all measurements presented in this work a principal quantum number of the Rydberg states of  $n = 62$  was used.

The first measurement is performed in the dipole trap, introduced in Section 3.5. The atoms are prepared in the  $F = 2, m_F = 2$  ground state by optical pumping, analogous to the state preparation of single atoms in tweezers. A magnetic field of 14 G is applied to define a quantisation axis and split the  $m_J$  levels of the Rydberg states. The UV beam is aligned along the  $x$  direction and the magnetic field is rotated by 22 degrees with respect to the  $x$  axis to mix the polarisations and couple all possible transitions. A weak 2 ms long UV pulse is applied at a trap depth of 3.5 MHz. The trap is loaded from a thermal cloud without further evaporation or cooling, which leads to thermal broadening of the transitions.

We observe five dips in the spectroscopy signal, as shown in Fig. 5.16, which we can as-

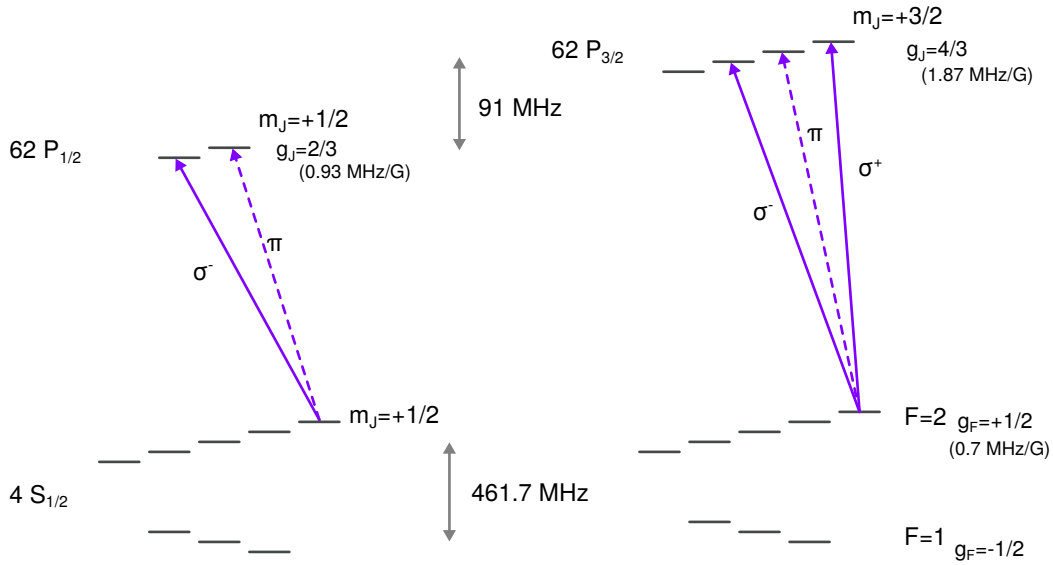


**Fig. 5.15** Level scheme for excitation to the Rydberg  $P_{1/2}$  (left) and  $P_{3/2}$  (right) states. The energies are shown for the  $n = 62$  Rydberg state. The energy splitting between Rydberg states scales as  $n^{*-3}$  with the effective quantum number  $n^*$

sign to the transitions to different  $m_J$  levels of the  $P_{1/2}$  and  $P_{3/2}$  states. The measured difference between the  $P_{1/2}$  and  $P_{3/2}$  states for no magnetic field splitting is 93.3 MHz. We calculate a theoretical splitting of 91.4 MHz with the Alkali Rydberg Calculator (ARC) python package [71, 158]. Considering the broadening due to the trapping potential with a FWHM of 5 MHz, measurement and theory agree well.

This measurement is also used to optimise the polarisation of the UV beam: Both quantisation axis and UV beam are aligned collinear and the losses of the  $4S_{1/2}F = 2, m_F = 2$  to  $P_{3/2}, m_J = -1/2$  and  $m_J = +1/2$  transitions are minimised, resulting in circular polarisation, coupling only the  $4S_{1/2}F = 2, m_F = 2$  to  $P_{3/2}, m_J = 3/2$  transition.

### 5.5.1 Electric field spectroscopy

In a second experiment we measure the energy shift of Rydberg states in a static electric field. This allows us to calibrate the electric field that is generated by the electrodes.

We perform spectroscopy of the  $P_{1/2}$  state with atoms loaded in the dipole trap, as described for the spectroscopy of the Rydberg states. A static voltage is applied to one of the upper electrodes that is parallel to dipole trap and UV beam. All other electrodes are grounded. The resonance of the Rydberg transition is measured for different voltages, as shown in Fig. 5.17. The energy shift of the Rydberg state is given by  $\Delta E = -\alpha_0/2 \cdot \mathcal{E}^2$ , with the electric field  $\mathcal{E}$  and the polarisability  $\alpha_0$  of the Rydberg state.

We calculate a polarisability of  $435.51 \text{ MHz}/(\text{V}/\text{cm})^2$  with the ARC package [71]. Fitting a quadratic function to the measured resonances yields an electric field of  $0.094 \text{ V}/\text{cm}$  for a

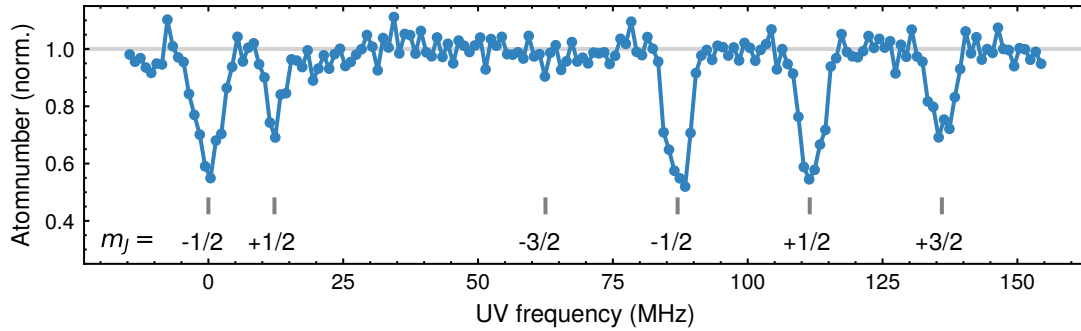


**Fig. 5.16** Spectroscopy of the  $n = 62$   $P_{1/2}$  and  $P_{3/2}$  states in the dipole trap. The atoms are prepared in the  $4S_{1/2} F = 2, m_F = 2$  state. The quantisation field of 14 G is rotated to mix the polarisations and couple all possible transitions. The two dips below 25 MHz result from the  $P_{1/2}, m_J = \pm 1/2$  states, the three dips above 75 MHz result from the  $P_{3/2}$  manifold. The UV frequency is referenced to the  $P_{1/2}, m_J = -1/2$  resonance. All Rydberg states are labelled with their  $m_J$  quantum number. The  $P_{3/2}, m_J = -3/2$  state is not coupled since  $\Delta m_J = -2$ .

voltage of 1 V applied to the electrode. We use this theoretical value to calibrate the electric field of the electrodes.

We further estimate the electric field from the electrodes with a finite element method simulation, which is performed with a simplified geometry of the electrodes as eight rods and a cylindrical objective, ignoring exact geometrical details of the objective or additional elements inside the vacuum chamber. This yields an electric field of 0.13 V/cm for 1 V applied to the same electrode as used for the measurement. Given the approximations of the simulation, the calculated values agree reasonably well with the measurement.

### 5.5.2 Linewidth and thermal broadening

In the last spectroscopic measurement we use single atoms in optical tweezers. The atoms are loaded with an effective trap depth of  $906 \mu\text{K}$ , referred to as 100% trap depth, and prepared in the  $F = 2, m_F = 2$  state. To reduce interaction effects between the atoms, we use a spacing of  $20 \mu\text{m}$  between the atoms. To keep the power levels for the intensity stabilisation similar between different experiments, we use a 5 by 5 square array, but due to the strong focusing of the UV beam to a waist of  $20 \mu\text{m}$  we only evaluate the central column of the array, which is aligned along the UV beam. The atoms are illuminated for  $100 \mu\text{s}$  with a weak UV pulse and the atom loss is measured.

In the first measurement, no additional Raman sideband cooling is used and the tweezer power is lowered to 20% of the initial value. This is the lowest possible power before atoms are lost, given the temperature without Raman sideband cooling.

In Fig. 5.18 a the data for the individual tweezers is shown for trap depth of 20% and 5 permil and with and without Raman sideband cooling. Due to the inhomogeneous trapping potentials, the individual lines are shifted by more than 1 MHz with respect to each other. These shifts are caused by aberrations in the optical setup of the SLM.

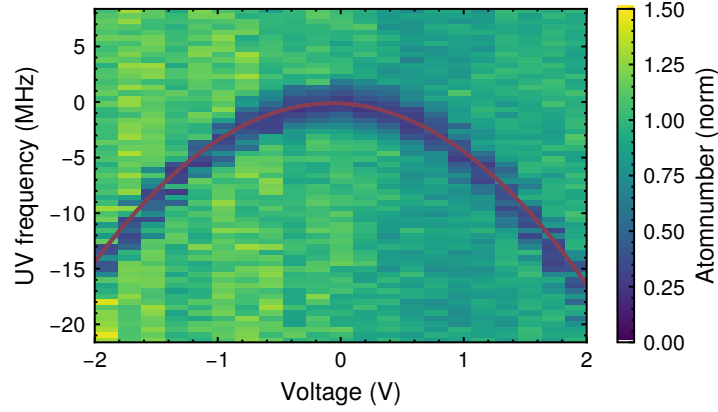


**Fig. 5.17** Spectroscopy of the  $62P_{1/2}$  Rydberg state with a static electric field. The UV frequency is referenced to the resonance at no field. A quadratic function (red line) is fitted to the measured resonances, yielding an electric field of  $0.094 \text{ V/cm}$  for a voltage of  $1 \text{ V}$ .

To evaluate the line shape and extract the temperature, the individual tweezer lines are shifted to a common centre and averaged, as shown in Fig. 5.18 c. The line shape in this non-cooled measurements shows a clear asymmetry which is fitted well by a Maxwell Boltzmann distribution

$$f(E) = \frac{E^2}{2(k_B T)^{3/2}} \cdot e^{-E/k_B T} \quad (5.6)$$

with  $T = 16 \pm 1.3 \mu\text{K}$ . Note that the temperature  $T$  depends on the trap depth  $V_0$  since  $T \propto \sqrt{V_0}$ , assuming adiabaticity [120]. This temperature agrees well with the values measured in Section 4.6.

The same measurement is repeated with Raman sideband cooling, which results in a narrower line with a Gaussian shape ( $\text{FWHM} = 386 \pm 21 \text{ kHz}$ ) and no detectable asymmetry. The reduced temperature after cooling further allows ramping the trap to a much lower power without atom loss. We perform the same measurement with cooling and ramp the tweezers to 5 permil of the initial power without additional atom loss. We observe a narrower line with a FWHM of  $112 \pm 9 \text{ kHz}$ . At this power level, the absolute variation of the resonance frequencies is about  $40 \text{ kHz}$ , smaller than the observed width of the lines. The measured linewidth is still larger than the theoretical width of the transition of  $\Gamma = 2\pi \cdot 1 \text{ kHz}$ , given by the blackbody reduced lifetime of  $\tau_r = 160 \mu\text{s}$ . We attribute this to the central Gaussian width of the laser, which we estimate from this measurement to be approximately  $100 \text{ kHz}$ . Considering the increase of the linewidth of the seed laser with up to a factor 16 in both frequency doubling stages, introduced in Section 5.3.4, this value seems reasonable. Resolving the theoretical width of the Rydberg transition would thus require a linewidth of the seed laser in the range of  $100 \text{ Hz}$ . However, for most experiments such as coherent Rabi oscillations or Rydberg dressing the current linewidth poses no limitation. The larger broadening at 20 % trap depth can be caused by the higher temperature at larger

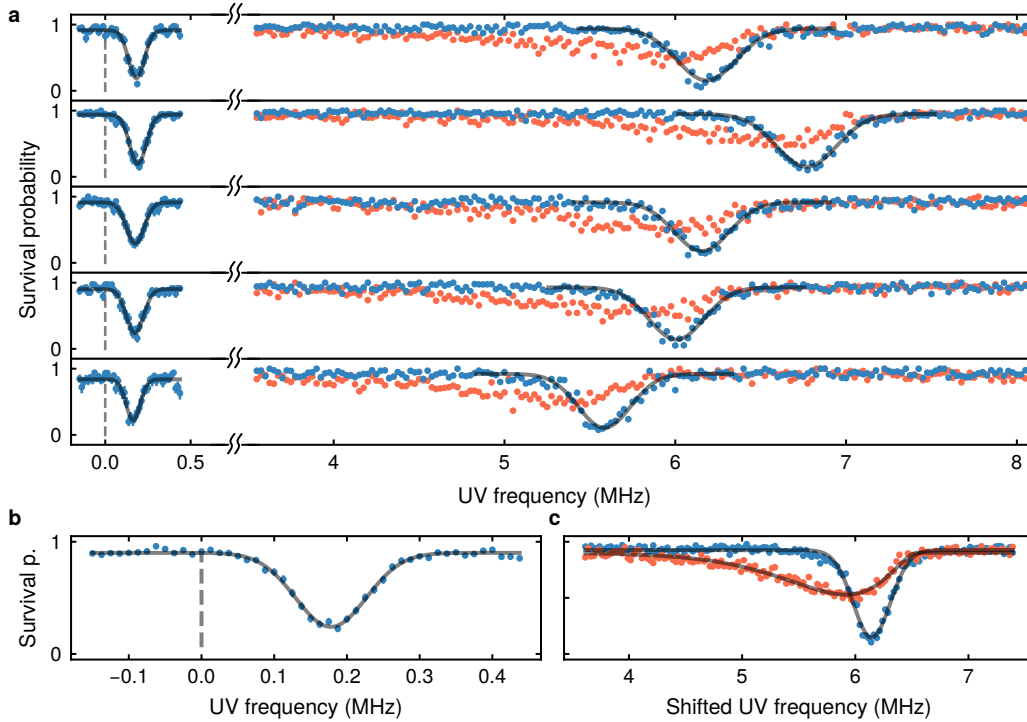


**Fig. 5.18** Spectroscopy of the  $4S_{1/2}F = 2, m_F = 2$  to  $62P_{1/2}, m_J = -1/2$  transition for different trap depths and with and without Raman sideband cooling. **a.** Spectroscopy with (blue) and without (orange) cooling at 20 percent of the tweezer power used for loading (right) and with cooling at the minimum of 5 permil power (left) for five tweezers. The grey dashed line at zero marks the free space resonance. For the measurements with sideband cooling Gaussian fits are shown in grey. **b.** Average of the individual tweezers at 5 permil trap power. **c.** The data for 20% trap power has been shifted to a common centre of the Gaussian fit before averaging. The non-cooled data is fitted with a Maxwell Boltzmann distribution.

trap depth but also from residual intensity noise and intensity drifts over the time scale of the measurement.

In conclusion, the spectroscopic measurements presented allowed us to determine the resonances of the Rydberg transitions. Using this technique the polarisation of the UV beam can be optimised and the electric field of the electrodes can be calibrated. Additionally, an upper bound for the linewidth of the UV laser can be determined. Most importantly, this measurement showed how the absolute value of inhomogeneous trap light shifts of individual tweezers can be reduced by applying Raman sideband cooling and lowering the trap depth.



## Chapter 6

### Interacting Rydberg systems

With the techniques introduced in [Chapter 4](#), we can prepare single atoms in a well-defined quantum state and close to the motional ground state of the trap. In [Chapter 5](#) we introduced the setup to generate UV light for direct excitation of Rydberg  $P$  states and presented first spectroscopic measurements of Rydberg states. We will now use these techniques for coherent control of Rydberg states and use the strong energy shift of nearby Rydberg atoms to engineer interacting many-body systems.

In [Section 6.1](#) we describe coherent Rabi oscillations between ground and Rydberg states of single atoms. Limitations and decoherence are investigated and the improvements of the above-mentioned methods such as Raman sideband cooling on coherent Rydberg Rabi oscillations are investigated.

When placing multiple atoms within the Rydberg blockade radius  $r_c$ , not all atoms can be simultaneously excited to the Rydberg state, but the atoms share one collective excitation. The observation of this so-called super atom is presented in [Section 6.2](#) and is the first demonstration of coherent interactions between single atoms in our setup.

[Section 6.3](#) moves towards Rydberg dressing. As the last part of this work, the first experimental realisation of Rydberg dressing in a tweezer array in our system is presented.

#### 6.1 Single-atom Rabi oscillations

Before using Rydberg states to induce interactions between atoms, we investigate coherent control of individual Rydberg atoms by measuring coherent Rabi oscillations between ground and Rydberg state.

Single atoms are trapped in tweezers and prepared in the  $4S_{1/2} F = 2, m_F = 2$  ground state, as described in [Section 4.2](#) and [Section 4.3](#). For some measurements Raman sideband cooling is used to prepare the atoms close to the motional ground state. The tweezer power is ramped to 20 % of the initial trap depth before being switched off completely for several microseconds. During the off-time, a short UV pulse is applied, as shown in [Fig. 6.1](#). The reduction of trap depth before the switch-off adiabatically cools the atoms and increases the survival probability, as presented in [Section 4.7](#). Switching off the trap for Rydberg excitation is a commonly-used technique, preventing light shifts as well as anti-trapping and ionisation of the Rydberg atoms due to the trapping light [[25](#), [35](#), [155](#), [159](#)]. For each set of measurements only the UV pulse duration is varied while the switch-off time is kept constant.

To keep interaction effects between neighbouring atoms small, we use a 5 by 5 array

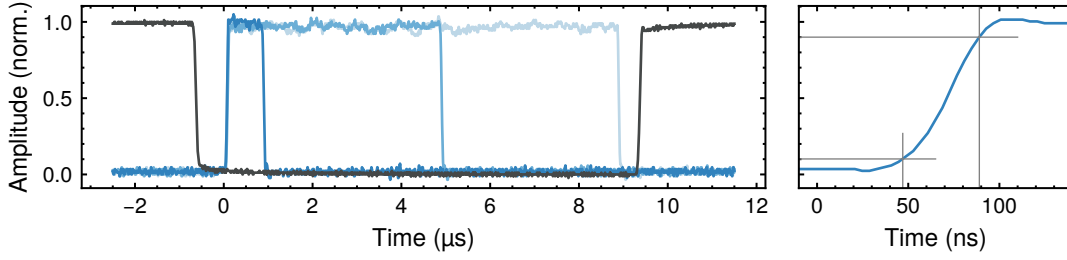


**Fig. 6.1** **Left:** Measured power of the tweezer trapping light (black) and UV pulses (blue). The trapping light is switched off for  $10 \mu\text{s}$ . Three UV pulses with durations of  $1 \mu\text{s}$ ,  $5 \mu\text{s}$  and  $9 \mu\text{s}$  are shown (dark to light blue). The pulses are stabilised with a sample-and-hold technique and no active stabilisation is used during the switch-off. The root mean square noise of the pulse amplitude is about 2% in each experimental shot. **Right:** Zoom of the switch-on of the UV pulse, showing a rise time of 40 ns, limited by the AOM.

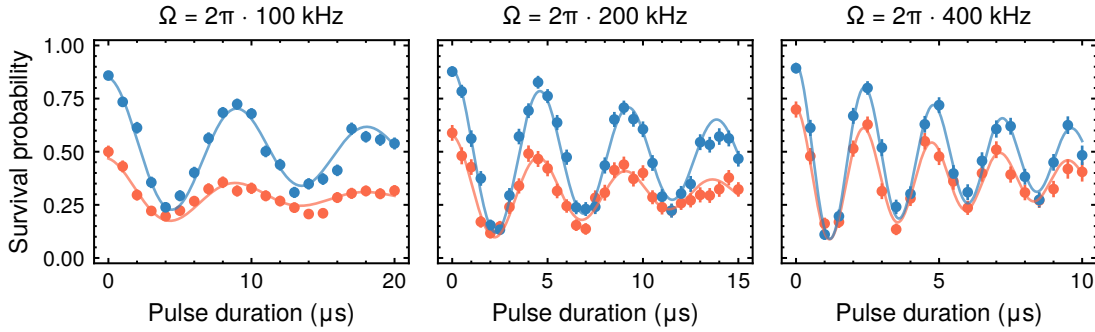


**Fig. 6.2** Resonant Rabi oscillations between the ground  $F = 2, m_F = 2$  and the Rydberg  $62P_{1/2}, m_J = -1/2$  state, averaged over five tweezers. Oscillations with (blue) and without (red) Raman sideband cooling and fit of an exponentially damped oscillation for Rabi frequencies of  $2\pi \cdot 100 \text{ kHz}$  (**left**),  $2\pi \cdot 200 \text{ kHz}$  (**middle**) and  $2\pi \cdot 400 \text{ kHz}$  (**right**).

of atoms with a spacing of  $15 \mu\text{m}$ . The UV beam is aligned onto the central column, of which all 5 traps are averaged for the analysis. The beam is focused onto the atoms with a waist of  $20 \mu\text{m}$  with circular polarisation. The maximum power used is 38 mW, yielding a Rabi frequency of  $2\pi \cdot 400 \text{ kHz}$ . For the following measurements atoms are excited to the  $62P_{1/2}, m_J = -1/2$  Rydberg state.

In **Fig. 6.2** coherent Rabi oscillations with and without RSC are shown for different Rabi frequencies. We measure the survival probability of atoms and fit an exponentially damped oscillation  $f(t) = a \cdot \cos(2\pi \cdot \Omega \cdot t) \cdot \exp(-t/\tau) + c$  to the measured signal. Since Rydberg atoms are anti-trapped by the tweezers due to the ponderomotive potential, they are lost when switching on the trap. From the fits we extract the Rabi frequency  $\Omega$  and the  $1/e$  decay time  $\tau$  of the amplitude.

Without RSC, the oscillation amplitude is decreased, since atoms are lost quickly due to the switch-off, as discussed in [Section 4.7](#). With RSC, the loss due to switch-off is negli-

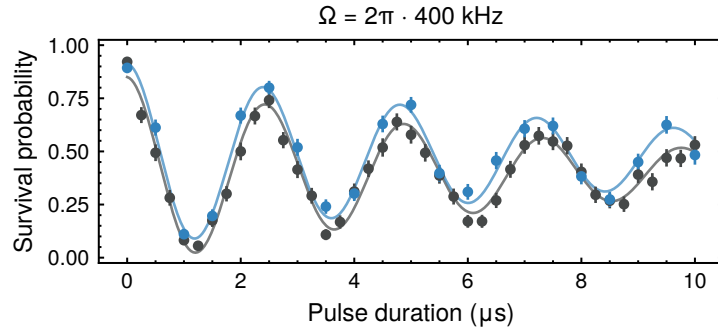


**Fig. 6.3** Rabi oscillations of  $2\pi \cdot 400$  kHz with (blue) and without (black) switching off the trap. Both measurements were performed with Raman cooling and ramping the trap to 5 permil.

ble, thus increasing the initial amplitude of the oscillations. For the lowest measured Rabi frequency of  $\Omega = 2\pi \cdot 100$  kHz, the number of coherent oscillations  $N = \Omega \cdot \tau$  is increased from  $N = 1$  without sideband cooling to  $N = 2$  with RSC. For the largest Rabi frequency of  $\Omega = 2\pi \cdot 400$  kHz, we observe no significant increase of  $N$  and calculate  $N = 3.5$  for both cases with and without RSC. This difference in behaviour is due to the different temperatures and thus the different Doppler shift  $\Delta_D$  of the atoms. With the temperatures extracted from the switch-off measurement, we calculate Doppler shifts of  $\Delta_D = 2\pi \cdot 160$  kHz before and  $2\pi \cdot 50$  kHz after Raman sideband cooling at a lowered trap depth of 20%. If the Doppler shift is larger or comparable to the Rabi frequency, coherent Rabi oscillations will be damped strongly. For larger Rabi frequencies this effect is reduced [111]. A detailed discussion of limitations and experimental errors is presented in the following section.

We calculate a theoretical Rabi frequency of  $2\pi \cdot 1.2$  MHz for a optical power of 38 mW and a waist of  $20 \mu\text{m}$ , using the ARC package [71]. This is three times the experimentally measured Rabi frequency. As we are not aware of any experimental errors that could explain such a deviation, we attribute this discrepancy of measured and calculated Rabi frequency to imperfections of the theoretical calculation. Similar deviations of a factor of two have been observed by other groups [63, 138].

As presented in Section 4.6 and Section 5.5, RSC allows us to hold atoms at lowered trap depth of 5 permil of the initial value without additional atom loss. The absolute inhomogeneous shifts between the individual traps are then reduced from  $\approx 2$  MHz for 20% trap depth to 40 kHz, much smaller than the achievable Rabi frequency. This enables us to perform Rabi oscillations in-trap, as shown in Fig. 6.3. We measure Rabi oscillations with and without switching off the trap at a lowered trap depth of 5 permil. For the in-trap measurement we adjust the detuning of the UV light by the trap light shift of 200 kHz. We observe the same performance with and without trapping light [35].

### 6.1.1 Decay of coherent oscillations

As we saw in the measurements of coherent Rabi oscillations, the number of coherent oscillations  $N$  is limited. Here, we discuss several factors that can cause such imperfec-

tions. Those can be divided into two categories: Detection errors which cause a reduction of amplitude and contrast of the observed oscillations and effects that cause damping of the oscillations. Detailed discussions of experimental imperfections can be found in References [28, 35, 111, 128, 160].

### Detection errors

Detection and state preparation errors cause a reduction of the contrast of measured Rabi oscillations, but will not cause significant damping of the oscillations over time. The main sources for such errors are state preparation, detection of ground state atoms and detection of Rydberg atoms:

- **State preparation fidelity:** Only atoms that are prepared in the correct ground state, in our case the  $m_F = 2$  state, can be excited to the Rydberg state. As described in Section 4.3, the ground state preparation fidelity is  $> 99\%$ . The resulting reduction in contrast of the Rabi oscillations is  $< 1\%$ . This effect is negligible for the measurements presented in this work.
- **Ground state atom detection fidelity:** To determine if an atom is lost, two fluorescence images of single atoms are taken. We observe atom loss of about  $5\%$  during imaging, determined by taking multiple consecutive images. This is slightly larger than the ground state detection fidelity observed by other groups with typical values between  $< 1\%$  to  $\approx 5\%$  [33, 126, 155, 161]. Since this loss is caused by imperfections of the molasses imaging it can likely be reduced by optimisation of the imaging parameters. In addition, atom loss during other steps of the experimental sequence like sideband cooling or due to vacuum losses shows the same effect. We measured both to be significantly smaller than the loss during imaging, as described in Section 4.5 and Section 4.2.
- **Detection of Rydberg states:** Atoms excited to the Rydberg state are detected indirectly by induced atom loss. Rydberg atoms are anti-trapped by the tweezer light due to the ponderomotive potential, given by  $V_P(r) = e^2 I(r) / (2m_e \epsilon_0 c \omega_L^2)$ , with the intensity  $I$  and frequency  $\omega_L$  of the laser.  $e$  and  $m_e$  are the electron charge and mass,  $c$  is the speed of light and  $\epsilon_0$  the electric constant [162, 163]. For ideal detection Rydberg atoms are ejected from the trap after the switch-on of the trapping light. Due to the finite lifetime of the Rydberg state, an atom can decay to the ground state before it is ejected from the trap, if the anti-trapping is not strong enough, leading to a false detection signal. Optical traps with closer detuning provide less anti-trapping, since the trap depth  $V_0$  scales as  $V_0 \propto I/\Delta$  with the detuning  $\Delta$  [9]. For 1064 nm trapping light in potassium, ground state and anti-trapping ponderomotive shift are equal in strength, ensuring a small false detection error [155]. The detection error due to recapture of atoms in the Rydberg state can be modelled analogously to the switch-off simulation presented in Section 4.7, including the repulsive ponderomotive potential [128]. We estimate a Rydberg state detection error of  $\epsilon_{\text{Ryd}} \approx 2\%$  for a trap depth of  $5 \mu\text{K}$  (5 permil of the initial trap depth) and  $\epsilon_{\text{Ryd}} \approx 0.5\%$  for a trap

depth of 200  $\mu\text{K}$  (20 %). To further increase this fidelity, separate Rydberg detection schemes can be used: When turning the traps back on, the intensity of the trapping light can be increased compared to the intensity before switching off the traps, to provide a strong anti-trapping of Rydberg atoms [57, 164]. This was not used for the experiments presented here, but can be easily implemented for future work if the Rydberg state detection fidelity becomes a limitation. Microwave radiation can be used to induce fast loss of Rydberg atoms before they decay to the ground state [33, 57]. In alkaline earth atoms autoionisation schemes have been successfully employed for the same purpose [35].

### Damping of Rabi oscillations

The most important sources for damping of Rabi oscillations are the Doppler shift of the atoms, intensity noise of the UV light and frequency or phase noise of the laser:

- **Doppler shift:** When the trap is switched off, motion of the atoms causes a Doppler shift  $\Delta_D$  of the resonance, given by  $\Delta_D = k \cdot v$  with the wave vector  $k = 2\pi/\lambda$  and the wavelength  $\lambda$  of the Rydberg excitation laser. The velocity  $v$  in direction of the laser beam is given by  $v = \sqrt{k_B T/m}$  with the temperature  $T$  and mass  $m$  of the atoms and the Boltzmann constant  $k_B$ . This causes a random detuning of the resonance in each experimental cycle, causing off-resonant driving of the transition with an effective Rabi frequency of  $\Omega_{\text{eff}} = \sqrt{\Omega^2 + \Delta_D^2}$ . With the temperatures extracted from the switch-off measurement presented in Section 4.7, we calculate Doppler shifts of  $\Delta_D = 2\pi \cdot 160$  kHz before and  $2\pi \cdot 50$  kHz after Raman sideband cooling at a lowered trap depth of 20 %. For increasing Rabi frequencies much larger than the Doppler shift  $\Omega \gg \Delta_D$ , this effect decreases, as shown in Fig. 6.2.
- **Intensity noise:** Changes and shot-to-shot variation of the area of the UV pulse directly cause changes of the Rabi frequency  $\Omega$  and lead to different evolutions in each experimental realisation. Intensity fluctuations limit the number of coherent oscillations to  $N = \sqrt{2}/(\pi\sigma_I)$  with the standard deviation of the pulse area  $\sigma_I$  [35].
- **Frequency and phase noise of laser:** Both frequency and phase noise of the excitation laser cause different evolutions in each experimental realisation, which causes dephasing and limits the number of coherent oscillations. Both depend on the frequency reference, mostly a high finesse optical cavity, the locking electronics and the laser itself. Improving phase noise by cavity filtering the laser or using intrinsically low phase noise lasers was shown to significantly improve the achievable number of coherent oscillations [56, 111, 155].

In addition to the effects discussed above, several others can lead to reduction of the contrast or decay of the observed oscillations: Spontaneous emission from the excited state with a blackbody reduced lifetime of 160  $\mu\text{s}$  for the  $6^2P$  states is one order of magnitude smaller than the time scale of the measurements of 10  $\mu\text{s}$ . For two-photon excitation schemes,

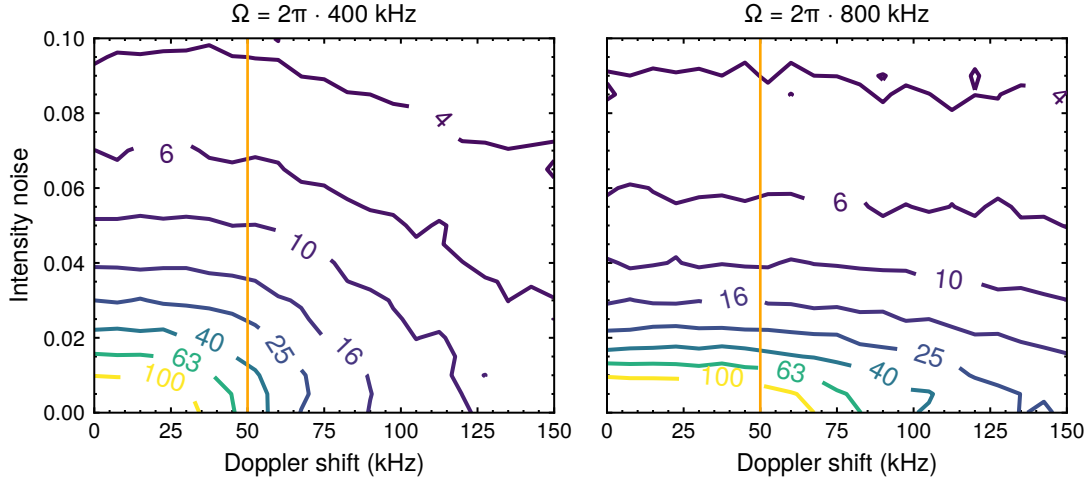


**Fig. 6.4** Monte Carlo simulation of the effects of Doppler shift and intensity noise on coherent Rabi oscillations. Contours are the number of coherent oscillations  $N = \Omega \cdot \tau$ . Intensity noise is given as a fraction of the Rabi frequency. The Doppler shift after RSC of  $2\pi \cdot 50$  kHz is indicated by orange lines. **Left:** Rabi frequency of  $2\pi \cdot 400$  kHz, corresponding to the value used in the measurements in Fig. 6.2 and Fig. 6.3. **Right:** Rabi frequency of  $2\pi \cdot 800$  kHz, showing the reduced sensitivity to Doppler shifts for higher Rabi frequencies.

the scattering rate at the intermediate state needs to be taken into account, reducing the effective lifetime of the Rydberg state and leading to asymmetric decay of the measured oscillations. Furthermore, any experimental imperfections such as residual electric fields that cause mixing of Rydberg states or drifts of the magnetic fields can cause errors. We estimate those negligible for the measurements presented.

### Simulation of Doppler shift and intensity noise

We now take a closer look at the effects of Doppler shift and intensity fluctuations with a Monte Carlo simulation to gain a better understanding on the decay of Rabi oscillations. The simulation follows the work presented in [128].

The time evolution of a three-level system with ground state  $|g\rangle$  and Rydberg states  $|r\rangle$  and  $|r'\rangle$  is simulated by solving the time-dependent Lindblad master equation

$$\dot{\rho} = -\frac{i}{\hbar}[H, \rho] + \frac{1}{2} \left[ 2c\rho c^\dagger - \rho c^\dagger c - c^\dagger c \rho \right], \quad (6.1)$$

with the density matrix  $\rho$  and the Hamilton operator  $H$ . Black-body induced decay with a rate  $\Gamma$  to neighbouring Rydberg states is simulated with decay to the auxiliary state  $|r'\rangle$  and the operator  $c = \sqrt{\Gamma} \cdot |r'\rangle\langle r|$ . The laser couples the states  $|g\rangle$  and  $|r\rangle$  with a Rabi frequency

$\Omega$  and a detuning  $\Delta$ , described by the Hamiltonian

$$H(t) = \frac{1}{2} \begin{array}{c} |r'\rangle \\ |r\rangle \\ |g\rangle \end{array} \begin{array}{ccc} \langle r'| & \langle r| & \langle g| \\ \left( \begin{array}{ccc} 0 & 0 & 0 \\ 0 & \Delta & \Omega \\ 0 & \Omega & -\Delta \end{array} \right) \end{array}. \quad (6.2)$$

The master equation is solved using the python quantum toolbox qutip [165, 166]. For the simulations presented, intensity noise is implemented by drawing the Rabi frequency from a Gaussian distribution with the center at  $\Omega_0$  and a width  $\sigma$ , modelling static shot-to-shot fluctuations.

The Doppler shift  $\Delta_D$  is given by  $\Delta_D = \mathbf{k} \cdot \mathbf{v}$  with the wave vector of the light  $\mathbf{k}$  and the velocity of the atom  $\mathbf{v}$ . Hence only the velocity component in the direction of the laser has to be taken into account. For thermal atoms the one dimensional velocity component follows a normal distribution with  $v_{1D} = \sqrt{k_B T / (m\omega^2)}$ , as introduced in Section 4.7. The Doppler shift is simulated by drawing the detuning of the laser  $\Delta$  from a Gaussian distribution with the width  $\Delta_D$ , centred around zero.

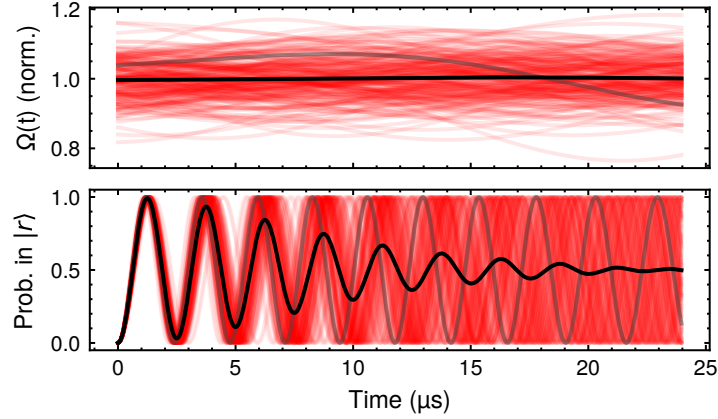
For a given Doppler shift and intensity deviation, the probability to be in the Rydberg state is calculated as a function of the UV pulse duration, by solving Eq. (6.1) for up to 20  $\mu\text{s}$ . The simulation is repeated 1000 times with each time randomly drawn intensity noise and Doppler shift. The probability for the atom to be in the Rydberg state at a given time  $t$  is averaged. The  $1/e$  decay time  $\tau$  is extracted from a fit of an exponentially damped oscillation to calculate the number of coherent oscillations  $N = \tau \cdot \Omega$ .

Fig. 6.4 shows the number of coherent oscillations  $N$  as a function of Doppler shift and intensity noise for two different Rabi frequencies. As shown in Fig. 6.2, the effect of the Doppler shift  $\Delta_D$  is reduced for higher Rabi frequencies  $\Omega$ . For off-resonant Rabi oscillations with detuning  $\Delta$ , the effective Rabi frequency is given by  $\Omega_{\text{eff}} = \sqrt{\Omega^2 + \Delta^2}$  [92]. The effect of a Doppler shift onto the effective Rabi frequency is thus quadratically suppressed for large Rabi frequencies with  $\Omega > \Delta_D$ . Without Doppler shift the effect of the intensity noise is independent of the Rabi frequency and inversely proportional to the RMS noise of the pulse area  $\sigma$  with  $N = \sqrt{2}/(\pi \cdot \sigma)$  [35].

### Time-dependent noise

Solving the full master equation further allows us to include time-dependent imperfections, such as time-dependent intensity noise (AC noise) by adding a time-dependent Rabi frequency  $\Omega \rightarrow \Omega(t)$ . To model the noise we use two methods: Either 200 sine functions with random phases, amplitudes and frequencies are added, where the frequencies are centred at  $f_c$  with a bandwidth  $f_{bw}$ . Alternatively white noise is created and bandpass filtered. Both methods show no significant difference in the simulated decay.

In Fig. 6.5, the individual Rabi frequencies  $\Omega(t)$  for 200 realisation with the resulting time-evolutions of the population in the Rydberg state are shown. The noise has a central frequency of  $f_c = 2\pi \cdot 20$  kHz with a bandwidth of  $f_{bw} = 2\pi \cdot 40$  kHz and a root-mean-square



**Fig. 6.5** Simulation of Rabi oscillations with time-dependent noise. Each red line represents one of 200 realisations, with an exemplary one highlighted in grey. The average is shown in black. **Top:** Normalised Rabi frequencies  $\Omega(t)/\Omega_0$  with a central noise frequency of  $2\pi \cdot 20$  kHz and a bandwidth of  $2\pi \cdot 40$  kHz. The RMS deviation of the noise is 5%. **Bottom:** Probability for the atom to be in the Rydberg state, obtained from solving the Master equation, for all realisations of  $\Omega(t)$ .

(RMS) deviation of 5%. The Doppler shift  $\Delta_D = 2\pi \cdot 50$  kHz. Averaging the 200 realisations shows a damped oscillation with  $N \approx 4$  coherent oscillations.

In Fig. 6.6 the effects of a variable frequency  $f_c$  of noise with a bandwidth of  $f_{bw} = 40$  kHz and a Rabi frequency of  $\Omega = 2\pi \cdot 400$  kHz are shown. High frequency noise, starting at one tenth of the Rabi frequency, averages over multiple Rabi oscillations and thus reduces the number of coherent oscillations  $N$  less with increasing frequency. At high noise frequencies  $N$  is limited by the Doppler shift  $\Delta_D = 2\pi \cdot 50$  kHz. For frequencies below 10 kHz the noise is static over the simulated duration of 25  $\mu$ s. The simulation shows that high frequency noise is less critical than long term drifts.

As discussed, decay is caused by intensity noise, frequency fluctuations and phase noise. Since the limitation of intensity noise is independent of the Rabi frequency for noise that remains constant at a given ratio of the intensity, we compare the improvements of increased Rabi frequency to number of coherent oscillations. In addition to measurements presented in Fig. 6.2, we measure oscillations to the  $62P_{3/2}, m_J = -3/2$  state. Due to the larger dipole matrix elements, we achieve Rabi frequencies of  $\approx \Omega = 2\pi \cdot 600$  kHz and observe an increase up to  $N \approx 10$  coherent oscillations. We can thus determine an upper limit of 5% on the intensity noise present in our setup. Intensity noise can not only be caused by intensity fluctuations of the laser beam, but also by beam motion, since the intensity has a Gaussian distribution. For a waist of 20  $\mu$ m, beam motion of 2  $\mu$ m with an initial displacement from the centre of the Gaussian beam of 2  $\mu$ m already causes an intensity change of 3%. We further observe a reproducible dependence of  $N$  to the parameters of the laser lock, which effectively changes the power spectral density of the phase noise in certain frequency ranges.

Given this dependence to locking parameters and that we observe improvements for higher

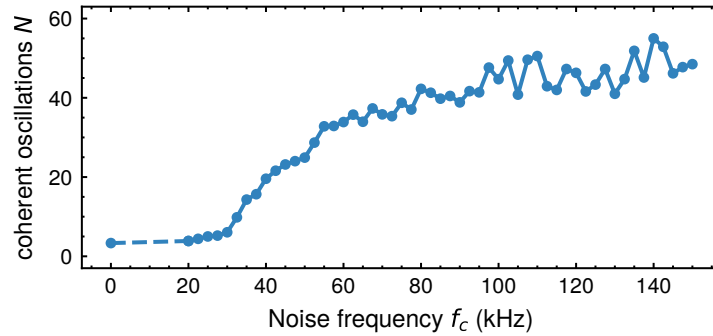


**Fig. 6.6** Number of coherent oscillations  $N$ , depending on the central frequency  $f_c$  of AC noise with a bandwidth of  $2\pi \cdot 40$  kHz and RMS deviation of 5%. For low frequencies the noise can be assumed static, limiting  $N$  to a few coherent oscillations. For large noise frequencies,  $N$  is only limited by the Doppler shift of  $2\pi \cdot 50$  kHz. The left point at 0 kHz is calculated for static shot-to-shot changes with the same RMS deviation.

Rabi frequencies implies that intensity noise is not the limiting source of error in our system. Improvements on phase and frequency noise have been reported to significantly increase the number of coherent oscillations up to  $N = 30$  to 50 coherent oscillations [56, 57, 111, 155]. We conclude that laser noise is limiting the performance in our system. By implementing the same techniques such as frequency filtering the laser with a high finesse cavity, we expect to significantly increase  $N$  in future work.

## 6.2 Rydberg blockade and superatom

In the experiments presented so far, atoms were placed with large distances  $> 15 \mu\text{m}$  to ensure negligible atom-atom interactions, for example to measure coherent Rabi oscillations between ground and Rydberg state or perform spectroscopy, allowing the observation of pure single-atom dynamics. Placing atoms close to each other leads to interactions between Rydberg atoms. If multiple atoms are close enough, one Rydberg excitation will shift the remaining atoms out of resonance, preventing multiple excitations to the Rydberg state, as illustrated in Fig. 6.7. This effect is called Rydberg blockade and is the key mechanism to engineer atom-atom interactions and simulate quantum systems or implement quantum gates [24, 25, 27, 28, 33, 34, 159, 164, 168–172].

For larger ensembles of atoms, only one single excitation is shared between all atoms, called a superatom [62, 173–175]. In the experiment described in this section we measure coherent Rabi oscillations between the ground and this collective state of the superatom. The long range interaction, called the van-der-Waals (vdW) interaction, causes the Rydberg blockade in our setup. It can be characterised by the  $C_6$  coefficient, that is defined in second

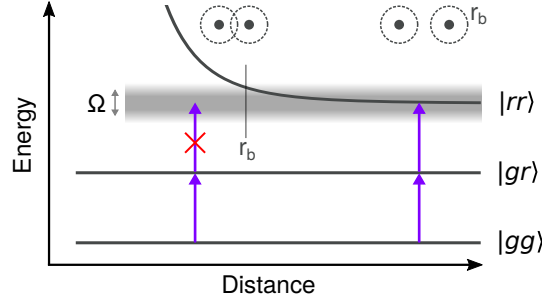


**Fig. 6.7** Illustration of Rydberg blockade for two atoms. For large separation between two atoms, initially prepared in the ground state  $|gg\rangle$ , both atoms can be both excited to the Rydberg state  $|rr\rangle$ . For small distances the van-der-Waals interaction of one atom in the Rydberg state shifts the resonance of the second atom, preventing the excitation to  $|rr\rangle$ . The transition is broadened by the Rabi frequency  $\Omega$ . The blockade radius  $r_b$  is defined as distance where the interaction shift equals the Rabi frequency and prevents more than one Rydberg excitation in the system.

order perturbation theory as

$$C_6 = \sum_{r'r''} \frac{|\langle r'r'' | V(r) | rr \rangle|^2}{\Delta_{r',r''}}, \quad (6.3)$$

with the pair states  $|rr\rangle$  and the energy difference between the states  $\Delta$ . The sum is taken over all dipole coupled pair states with the interaction potential  $V(r)$ . The energy shift of the Rydberg state is then given by  $\Delta E = -C_6/r^6$ . The blockade radius is defined as the maximal distance where the interaction shift prevents excitation of multiple atoms into the Rydberg state, that is  $r_b = \sqrt[6]{|C_6|/\Omega}$ , with the Rabi frequency  $\Omega$ . In our case the  $C_6$  coefficient of the  $62P_{3/2}$  state is on the order of  $100 \text{ GHz} \cdot \mu\text{m}^6$ , resulting in a blockade radius of approximately  $7 \mu\text{m}$  [71]. The interaction shift has a strong angular and magnetic field dependence, shown in Fig. 6.8.

The discussion so far assumed the idealised system of one ground and one Rydberg state. Multiple additional pair states exist, that will be strongly shifted for small inter-atomic distances. Compared to the often-used alkali elements rubidium and caesium, the level splitting in potassium is considerably smaller: For potassium, the energy difference between the  $62P_{1/2}$  and  $62P_{3/2}$  states is 91 MHz, for rubidium 416 MHz and for caesium 1076 MHz. For the small splitting of potassium, other pair state manifolds may overlap, especially for short distances or large magnetic fields. Residual imperfect polarisation components can then couple to other than the desired pair states. The relevant pair states as a function of atom-atom distance are shown in Fig. 6.9. We use the  $62P_{3/2, m_J = -3/2}$  state with a quantisation field of 5 G. For distances smaller than  $4.5 \mu\text{m}$ , other pair states from the  $P_{3/2}P_{3/2}$  and the  $P_{3/2}P_{1/2}$  manifold are shifted to resonance. The minimal atom-atom distance of  $5 \mu\text{m}$  in the measurements presented, ensures a clean system with well-defined coupling to the desired states.

As mentioned before, for multiple atoms that are placed within one blockade radius, one

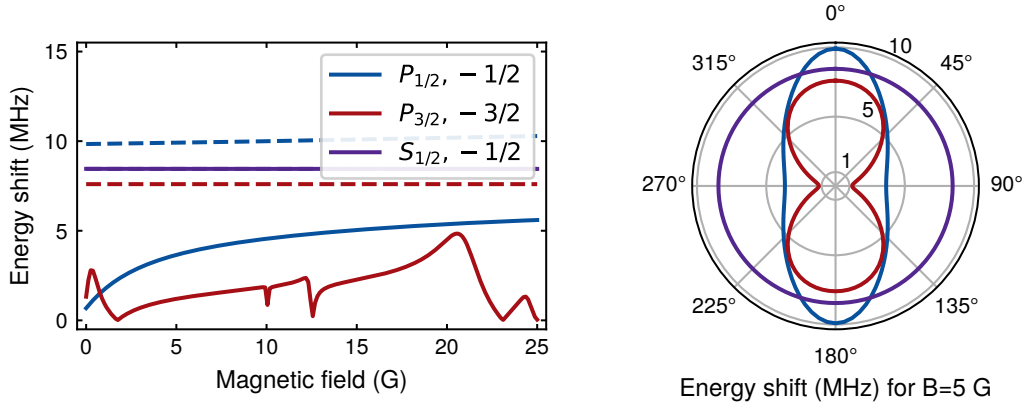


**Fig. 6.8** Calculation of the Rydberg interaction energy shift for two atoms at a distance of  $5 \mu\text{m}$ . **Left:** Energy shift as a function of magnetic field for the  $S_{1/2}$ ,  $P_{1/2}$  and  $P_{3/2}$  states for angles of 0 degrees (dashed lines) and 90 degrees (solid lines) between inter-atomic and quantisation axis. Due to splitting of the  $m_J$  states the energy shift of the  $P_{3/2}$  state shows a strong dependence on the magnetic field. **Right:** Energy shift as a function of angle between inter-atomic and quantisation axis for a magnetic field of 5 G. Calculations were performed with the python package pairinteraction [167].

excitation shifts all remaining atoms out of resonance, preventing more than one excitation of the whole system. The system with  $N$  atoms can be described by the two states  $|G\rangle$  and  $|W\rangle$  with

$$|G\rangle = |g_1, g_2, \dots, g_N\rangle \quad \text{and} \quad (6.4)$$

$$|W\rangle = \frac{1}{\sqrt{N}} \sum_{i=1}^N |g_1, \dots, r_i, \dots, g_N\rangle, \quad (6.5)$$

where the subscripts label the atoms. The Hamiltonian of the system is given by

$$H = \frac{\hbar\sqrt{N}\Omega}{2} (|G\rangle\langle W| + |W\rangle\langle G|) - \hbar\Delta|W\rangle\langle W|, \quad (6.6)$$

where  $\Omega$  is the single-atom Rabi frequency and  $\Delta$  the single-atom detuning. If the system is driven on resonance, it will oscillate between the ground state  $|G\rangle$  and collective state  $|W\rangle$  with a collectively enhanced frequency of  $\sqrt{N} \cdot \Omega$ .

For the measurement of the superatom all atoms are prepared in the the  $F = 2, m_F = -2$  ground state. No Raman sideband cooling is applied, as the measurement was performed at an early stage of building the experimental setup. The UV laser has  $\sigma^-$  polarisation, coupling to the  $6^2P_{3/2}, m_J = -3/2$  state. Four atoms are placed in a block of 2 by 2 atoms with a spacing of  $5 \mu\text{m}$ , as shown in Fig. 6.10. This block is repeated 4 times with a larger spacing of  $15 \mu\text{m}$  along the direction of the UV beam to increase statistics. Interactions between the blocks are negligible due to the large spacing. A magnetic field of 5 G, oriented

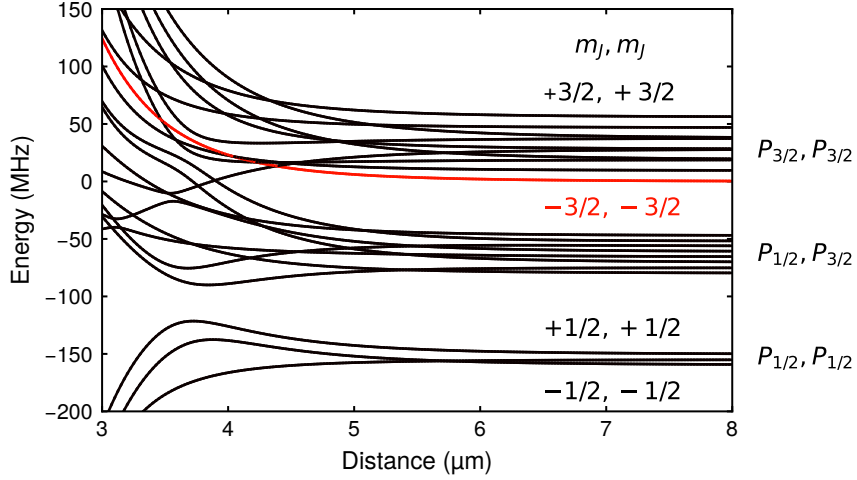


**Fig. 6.9** Relevant pair state level structure for the  $P$  state manifold. A quantisation field of 5 G splits the different  $m_J$  levels. The energetically highest and lowest pair states are marked with their respective  $m_J$  quantum numbers. The  $m_{J_1} = -3/2, m_{J_2} = -3/2$  pair state that is used in the superatom measurements is highlighted in red. Calculations were performed with the python package pairinteraction [167].

along the direction of the UV beam, is applied to separate the individual  $m_J$  levels and define a quantisation axis.

Since the loading probability of the individual traps is about 50%, the measured data is post-selected for an initial loading of 1 to 4 atoms. The measured Rabi oscillations for each set of post-selected data is shown in Fig. 6.10. The difference in the size of the errorbars is explained by the large difference in experimental realisations for different numbers of atoms. Due to the stochastic loading probability, for 1 or 2 atoms up to 400 individual realisations are averaged for each data point, while for 4 atoms only 34 realisations are used for each point.

We extract Rabi frequencies of  $\Omega(N = 1) = 2\pi \cdot 403 \pm 2$  kHz,  $\Omega(2) = 2\pi \cdot 569 \pm 5$  kHz,  $\Omega(3) = 2\pi \cdot 677 \pm 8$  kHz and  $\Omega(N = 4) = 2\pi \cdot 762 \pm 8$  kHz by fitting an exponentially damped oscillation to each set of measurements.

As shown in Fig. 6.8, all atoms are situated well within one blockade radius.

Despite a limited detection efficiency of 83% and therefore reduced contrast, we observe a superatom of up to individual 4 atoms. The observed root scaling of the Rabi frequency with the number of atoms  $N$ , as shown in Fig. 6.10 and the excitation of maximally one atom to the Rydberg state indicate the realisation of the entangled collective  $|W\rangle$  state. This is the first realisation of Rydberg induced atom-atom interaction and entanglement of multiple atoms in our setup.

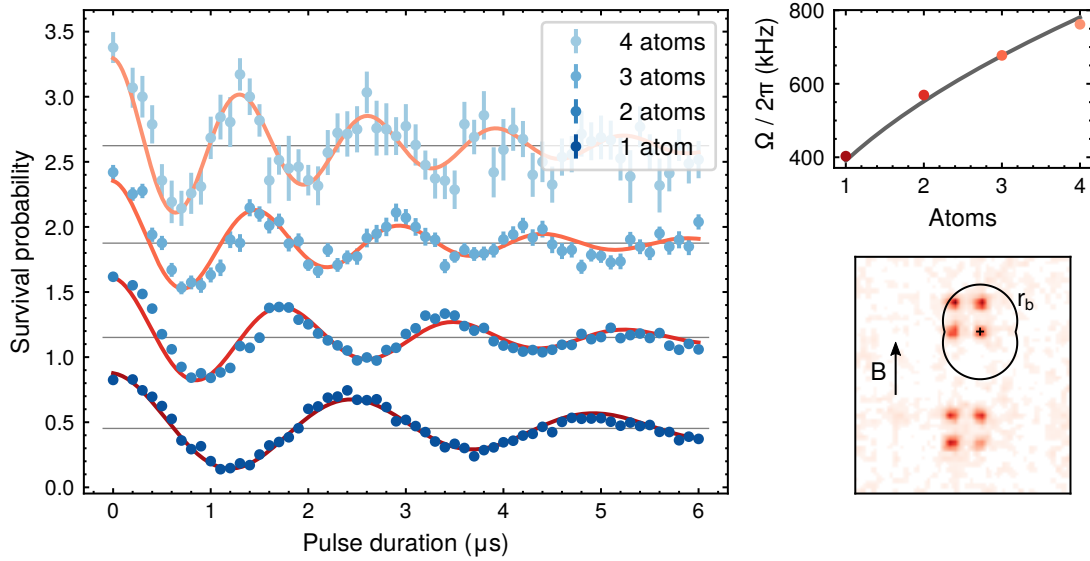


**Fig. 6.10** Measurement of collective Rabi oscillations: **Left:** Survival probability after the UV pulse, post-selected on an initial loading of 1 to 4 atoms. No discrimination is made between different configurations of the initially loaded atoms. The blue points are the measured values, the red lines are fits with an exponentially damped oscillation. Error bars denote the standard deviation from averaging. **Top right:** Rabi frequency  $\Omega$  extracted from the fits as a function of atoms  $N$ . The grey line shows the square root scaling  $\Omega(N) = a \cdot \sqrt{N}$  with the amplitude  $a$  as the only free parameter, confirming the excitation to the collective  $|W\rangle$  state. **Bottom right:** Averaged atom picture of two blocks with the blockade radius  $r_b$  of one atom indicated by a black line.

## 6.3 Rydberg dressing

We now shift the focus away from resonant excitation of Rydberg atoms to Rydberg dressing. This technique is used to engineer long range interactions in optical lattices or bulk systems [42, 43, 64, 73, 176, 177]. In optical tweezers it has so far only been used in the context of quantum gates with two individual atoms [74].

In this section, first the basic theory is explained, followed by the description of the first experimental realisation of dressed interactions in our system.

### 6.3.1 Theory of Rydberg dressing

In the following, the key ideas of Rydberg dressing are introduced. A detailed discussion and derivation can be found in References [41, 42, 74, 138, 178, 179]. We assume a laser that couples the ground state  $|g\rangle$  to the Rydberg state  $|r\rangle$  of an atom with Rabi frequency  $\Omega$  and detuning from resonance  $\Delta$ . Two atoms are placed at a distance  $r$  from each other, interacting via the van-der-Waals potential  $V(r) = C_6/r^6$  with the  $C_6$  coefficient, introduced in Section 6.2. The two-atom basis is composed of the state  $|gg\rangle$  with both atoms in the ground state,  $|rr\rangle$  with both atoms in the Rydberg state and the state

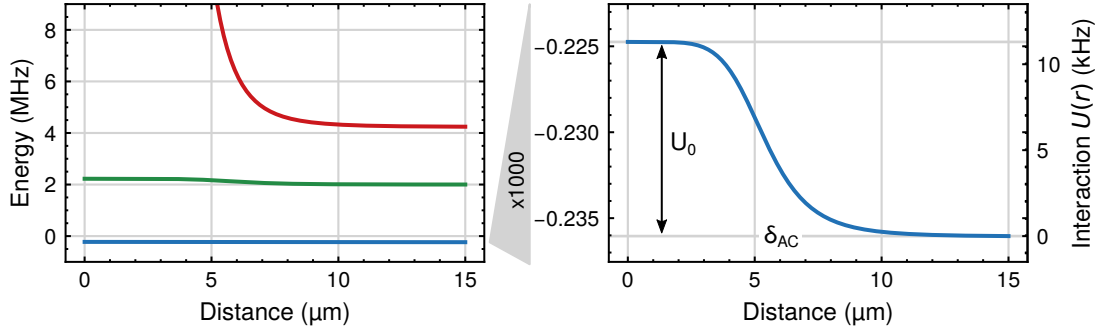


**Fig. 6.11** **Left:** Eigenenergies of the dressed states  $|gg\rangle$ ,  $|+\rangle$  and  $|rr\rangle$  as a function of interatomic distance obtained by diagonalising the Hamiltonian (Eq. (6.7)) with  $\Omega = 1$  MHz,  $\Delta = -2$  MHz and  $C_6 = 100$  GHz  $\cdot \mu\text{m}^6$ . Due to the strong interaction of  $V(r)$  for short distances, the  $|rr\rangle$  state is strongly shifted for  $r < 6 \mu\text{m}$ . **Right:** Eigenenergies of the  $|gg\rangle$  state for the same parameters with a magnified energy axis, showing the characteristic soft core potential for Rydberg dressing with a soft core radius of  $r_c = 5.4 \mu\text{m}$ . For large distances the energy shift is given by the non-interacting AC Stark shift  $\delta_{AC}$ .

$|+\rangle = 1/\sqrt{2}(|gr\rangle + |rg\rangle)$  of only one atom being in the Rydberg state. The asymmetric state  $|-\rangle = 1/\sqrt{2}(|gr\rangle - |rg\rangle)$  is a dark state of the system and can be eliminated, as described in Reference [138]. We focus on the ‘weak dressing’ limit with  $\Delta > \Omega$ . However, the ‘strong dressing’ regime with  $\Delta \leq \Omega$  is covered by the same theory [74].

The system is described by the Hamiltonian

$$H(t) = \frac{\hbar}{2} \begin{array}{c} |gg\rangle \\ |+\rangle \\ |rr\rangle \end{array} \begin{array}{ccc} \langle gg| & \langle +| & \langle rr| \\ \left( \begin{array}{ccc} 0 & \sqrt{2}\Omega & 0 \\ \sqrt{2}\Omega & -2\Delta & \sqrt{2}\Omega(t) \\ 0 & \sqrt{2}\Omega(t) & -4\Delta + 2V(r)/\hbar \end{array} \right) & & \end{array} \quad (6.7)$$

In Fig. 6.11 the eigenenergies of Hamiltonian  $H$  as a function of interatomic distance are shown. For Rydberg dressing we are interested in the behaviour of the state  $|gg\rangle$ . For large distances  $r \rightarrow \infty$  the ground state shift of  $|gg\rangle$  is only given by the AC Stark shift  $\delta_{AC}$  of two individual atoms with

$$\delta_{AC} = -2 \times \frac{\hbar}{2} \left( \Delta + \sqrt{\Omega^2 + \Delta^2} \right) \approx 2 \times \hbar \frac{\Omega^2}{4\Delta}. \quad (6.8)$$

For shorter distances, the the ground state  $|gg\rangle$  is additionally shifted by the interaction  $U$

due to the admixture of the Rydberg state. The interaction  $U$  is given by

$$U(r) = \frac{U_0}{1 + (r/r_c)^6}, \quad (6.9)$$

$$r_c = \left| \frac{C_6}{2\hbar\Delta} \right|^{1/6}, \quad (6.10)$$

$$U_0 = \frac{\hbar\Omega^4}{8\Delta^3}, \quad (6.11)$$

with the interaction strength  $U_0$  and the soft core radius  $r_0$ .

Besides the interaction strength, the lifetime of the dressed atoms is important. During dressing a small fraction of the Rydberg character is admixed to the ground states. This admixture  $\beta$  is given by

$$\beta = \frac{\Omega}{2\Delta}. \quad (6.12)$$

The probability for an atom to be in the Rydberg state is then given by  $\beta^2$ , reducing the effective lifetime  $\tau_{\text{eff}}$  of the dressed state to

$$\tau_{\text{eff}} = \frac{\tau_r}{\beta^2}, \quad (6.13)$$

with the lifetime of the Rydberg state  $\tau_r$ .

The maximally reachable ratio  $R$  of the interaction timescale to dissipation rate due to Rydberg state decay is then

$$R = \frac{\Omega^2\tau_r}{2\Delta}. \quad (6.14)$$

This ratio is only limited by the available laser power and thus the maximum achievable Rabi frequency  $\Omega$ . For reasonable experimental values with a Rabi frequency of  $2\pi \cdot 1$  MHz, a detuning of  $2\pi \cdot 3$  MHz and a Rydberg state lifetime of  $\tau_r = 160 \mu\text{s}$  (for  $62P$ ), coherence ratios of  $R \approx 25$  are reachable.

So far, we have assumed a perfect single-frequency laser with a  $\delta$  function as spectral profile. We now discuss the effect of the laser linewidth on Rydberg dressing. The spectral profile of a real laser is better approximated by a combination of a Gaussian and Lorentzian line shape, as illustrated in Fig. 6.12 [103, 180]. We measured a Gaussian width of 100 kHz (see Section 5.5). For Rydberg dressing, due to the large detuning, mainly the wings of the laser profile, described by a Lorentzian profile, are important.

The effective width of an atomic transition  $\Gamma_{\text{eff}}$  is then given by the convolution of the Lorentzian profile of the transition with a width of  $\Gamma_r = 1/\tau_r$  and the spectral profile of the laser. Due to the Lorentzian width of the laser  $\Gamma_L$ , the wings of the effective profile are also Lorentzian with an effective width of  $\Gamma_{\text{eff}} = \Gamma_r + \Gamma_L$ . The additional scatter, caused by the Lorentzian width of the laser, thus reduces the effective Rydberg state lifetime. For

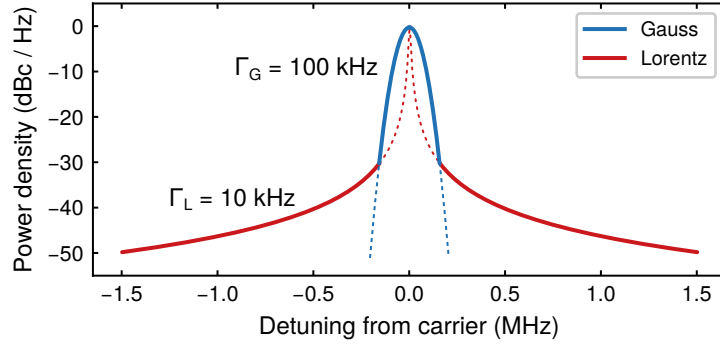


**Fig. 6.12** Illustration of the spectral profile of a laser. The central part, called the carrier, is described by a Gaussian profile with a linewidth (FWHM) of  $\Gamma_G = 100$  kHz. Further away the laser follows a Lorentzian line shape with a FWHM of  $\Gamma_L = 10$  kHz.

a Rydberg linewidth of  $\Gamma_r = 2\pi \cdot 1$  kHz, a Lorentzian laser with  $\Gamma_L = 2\pi \cdot 9$  kHz reduces the effective lifetime and thus the coherence to dissipation ratio  $R$  by a factor of 10. This shows the importance of using a laser with low noise, especially at the detuning used for Rydberg dressing, which is in the range of a few megahertz in our case. Since the Rydberg lifetime including blackbody-induced decay scales as  $\tau_r \propto n^2$ , this effect is less severe in experiments which use low principle quantum numbers  $n$  [42, 43, 64, 177].

### 6.3.2 Dressed interactions

In a first set of measurements we determine the lifetime of the Rydberg dressed atoms  $\tau_{\text{eff}}$  and the single particle AC stark shift  $\delta_{AC}$ . Afterwards, the interaction induced-phase shift of Rydberg dressing is measured, confirming dressed interactions in our system.

The effective lifetime of the dressed state  $\tau_{\text{eff}}$  is measured as follows: To ensure negligible interactions between the atoms, an array with  $15 \mu\text{m}$  spacing is used. For all presented dressing experiments, atoms are initially prepared in the  $F = 2, m_F = 2$  ground state and dressed with the the  $62P_{1/2}, m_J = -1/2$  Rydberg state. Since the measurements were performed at an earlier stage of building the experimental setup, the tweezer trap depth was lowered to 5% of the initial value of approximately 1 mK rather than the value of 5 permil, used in the measurements presented above.

We first determine the dressed lifetime by measuring atom loss as a function of the UV pulse duration with a Rabi frequency of  $2\pi \cdot 320$  kHz, as shown in Fig. 6.13. An exponential decay with amplitude and decay time  $\tau$  as free parameters is fitted to extract the dressed lifetime  $\tau_{\text{eff}}$ . The measurement is performed for multiple detunings  $\Delta$ , showing a significant deviation by about a factor 10 of the measured lifetime to the theoretically predicted one of Eq. (6.13), with a blackbody limited Rydberg state lifetime of  $160 \mu\text{s}$  [71]. We explain this by an additional Lorentzian linewidth of the UV laser. As discussed before, additional phase noise and Lorentzian linewidth of the laser cause a broadening of the transition, reducing the effective lifetime. Our measurement suggests a Lorentzian width of the laser

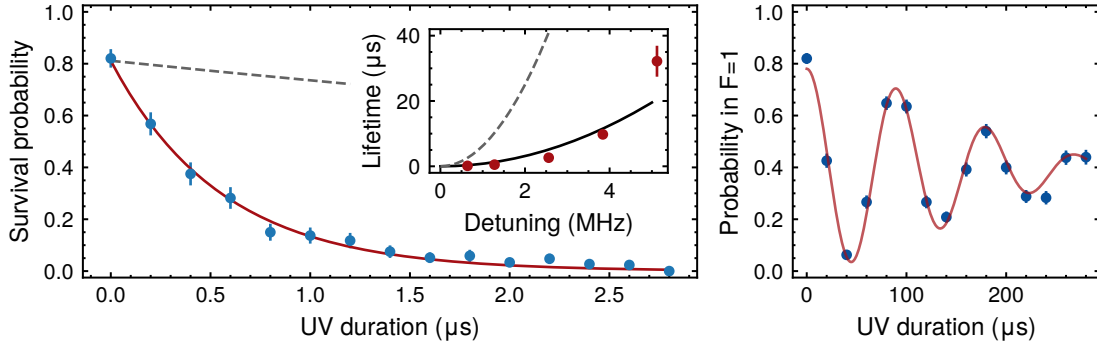


**Fig. 6.13** **Left:** Lifetime measurement of single dressed atoms for  $\Omega = 2\pi \cdot 320$  kHz and  $\Delta = 4\Omega = 2\pi \cdot 1.3$  MHz. The atoms are separated by  $15 \mu\text{m}$ , preventing interaction shifts. An exponential fit is used to extract the dressed lifetime  $\tau$ . The inset shows lifetimes as a function of detuning. The measured lifetimes are significantly lower than the theoretical prediction with a Rydberg state lifetime of  $\tau = 160 \mu\text{s}$ , shown in dashed grey for both plots. Assuming an additional Lorentzian width of the laser of  $2\pi \cdot 7$  kHz, the effective lifetime is reduced to  $\tau = 20 \mu\text{s}$ , shown in black for the inset. **Right:** Ramsey measurement of the ground states  $F = 2, m_F = 2$  to  $F = 1, m_F = 1$  transition. The Ramsey pulses are resonant if no additional UV light is applied. The measured oscillation frequency of  $2\pi \cdot 11$  kHz is a direct measurement of the single-atom AC stark shift  $\delta_{AC}$  cause by the UV light.

of about  $\Gamma_{\text{laser}} = 2\pi \cdot 7$  kHz in the UV. This shows a good performance of our seed laser, considering the scaling of phase noise and linewidth during frequency doubling, discussed in Section 5.3.4, and reported Lorentzian linewidth for similar ECDLs of  $2\pi \cdot 14$  kHz [103]. A reduced lifetime will limit the maximally achievable interaction time, but not limit our measurement for a first observation of Rydberg dressed interactions.

For all following experiments the atoms are placed along a line with 25 sites and a spacing of  $4 \mu\text{m}$ . The Rabi frequency of the UV light is  $\Omega = 2\pi \cdot 320$  kHz and the detuning  $\Delta = 6\Omega = 2\pi \cdot 1.9$  MHz. To measure the single-atom AC stark shift  $\delta_{AC}$ , presented in Eq. (6.8), we use a Ramsey measurement with two  $\pi/2$  pulses and a  $\pi$  rephasing pulse on the ground state transition between  $F = 2, m_F = 2$  and  $F = 1, m_F = 1$ . After the second  $\pi/2$  pulse all atoms in the  $F = 2, m_F = 2$  state are removed using resonant light on the D2 transition, as described in Section 4.8. All pulses are resonant on the ground state transition. In between the first  $\pi/2$  and the  $\pi$  pulse a UV pulse is applied. The experimental sequence is similar to the one used to measure dressed interactions, as shown in Fig. 6.14, but only one UV pulse is applied. A shift of the  $m_F = 2$  state causes an oscillation of the measured Ramsey signal. The measured oscillation frequency is  $2\pi \cdot 11$  kHz. The theoretical calculation predicts  $\delta_{AC} = 2\pi \cdot 13$  kHz, where the Rabi frequency  $\Omega$  and detuning  $\Delta$  were measured independently using a spectroscopy and observing resonant Rabi oscillations. Due to the small separation of the atoms, interactions change the measured shift. The correction can be estimated by the interaction shift  $U_0$  from Eq. (6.11) as  $\delta_{\text{corr}} \approx N_{\text{eff}}/2 \cdot U_0$  with the number of atoms inside the softcore radius  $N_{\text{eff}}$ . This shift is on the order of  $2\pi \cdot 200$  Hz and is neglected [138]. We attribute the discrepancy of measured

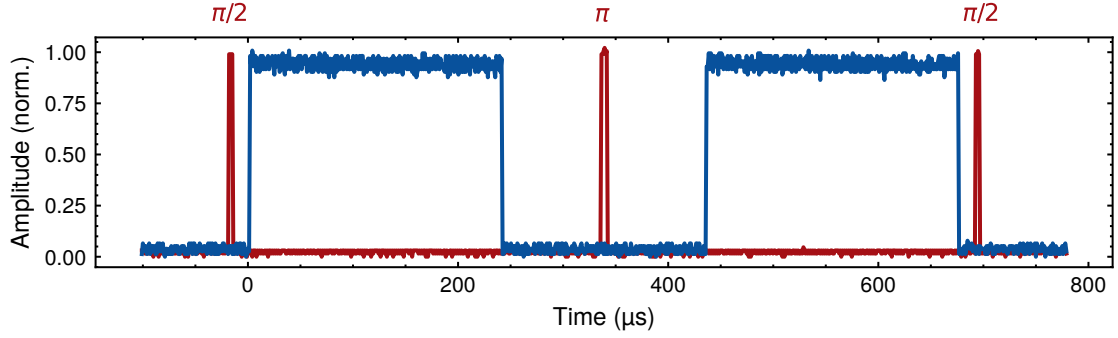


**Fig. 6.14** Oscilloscope trace of the experimental sequence for Rydberg dressing. A spin echo Ramsey sequence on the ground state  $F = 2, m_F = 2$  to  $F = 1, m_F = 1$  transition is used to observe dressing (red). The  $\pi$  pulse is applied symmetrically in between the UV dressing light to cancel the AC stark shift  $\delta_{AC}$ . Only the duration of the UV pulses is changed for the measurement while keeping all other timings constant. For the measurement of the AC stark shift the same sequence with only the first UV pulse is used.

and calculated shift to inhomogeneous trap light shifts, as discusses below.

Lastly, we measure the interactions that are induced by Rydberg dressing. We use a Ramsey sequence to measure the interaction-induced phase shift, as shown in Fig. 6.14. This sequence is similar to the Ramsey measurements presented in Section 4.8 and in References [42, 138].

We calculate an interaction strength  $U$  with a separation of  $4 \mu\text{m}$  between two atoms as  $U(r = 4 \mu\text{m}) = 2\pi \cdot 168 \text{ Hz}$  with a peak interaction strength  $U_0 = 2\pi \cdot 185 \text{ Hz}$  and a soft core radius of  $r_c = 5.86 \mu\text{m}$ . This corresponds to correlated phase shifts of  $\phi = \int_0^t U(t') dt' = U \cdot t = 36$  degrees for the maximum dressing time of  $t = 600 \mu\text{s}$ . The next nearest neighbour interaction strength is  $U(r = 8 \mu\text{m}) = 2\pi \cdot 25 \text{ Hz}$ .

In the experimental sequence the atoms are first prepared in a superposition of both ground states  $F = 2, m_F = 2$  and  $F = 1, m_F = 1$ , using a resonant  $\pi/2$  pulse. In the Bloch sphere picture the atoms are rotated onto the equator of the sphere. After  $350 \mu\text{s}$  a  $\pi$  pulse then rephases the atoms by rotating them by 180 degrees on the Bloch sphere, cancelling all single-atom light shifts after a second hold time of  $350 \mu\text{s}$ . A second  $\pi/2$  pulse with a phase shift of 180 degrees compared to the first two pulses is applied. This pulse maps the atoms onto the  $F = 1, m_F = 1$  ground state. Afterwards, a resonant pulse on the D2 line removes all atoms in the  $F = 2, m_F = 2$  state such that only atoms in  $F = 1$  are detected.

So far we did not consider any UV pulses for Rydberg dressing in between the Ramsey pulses. Interactions induce correlated phase shifts of two atoms, that collectively rotate the Bloch vectors of two atoms out of the plane of the Bloch sphere. Such correlated shifts are not cancelled by the  $\pi$  pulse. These correlated phase shifts are converted to correlated atom losses by the second  $\pi/2$  pulse and the pushout of all atoms in the  $F = 2, m_F = 2$  state. To measure those correlated atom losses, we calculate the two-body correlation

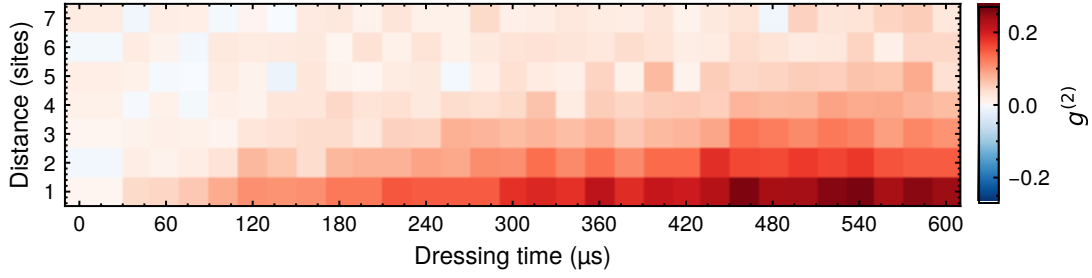


**Fig. 6.15** Correlator  $g_{ij}^{(2)}$  for distances of 1 to 7 sites in a one dimensional chain of atoms as a function of dressing time. In the absence of UV light the system shows no correlations. For increasing dressing times next-neighbour correlations build up and for longer pulse durations long-range correlations become visible.

function as follows:

We assign a detected atom to the value 1 and a lost atom to  $-1$ , always conditioned on an initially loaded atom. This definition ensures a symmetric correlator with  $g_{ij}^{(2)} = 0$  for an uncorrelated system. The two body correlator  $g^{(2)}$  between sites  $i$  and  $j$  is defined as

$$g_{ij}^{(2)} = \left\langle (n_i - \langle n_i \rangle) \cdot (n_j - \langle n_j \rangle) \right\rangle, \quad (6.15)$$

with the mean value of the  $i^{\text{th}}$  site  $\langle n_i \rangle$ . The correlator is evaluated up to a distance of 7 sites ( $j = i \pm 7$ ) along the chain, as shown in Fig. 6.15. The growth of correlations in the system for increasing dressing times shows a first signal of Rydberg dressed interactions in our system.

### Experimental imperfections

However, this first realisation of Rydberg dressing has several experimental imperfections, which are discussed in the following:

- **Loading probability:** The loading probability of the tweezers is 50%. This half-filled chain of atoms prevents coherent interactions or revivals as measured in Reference [41]. The implementation of resorting is planned as a future upgrade of the setup, enabling the observation of dynamics of deterministically prepared fully loaded arrays of single atoms [106].
- **Rydberg dressed lifetime:** We measure the lifetime of Rydberg dressed states and attribute the reduction of up to a factor 10 compared to the theoretically expected values to the laser parameters. This limits the reachable coherence ratio  $R$  from Eq. (6.14) to below 1. Without a reduced lifetime we calculate  $R = 4$ , which should allow to observe coherent interactions. The critical parameters such as phase noise and linewidth were identified and solutions discussed. Future upgrades of the seed

laser will increase both coherent Rabi oscillations and resonant experiments as well as Rydberg dressing.

- **Inhomogeneities:** The measurement was performed with a minimum trap depth of 5 %, one order of magnitude higher than the later achieved minimum depth of 5 permil. This is due to the measurement being performed at an initial stage of building the experiment without fully optimised parameters for Raman sideband cooling. Due to the inverse cubic scaling of the interaction strength  $U_0$  with the detuning  $\Delta$ , inhomogeneous tweezer light shifts on the order of 10 % cause differences in the interactions of about 50 % over the chain of atoms. With the optimised system, presented in [Section 4.6](#), the inhomogeneous light shifts are lowered by a factor of 10, reducing the changes in interaction strength to about 4 %. A further reduction is possible at larger detunings, which can be compensated by an increase in Rabi frequency.

In this chapter we investigated the coherent control of Rydberg states and used the strong interaction between Rydberg atoms to induce interactions in arrays of individual atoms. We first measured coherent Rabi oscillations and analysed the experimental imperfections. Monte Carlo simulations of experimental errors helped us to gain an understanding of the effects of multiple imperfections. By placing multiple atoms within one blockade radius, we could create an entangled state of 4 atoms, called a superatom, and drive coherent oscillations to this collective state. In the last part we presented Rydberg dressing as an alternative scheme to engineer interactions. Multiple improvements for dressing were implemented during this work. Raman sideband cooling now enables ramping the tweezer trap depth to very low values of a few permil of the depth used for loading and imaging, reducing variations of the dressed interaction due to inhomogeneous light shifts to a negligible level [181]. Despite these imperfections, we observe a clear signature of long-range interactions up to four sites.

## Chapter 7

### Conclusion and outlook

#### 7.1 Conclusion

In this thesis, we present an optical tweezer platform using potassium atoms which is well-suited for quantum simulation. In the first part of the thesis, we discuss how Rydberg atoms can be used to induce interactions among atoms and introduce Rydberg dressing as a method to simulate spin models. Simultaneous dressing of multiple ground states enables the design of complex long-range interactions to study, for example, frustrated quantum systems. Furthermore, important properties for Rydberg dressing and optical tweezer arrays are discussed and we explain the rationale behind using potassium.

We introduce the experimental setup which provides cold atomic samples and present how atoms can be trapped in arrays of optical tweezers. The techniques for preparation of atoms in a defined quantum state are introduced, and a preparation fidelity of the  $F = 2, m_F = \pm 2$  states of better than 99% was achieved.

In the next step, Raman sideband cooling for preparation of atoms close to the motional ground state is introduced and characterised. We used multiple techniques to overcome limitations, arising from strong anti-trapping of the excited states of potassium and the weak axial confinement in optical tweezers. We achieved mean vibrational quantum numbers of  $\langle \bar{n}_{rad} \rangle = 0.23$  and  $\langle \bar{n}_{ax} \rangle = 1.1$  in the radial and axial direction for an array of 64 atoms. The best performance for a single tweezer was  $\bar{n}_{rad} = 0.13$  and  $\bar{n}_{ax} = 0.23$  with a ground state probability of 69%. The performance was mainly limited by the inhomogeneities of the trapping potential. Additional sideband cooling improved the trap depth at which atoms remain trapped by a factor of 50, down to a few micro Kelvin. This reduced absolute inhomogeneities of trap light shifts to a negligible level, a key requirement for Rydberg dressing. For resonant Rydberg excitation the trapping potential was switched off for a few microseconds. Sideband cooling improved the maximum achievable switch-off time from  $2 \mu s$  to  $15 \mu s$ . Additionally, lower initial temperatures allowed further cooling of the atoms by adiabatic lowering of the trap and increased the maximum switch-off time to  $20 \mu s$ , an improvement by one order of magnitude.

We introduce coherent ground state control using an optical Raman transition, completing our experimental toolbox for preparation and coherent control of single atoms.

Atoms are excited to Rydberg states with large principal quantum numbers via the direct transition using UV light. We describe the calculation and design of the high power laser setup, including two cavity-enhanced second harmonic generation doubling stages, providing nearly one Watt of UV light. Spectroscopy of Rydberg states was used to characterise

the performance of our laser-setup and to extract an upper bound of the Gaussian linewidth of 100 kHz in the UV.

Combining all techniques presented in this work for preparation and control of single atoms and generation of UV light, we present coherent control of Rydberg states with single atoms. We discuss experimental imperfections and sources of errors, such as detection fidelities, Doppler shifts and noise of the laser. Numerical simulations helped us gain an understanding of those effects. We conclude that phase and frequency noise as well as intensity drifts of the laser are the strongest limitations in our current setup.

As the first presentation of an interacting system, we performed coherent oscillations of up to four individual atoms to a collective entangled state. This measurement of a so-called superatom is the first demonstration of interacting many-body systems in our setup.

In the last part, we move towards off-resonant Rydberg dressing and describe how this can be used to induce interactions among ground state atoms. We characterised the system and observed a reduction in the dressed lifetime, which we attribute to the Lorentzian linewidth of the laser. Measuring the induced interactions in a chain of atoms, we observed two body correlations, the first demonstration of Rydberg dressed interactions in our setup. While these first measurements, taken at an early stage of setting up the experiment, were limited by trap inhomogeneities, Raman sideband cooling will reduce this experimental error to a negligible level. We additionally discuss further improvements which will reduce remaining experimental errors such as phase noise of the laser to a negligible level. This will enable the use of Rydberg dressed interactions to study large-scale quantum many-body systems and realise simultaneous dressing of both ground states.

## 7.2 Outlook

Since the field of optical tweezers and Rydberg atoms for quantum simulation has grown rapidly over the last years, many technical challenges were solved and impressive results achieved. However, there are still challenges that remain and which were only discussed briefly in this thesis. We now discuss several important limitations and potential solutions:

- **Maximum number of coherent interactions:** A key number for any experimental implementation, both in terms of quantum computing and quantum simulation, is the number of coherent interactions  $N$  that can be achieved. We observed up to  $N = 4$  oscillations in the measurements presented in this work, which was mainly limited by phase and intensity noise of the laser. For Rydberg atoms in optical tweezers, this maximum is currently  $N \approx 50$ , with Rabi frequencies in the range of 1 to 10 MHz [35, 56, 155]. Those were achieved with a reduction in phase noise of the lasers, either by filtering the light in an optical cavity or by the use of intrinsically low-noise sources such as titanium-sapphire lasers. Additionally, increasing the Rabi frequency helped to reduce the effect of Doppler shifts. We constructed a filter cavity to reduce the phase noise of the UV seed laser, which will be implemented into our setup for future measurements. A general limitation is the available optical power, both important for high Rabi frequencies but also to provide homogeneous interactions over an array

of tweezers [57]. Technological advances enable the use of high power fibre lasers. Alternatively, optical cavities can be used to significantly enhance the optical power.

- **Experimental time scale:** While the interaction strength can be increased, for example by an increase of Rabi frequency or the use of Förster resonances, the time scale for Rydberg experiments is limited. For most experiments presented, the trapping potential is switched off during excitation to Rydberg states, limiting the experimental time to about  $10 \mu\text{s}$ . Cooling the atoms close to their motional ground state increased this time by one order of magnitude in our experimental setup. Alternatively, Rydberg atoms can be trapped in engineered trapping potentials [163, 182–184]. This extends the usable time scales to the black-body reduced lifetime of the Rydberg states on the order of  $100 \mu\text{s}$ . While this limits the usable experimental timescale, with sufficiently high coupling strength the interaction time is long enough for quantum simulation [52].
- **Black-body radiation:** Rydberg atoms have long radiative lifetimes, compared to low principal quantum number states, before they decay back to their ground state. At room temperature, this lifetime is significantly reduced by black-body radiation, driving transitions to energetically close Rydberg states. Atoms in those states with different orbital parity will interact via the long-range dipole-dipole potential that scales as  $U \propto r^{-3}$ . In atomic arrays, the decay of a Rydberg atom to such a black-body coupled state cannot be treated as a simple atom loss, since it shifts the resonances of multiple surrounding atoms. This can lead to line broadening or avalanche losses in the system [42, 43, 185–187]. Solutions are cryogenic environments to directly reduce black-body radiation or selective depumping of undesired Rydberg states. Here, the energetically closest Rydberg states with the strongest effect on the black-body reduced lifetime are coupled to low-lying states with short lifetimes. For Rydberg dressing, ‘stroboscopic dressing’ was presented as a possible solution, where short pauses in the interactions allow undesired Rydberg impurities to decay. Here, our system with flexible placement of individual atoms is an ideal platform to study such effects and add valuable insight to understanding this problem.
- **Inhomogeneities of tweezer arrays:** As presented in this work, inhomogeneities of the trap depth in an array of tweezers are a severe limitation for Rydberg dressing. While SLMs can compensate for optical aberrations, experimental implementations are typically limited to about 10% inhomogeneities, even with the use of feedback techniques [16, 57]. An intrinsic problem is the measurement of aberrations at the position of the atoms, with feedback times for each iteration on the order of several minutes. Raman sideband cooling enabled us to hold atoms at low enough trap depth such that the absolute inhomogeneous shifts are negligible for Rydberg dressing. Another solution is the use of optical lattices: Atoms can be loaded and sorted in tweezers and then be transferred into a lattice [127]. Here only large scale variations due to the harmonic confinement are present, which can be compensated. If a lattice with a short spacing over-samples the tweezer spacing, the trap frequencies can be significantly increased. This is not only advantageous for Raman sideband cooling

but also important to reduce the momentum kick onto atoms when using pulses from strongly focussed beams for single atom addressing. This approach thus combines the advantages of tweezers with those of optical lattices, and avoids long cycle times and additional steps such as evaporative cooling. Since our setup was planned to be compatible with bi-chromatic super-lattices at 532 nm and 1064 nm in all three dimensions, it is well-suited for this approach.

Despite these challenges, optical tweezers are a promising platform for large-scale quantum simulation, offering configurable arrays of interacting single atoms. A variety of technical problems have already been solved, while for others, such as black-body induced Rydberg impurities, a better understanding is still needed. The experimental platform presented in this work is well-suited to study limitations such as Rydberg impurities and tackle the problems of inhomogeneous trapping potentials by using optical tweezers in combination with optical lattices.

In our experimental setup the immediate next steps include the implementation of a filter cavity for the seed laser of the UV setup, as phase noise of the laser was identified as one of the main limitations for coherent Rydberg dressing [188]. Additionally, sorting of atoms using acousto-optic-deflectors will enable the deterministic preparation of defect-free arrays [106].

With these improvements, the system is ideal for the implementation of spin models, in which fundamental many-body problems can be studied. Rydberg dressing enables engineering of complex Hamiltonians with tunable angular and distant-dependent interactions. This enables, for example, the study of frustrated quantum systems and variational quantum optimisation [29–31, 44].

## Appendix A

### Potassium 39 level scheme

In Fig. A.1 the relevant levels  $4S_{1/2}$ ,  $4P_{1/2}$  and  $4P_{3/2}$  of the D1 and D2 line of  $^{39}\text{K}$  are shown. A detailed discussion of the properties of potassium can be found in References [189, 190]. The transitions used for the magneto-optical trap and grey molasses cooling are marked.

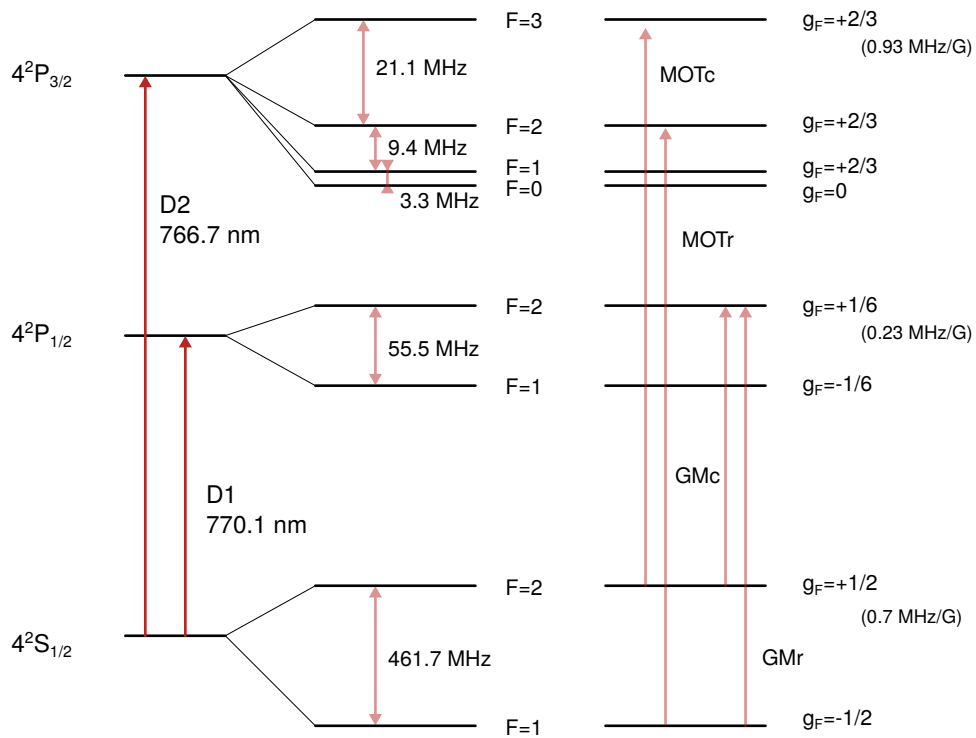


**Fig. A.1** Level scheme of  $^{39}\text{K}$  with the relevant levels of the D1 and D2 transition, relevant for slowing and cooling the atoms. The transitions used for the magneto optical trap (MOT) and grey molasses cooling (GM) are marked by red arrows. Additionally the  $g_F$  factors and resulting magnetic field shifts are shown.

## A.1 Light shifts of the excited states

As discussed in Section 2.2 and Chapter 4, the excited  $4P_{3/2}$  and  $4P_{1/2}$  states are strongly anti-trapped for a trap wavelength of 1064 nm. This is caused by the  $4P_{1/2} \leftrightarrow 3D$  and  $4P_{3/2} \leftrightarrow 3D$  resonances at 1169.7 nm and 1177.6 nm. This strong shift required the implementation of several techniques like chopping of the trapping light for successful experiments with single potassium atoms. As a reference the light shift as a ratio to the ground state light shift at 1064 nm of all  $F$  and  $m_F$  states for both the  $4P_{3/2}$  and  $4P_{1/2}$  states are given in Table A.1 and Table A.2.

State	$\sigma_+$	$\pi$
$4P_{3/2} F = 3, m_F = 3$	-8.03	-4.03
$4P_{3/2} F = 3, m_F = 2$	-6.70	-5.20
$4P_{3/2} F = 3, m_F = 1$	-5.59	-5.90
$4P_{3/2} F = 3, m_F = 0$	-4.72	-6.13
$4P_{3/2} F = 3, m_F = -1$	-4.08	-5.90
$4P_{3/2} F = 3, m_F = -2$	-3.68	-5.20
$4P_{3/2} F = 3, m_F = -3$	-3.51	-4.03
$4P_{3/2} F = 2, m_F = 2$	-6.70	-5.20
$4P_{3/2} F = 2, m_F = 1$	-5.94	-5.20
$4P_{3/2} F = 2, m_F = 0$	-5.19	-5.20
$4P_{3/2} F = 2, m_F = -1$	-4.43	-5.20
$4P_{3/2} F = 2, m_F = -2$	-3.68	-5.20
$4P_{3/2} F = 1, m_F = 1$	-5.71	-5.67
$4P_{3/2} F = 1, m_F = 0$	-5.65	-4.27
$4P_{3/2} F = 1, m_F = -1$	-4.20	-5.67
$4P_{3/2} F = 0, m_F = 0$	-5.19	-5.20

**Tab. A.1** Light shifts of the excited  $4P_{3/2}$  states for circular and linear polarisation as ratio of the ground state shift. A minus sign indicates anti trapping.

State	$\sigma_+$	$\pi$
$4P_{1/2} F = 2, m_F = 2$	-7.18	-5.66
$4P_{1/2} F = 2, m_F = 1$	-6.41	-5.66
$4P_{1/2} F = 2, m_F = 0$	-5.65	-5.66
$4P_{1/2} F = 2, m_F = -1$	-4.89	-5.66
$4P_{1/2} F = 2, m_F = -2$	-4.13	-5.66
$4P_{1/2} F = 1, m_F = 1$	-4.89	-5.66
$4P_{1/2} F = 1, m_F = 0$	-5.65	-5.66
$4P_{1/2} F = 1, m_F = -1$	-6.41	-5.66

**Tab. A.2** Light shifts of the excited  $4P_{1/2}$  states for circular and linear polarisation as ratio of the ground state shift. A minus sign indicates anti trapping.



## Appendix B

### Histograms and discrimination for single tweezers

For single atom imaging the fluorescence light during molasses cooling is detected, as discussed in [Chapter 4](#). In each fluorescence picture a small region of interest of several pixels is assigned to each atom and the pixel values are summed up. In [Fig. B.1](#) a histogram for an 8 by 8 array of atoms is shown, where the signals of all individual tweezers are summed. In [Fig. B.2](#) the data is shown for one quarter of the array. By setting a threshold in between both peaks, we can distinguish between no or one loaded atom.

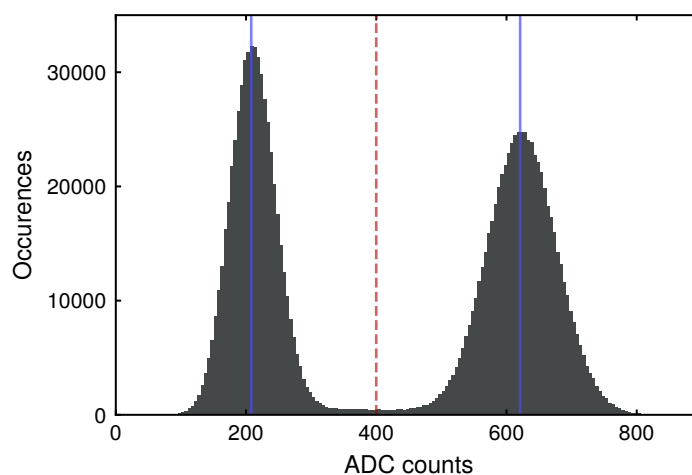


**Fig. B.1** Histogram of 64 tweezers in an 8 by 8 array. The two peaks are attributed to no atom (left) and one atom (right). The centre of each peak is marked by a blue line. The threshold for discrimination of zero or one atom is shown in red.

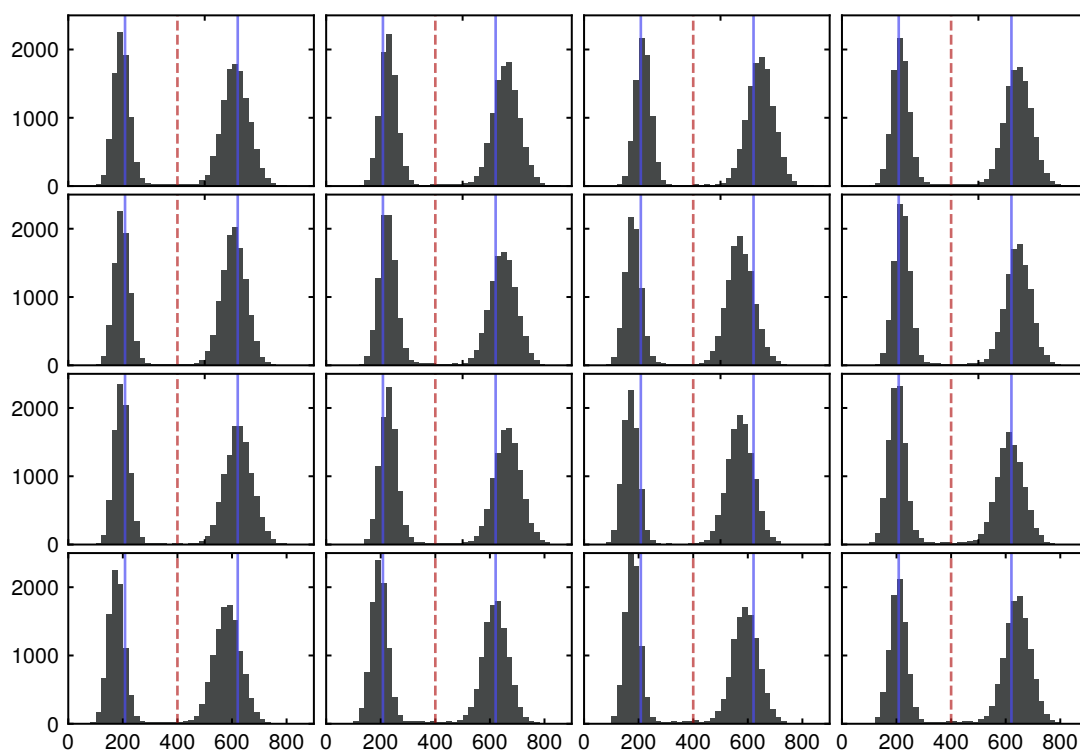


**Fig. B.2** Single tweezer histograms: For reference the blue lines indicating the centre and red lines for atom number discrimination are identical to the averaged histogram of all tweezers in Fig. B.1. All axis have the same scale.

## Danksagung

Diese Arbeit wäre ohne die Hilfe und Unterstützung vieler Leute so nicht möglich gewesen. Dafür möchte ich mich hier bedanken:

Immanuel, vielen Dank für die Möglichkeit, meine Promotion in deiner Gruppe und diesem spannenden Feld anfertigen zu können.

Danke Christian, für die Chance an diesem neuen Experiment mitarbeiten zu können. Vielen Dank für die Unterstützung und unzähligen Diskussionen, egal, ob es um das richtige Verschrauben von Wasserverbindungen, Datenauswertung mit Python oder die großen Fragen der Physik ging. Auch war ich immer von deiner Fähigkeit beeindruckt, zu erkennen welche Probleme optimale Lösungen erfordern und wo ein Stück Klebeband oder Kabelbinder reichen.

Mein besonderer Dank gilt dem Team Kalium: Zuerst meinem Mitdoktoranden Lorenzo, mit dem ich zusammen in einem Labor mit zwei leeren optischen Tischen angefangen habe und wo wir zusammen in 4 Jahren ein super Experiment aufgebaut haben: Mille grazie! Außerdem Marcel für die gute Zeit und vielen guten Stunden im Labor, auch wenn du leider dem wahren Kalium-39 abtrünnig geworden bist. Lea, vielen Dank für die großartige Unterstützung im Labor und die Hilfe im Kampf mit dem UV-setup. Vielen Dank und auch viel Erfolg für die Zukunft der ‚next generation‘ an Doktoranden, Philip und Robin. Und natürlich auch vielen Dank an Zaijun, Anne-Sophie, Sarah, Joop, Rebecca, Ina, Florian und Anton.

Anton, vielen Dank für die Hilfe bei Design und Konstruktion des experimentellen Aufbaus und die unzähligen kleinen und großen technischen Lösungen im Labor. Danke natürlich auch an das Team der MPQ-Werkstatt. Vielen Dank an Karsten für die Hilfe bei allen Problemen mit der Elektronik, dem fortwährenden Optimieren von Photodioden und mehreren Abenden ‚ground-loop-hunting‘ im Labor.

Der gesamten AG Bloch: Danke an Kristina und Doreen für die administrative Unterstützung und die Organisation der group retreats. Danke auch den Teams der Labore Single Atoms, Lithium, Polare Moleküle und Strontium für die vielen Diskussion, Journal Clubs und auch das unkomplizierte Leihen und Tauschen von Laborequipment. Ein besonderer Dank geht an das MPQ Bouldersteam: Jens, Marcel, Philip, Andreas und Thomas für die vielen schönen morgendlichen Boulder-sessions.

Meinen Eltern: Vielen Dank für eure Unterstützung.

Danke Kathrin ♡



## References

- [1] Prodan, J., A. Migdall, W. D. Phillips, I. So, H. Metcalf, and J. Dalibard. *Stopping Atoms with Laser Light*, Physical Review Letters **54.**, 992–995 (Mar. 1985). DOI: [10.1103/PhysRevLett.54.992](https://doi.org/10.1103/PhysRevLett.54.992) (cit. on p. 1).
- [2] Chu, S., L. Hollberg, J. E. Bjorkholm, A. Cable, and A. Ashkin. *Three-dimensional viscous confinement and cooling of atoms by resonance radiation pressure*, Physical Review Letters **55.**, 48–51 (July 1985). DOI: [10.1103/PhysRevLett.55.48](https://doi.org/10.1103/PhysRevLett.55.48) (cit. on p. 1).
- [3] Davis, K. B., M. O. Mewes, M. R. Andrews, N. J. van Druten, D. S. Durfee, D. M. Kurn, and W. Ketterle. *Bose-Einstein Condensation in a Gas of Sodium Atoms*, Physical Review Letters **75.**, 3969–3973 (Nov. 1995). DOI: [10.1103/PhysRevLett.75.3969](https://doi.org/10.1103/PhysRevLett.75.3969) (cit. on p. 1).
- [4] Anderson, M. H., J. R. Ensher, M. R. Matthews, C. E. Wieman, and E. A. Cornell. *Observation of Bose-Einstein Condensation in a Dilute Atomic Vapor*, Science **269.**, 198–201 (July 1995). DOI: [10.1126/science.269.5221.198](https://doi.org/10.1126/science.269.5221.198) (cit. on p. 1).
- [5] DeMarco, B. and D. S. Jin. *Onset of Fermi Degeneracy in a Trapped Atomic Gas*, Science **285.**, 1703–1706 (Sept. 1999). DOI: [10.1126/science.285.5434.1703](https://doi.org/10.1126/science.285.5434.1703) (cit. on p. 1).
- [6] Schrödinger, E. *Are There Quantum Jumps? Part II*, The British Journal for the Philosophy of Science **3.**, 233–242 (Nov. 1952) (cit. on p. 1).
- [7] Takamoto, M., F.-L. Hong, R. Higashi, and H. Katori. *An optical lattice clock*, Nature **435.**, 321–324 (May 2005). DOI: [10.1038/nature03541](https://doi.org/10.1038/nature03541) (cit. on p. 1).
- [8] Ludlow, A. D., M. M. Boyd, T. Zelevinsky, S. M. Foreman, S. Blatt, M. Notcutt, T. Ido, and J. Ye. *Systematic Study of the Sr 87 Clock Transition in an Optical Lattice*, Physical Review Letters **96.**, 033003 (Jan. 2006). DOI: [10.1103/PhysRevLett.96.033003](https://doi.org/10.1103/PhysRevLett.96.033003) (cit. on p. 1).
- [9] Grimm, R., M. Weidemüller, and Y. B. Ovchinnikov. *Optical dipole traps for neutral atoms*, Adv. At. Mol. Opt. Phys. **42**, 95 (Feb. 1999). DOI: [10.1016/S1049-250X\(08\)60186-X](https://doi.org/10.1016/S1049-250X(08)60186-X) (cit. on pp. 1, 9, 37, 84).
- [10] Bakr, W. S., J. I. Gillen, A. Peng, S. Fölling, and M. Greiner. *A quantum gas microscope for detecting single atoms in a Hubbard-regime optical lattice*, Nature **462.**, 74–77 (Nov. 2009). DOI: [10.1038/nature08482](https://doi.org/10.1038/nature08482) (cit. on pp. 1, 35).
- [11] Sherson, J. F., C. Weitenberg, M. Endres, M. Cheneau, I. Bloch, and S. Kuhr. *Single-atom-resolved fluorescence imaging of an atomic Mott insulator*, Nature **467.**, 68–72 (Sept. 2010). DOI: [10.1038/nature09378](https://doi.org/10.1038/nature09378) (cit. on pp. 1, 20, 35).

- 
- [12] Cheuk, L. W., M. A. Nichols, M. Okan, T. Gersdorf, V. V. Ramasesh, W. S. Bakr, T. Lompe, and M. W. Zwierlein. *Quantum-Gas Microscope for Fermionic Atoms*, Physical Review Letters **114.**, 193001 (May 2015). DOI: [10.1103/PhysRevLett.114.193001](https://doi.org/10.1103/PhysRevLett.114.193001) (cit. on pp. 1, 7, 10, 43, 51).
- [13] Omran, A., M. Boll, T. A. Hilker, K. Kleinlein, G. Salomon, I. Bloch, and C. Gross. *Microscopic Observation of Pauli Blocking in Degenerate Fermionic Lattice Gases*, Physical Review Letters **115.**, 263001 (Dec. 2015). DOI: [10.1103/PhysRevLett.115.263001](https://doi.org/10.1103/PhysRevLett.115.263001) (cit. on pp. 1, 20).
- [14] Parsons, M. F., F. Huber, A. Mazurenko, C. S. Chiu, W. Setiawan, K. Wooley-Brown, S. Blatt, and M. Greiner. *Site-Resolved Imaging of Fermionic Li 6 in an Optical Lattice*, Physical Review Letters **114.**, 213002 (May 2015). DOI: [10.1103/PhysRevLett.114.213002](https://doi.org/10.1103/PhysRevLett.114.213002) (cit. on p. 1).
- [15] Feynman, R. P. *Simulating physics with computers*, International Journal of Theoretical Physics **21.**, 467–488 (June 1982). DOI: [10.1007/BF02650179](https://doi.org/10.1007/BF02650179) (cit. on p. 1).
- [16] Nogrette, F., H. Labuhn, S. Ravets, D. Barredo, L. Béguin, A. Vernier, T. Lahaye, and A. Browaeys. *Single-Atom Trapping in Holographic 2D Arrays of Microtraps with Arbitrary Geometries*, Physical Review X **4.**, 021034 (May 2014). DOI: [10.1103/PhysRevX.4.021034](https://doi.org/10.1103/PhysRevX.4.021034) (cit. on pp. 1, 5, 35, 103).
- [17] Kim, H., W. Lee, H.-g. Lee, H. Jo, Y. Song, and J. Ahn. *In situ single-atom array synthesis using dynamic holographic optical tweezers*, Nature Communications **7.**, 13317 (Dec. 2016). DOI: [10.1038/ncomms13317](https://doi.org/10.1038/ncomms13317) (cit. on pp. 1, 5, 35).
- [18] Barredo, D., V. Lienhard, S. de Léséleuc, T. Lahaye, and A. Browaeys. *Synthetic three-dimensional atomic structures assembled atom by atom*, Nature **561.**, 79–82 (Sept. 2018). DOI: [10.1038/s41586-018-0450-2](https://doi.org/10.1038/s41586-018-0450-2) (cit. on pp. 1, 5, 35).
- [19] Endres, M., H. Bernien, A. Keesling, H. Levine, E. R. Anschuetz, A. Krajenbrink, C. Senko, V. Vuletic, M. Greiner, and M. D. Lukin. *Atom-by-atom assembly of defect-free one-dimensional cold atom arrays*, Science **354.**, 1024–1027 (2016). DOI: [10.1126/science.aah3752](https://doi.org/10.1126/science.aah3752) (cit. on pp. 2, 5, 35).
- [20] Barredo, D., S. de Léséleuc, V. Lienhard, T. Lahaye, and A. Browaeys. *An atom-by-atom assembler of defect-free arbitrary two-dimensional atomic arrays*, Science **354.**, 1021–1023 (Nov. 2016). DOI: [10.1126/science.aah3778](https://doi.org/10.1126/science.aah3778) (cit. on pp. 2, 5, 35).
- [21] Ohl de Mello, D., D. Schäffner, J. Werkmann, T. Preuschoff, L. Kohfahl, M. Schlosser, and G. Birkel. *Defect-Free Assembly of 2D Clusters of More Than 100 Single-Atom Quantum Systems*, Physical Review Letters **122.**, 203601 (May 2019). DOI: [10.1103/PhysRevLett.122.203601](https://doi.org/10.1103/PhysRevLett.122.203601) (cit. on pp. 2, 5, 35–37).
- [22] Kaufman, a. M., B. J. Lester, C. M. Reynolds, M. L. Wall, M. Foss-Feig, K. R. a. Hazzard, a. M. Rey, and C. a. Regal. *Two-particle quantum interference in tunnel-coupled optical tweezers*, Science **345.**, 306–309 (July 2014). DOI: [10.1126/science.1250057](https://doi.org/10.1126/science.1250057) (cit. on p. 2).

- [23] Murmann, S., A. Bergschneider, V. M. Klinkhamer, G. Zürn, T. Lompe, and S. Jochim. *Two Fermions in a Double Well: Exploring a Fundamental Building Block of the Hubbard Model*, *Physical Review Letters* **114.**, 080402 (Feb. 2015). DOI: [10.1103/PhysRevLett.114.080402](https://doi.org/10.1103/PhysRevLett.114.080402) (cit. on p. 2).
- [24] Lukin, M. D., M. Fleischhauer, R. Cote, L. M. Duan, D. Jaksch, J. I. Cirac, and P. Zoller. *Dipole Blockade and Quantum Information Processing in Mesoscopic Atomic Ensembles*, *Physical Review Letters* **87.**, 037901 (June 2001). DOI: [10.1103/PhysRevLett.87.037901](https://doi.org/10.1103/PhysRevLett.87.037901) (cit. on pp. 2, 89).
- [25] Urban, E., T. A. Johnson, T. Henage, L. Isenhower, D. D. Yavuz, T. G. Walker, and M. Saffman. *Observation of Rydberg blockade between two atoms*, *Nature Physics* **5.**, 110–114 (Feb. 2009). DOI: [10.1038/nphys1178](https://doi.org/10.1038/nphys1178) (cit. on pp. 2, 81, 89).
- [26] Gaëtan, A., Y. Miroshnychenko, T. Wilk, A. Chotia, M. Viteau, D. Comparat, P. Pillet, A. Browaeys, and P. Grangier. *Observation of Collective Excitation of Two Individual Atoms in the Rydberg Blockade Regime*, *Nature Physics* **5.**, 115–118 (Jan. 2009). DOI: [10/ctz867](https://doi.org/10/ctz867) (cit. on p. 2).
- [27] Wilk, T., A. Gaëtan, C. Evellin, J. Wolters, Y. Miroshnychenko, P. Grangier, and A. Browaeys. *Entanglement of Two Individual Neutral Atoms Using Rydberg Blockade*, *Physical Review Letters* **104.**, 010502 (Jan. 2010). DOI: [10.1103/PhysRevLett.104.010502](https://doi.org/10.1103/PhysRevLett.104.010502) (cit. on pp. 2, 89).
- [28] Saffman, M., T. G. Walker, and K. Mølmer. *Quantum information with Rydberg atoms*, *Reviews of Modern Physics* **82.**, 2313–2363 (Aug. 2010). DOI: [10.1103/RevModPhys.82.2313](https://doi.org/10.1103/RevModPhys.82.2313) (cit. on pp. 2, 5, 84, 89).
- [29] Lechner, W., P. Hauke, and P. Zoller. *A quantum annealing architecture with all-to-all connectivity from local interactions*, *Science Advances* **1.**, e1500838 (Oct. 2015). DOI: [10.1126/sciadv.1500838](https://doi.org/10.1126/sciadv.1500838) (cit. on pp. 2, 104).
- [30] Glaetzle, A. W., R. M. Van Bijnen, P. Zoller, and W. Lechner. *A coherent quantum annealer with Rydberg atoms*, *Nature Communications* **8.**, 1–6 (June 2017). DOI: [10.1038/ncomms15813](https://doi.org/10.1038/ncomms15813) (cit. on pp. 2, 10, 104).
- [31] Pichler, H., S.-t. Wang, L. Zhou, S. Choi, and M. D. Lukin. *Quantum Optimization for Maximum Independent Set Using Rydberg Atom Arrays*. Aug. 2018. URL: <http://arxiv.org/abs/1808.10816> (cit. on pp. 2, 104).
- [32] Saskin, S., J. T. Wilson, B. Grinkemeyer, and J. D. Thompson. *Narrow-Line Cooling and Imaging of Ytterbium Atoms in an Optical Tweezer Array*, *Physical Review Letters* **122.**, 143002 (Apr. 2019). DOI: [10.1103/PhysRevLett.122.143002](https://doi.org/10.1103/PhysRevLett.122.143002) (cit. on pp. 2, 5).
- [33] Graham, T. M., M. Kwon, B. Grinkemeyer, Z. Marra, X. Jiang, M. T. Lichtman, Y. Sun, M. Ebert, and M. Saffman. *Rydberg-Mediated Entanglement in a Two-Dimensional Neutral Atom Qubit Array*, *Physical Review Letters* **123.**, 230501 (Dec. 2019). DOI: [10.1103/PhysRevLett.123.230501](https://doi.org/10.1103/PhysRevLett.123.230501) (cit. on pp. 2, 84, 85, 89).

- [34] Levine, H. *et al.* *Parallel Implementation of High-Fidelity Multiqubit Gates with Neutral Atoms*, *Physical Review Letters* **123.**, 170503 (Oct. 2019). DOI: [10.1103/PhysRevLett.123.170503](https://doi.org/10.1103/PhysRevLett.123.170503) (cit. on pp. 2, 37, 53, 89).
- [35] Madjarov, I. S., J. P. Covey, A. L. Shaw, J. Choi, A. Kale, A. Cooper, H. Pichler, V. Schkolnik, J. R. Williams, and M. Endres. *High-fidelity entanglement and detection of alkaline-earth Rydberg atoms*, *Nature Physics* (May 2020). DOI: [10.1038/s41567-020-0903-z](https://doi.org/10.1038/s41567-020-0903-z) (cit. on pp. 2, 81, 83–85, 87, 102).
- [36] Bernien, H. *et al.* *Probing many-body dynamics on a 51-atom quantum simulator*, *Nature* **551.**, 579–584 (Nov. 2017). DOI: [10.1038/nature24622](https://doi.org/10.1038/nature24622) (cit. on pp. 2, 5).
- [37] Lienhard, V., S. de Léséleuc, D. Barredo, T. Lahaye, A. Browaeys, M. Schuler, L.-P. Henry, and A. M. Läuchli. *Observing the Space- and Time-Dependent Growth of Correlations in Dynamically Tuned Synthetic Ising Models with Antiferromagnetic Interactions*, *Physical Review X* **8.**, 021070 (June 2018). DOI: [10.1103/PhysRevX.8.021070](https://doi.org/10.1103/PhysRevX.8.021070) (cit. on p. 2).
- [38] Keesling, A. *et al.* *Quantum Kibble–Zurek mechanism and critical dynamics on a programmable Rydberg simulator*, *Nature* **568.**, 207–211 (Apr. 2019). DOI: [10.1038/s41586-019-1070-1](https://doi.org/10.1038/s41586-019-1070-1) (cit. on p. 2).
- [39] Léséleuc, S. de, V. Lienhard, P. Scholl, D. Barredo, S. Weber, N. Lang, H. P. Büchler, T. Lahaye, and A. Browaeys. *Observation of a symmetry-protected topological phase of interacting bosons with Rydberg atoms*, *Science* **365.**, 775–780 (Aug. 2019). DOI: [10.1126/science.aav9105](https://doi.org/10.1126/science.aav9105) (cit. on pp. 2, 5).
- [40] Jau, Y.-Y., A. M. Hankin, T. Keating, I. H. Deutsch, and G. W. Biedermann. *Entangling atomic spins with a Rydberg-dressed spin-flip blockade*, *Nature Physics* **12.**, 71–74 (Jan. 2016). DOI: [10.1038/nphys3487](https://doi.org/10.1038/nphys3487) (cit. on p. 2).
- [41] Zeiher, J., J.-y. Choi, A. Rubio-Abadal, T. Pohl, R. van Bijnen, I. Bloch, and C. Gross. *Coherent Many-Body Spin Dynamics in a Long-Range Interacting Ising Chain*, *Physical Review X* **7.**, 041063 (Dec. 2017). DOI: [10.1103/PhysRevX.7.041063](https://doi.org/10.1103/PhysRevX.7.041063) (cit. on pp. 2, 93, 99).
- [42] Zeiher, J., R. van Bijnen, P. Schauß, S. Hild, J.-y. Choi, T. Pohl, I. Bloch, and C. Gross. *Many-body interferometry of a Rydberg-dressed spin lattice*, *Nature Physics* **12.**, 1095–1099 (Dec. 2016). DOI: [10.1038/nphys3835](https://doi.org/10.1038/nphys3835) (cit. on pp. 2, 7, 93, 96, 98, 103).
- [43] Borish, V., O. Marković, J. A. Hines, S. V. Rajagopal, and M. Schleier-Smith. *Transverse-Field Ising Dynamics in a Rydberg-Dressed Atomic Gas*, *Physical Review Letters* **124.**, 063601 (Feb. 2020). DOI: [10.1103/PhysRevLett.124.063601](https://doi.org/10.1103/PhysRevLett.124.063601) (cit. on pp. 2, 5, 7, 93, 96, 103).
- [44] Glaetzle, A. W., M. Dalmonte, R. Nath, C. Gross, I. Bloch, and P. Zoller. *Designing Frustrated Quantum Magnets with Laser-Dressed Rydberg Atoms*, *Physical Review Letters* **114.**, 173002 (Apr. 2015). DOI: [10.1103/PhysRevLett.114.173002](https://doi.org/10.1103/PhysRevLett.114.173002) (cit. on pp. 2, 9, 10, 74, 104).

- [45] Schlosser, N., G. Reymond, I. Protsenko, and P. Grangier. *Sub-poissonian loading of single atoms in a microscopic dipole trap*, Nature **411.**, 1024–1027 (June 2001). DOI: [10.1038/35082512](https://doi.org/10.1038/35082512) (cit. on p. 5).
- [46] Schlosser, N., G. Reymond, and P. Grangier. *Collisional Blockade in Microscopic Optical Dipole Traps*, Physical Review Letters **89.**, 023005 (June 2002). DOI: [10.1103/PhysRevLett.89.023005](https://doi.org/10.1103/PhysRevLett.89.023005) (cit. on p. 5).
- [47] Grünzweig, T., A. Hilliard, M. McGovern, and M. F. Andersen. *Near-deterministic preparation of a single atom in an optical microtrap*, Nature Physics **6.**, 951–954 (Dec. 2010). DOI: [10.1038/nphys1778](https://doi.org/10.1038/nphys1778) (cit. on p. 5).
- [48] Lester, B. J., N. Luick, A. M. Kaufman, C. M. Reynolds, and C. A. Regal. *Rapid Production of Uniformly Filled Arrays of Neutral Atoms*, Physical Review Letters **115.**, 073003 (Aug. 2015). DOI: [10.1103/PhysRevLett.115.073003](https://doi.org/10.1103/PhysRevLett.115.073003) (cit. on p. 5).
- [49] Brown, M. O., T. Thiele, C. Kiehl, T.-W. Hsu, and C. A. Regal. *Gray-Molasses Optical-Tweezer Loading: Controlling Collisions for Scaling Atom-Array Assembly*, Physical Review X **9.**, 011057 (Mar. 2019). DOI: [10.1103/PhysRevX.9.011057](https://doi.org/10.1103/PhysRevX.9.011057) (cit. on p. 5).
- [50] Norcia, M. A., A. W. Young, W. J. Eckner, E. Oelker, J. Ye, and A. M. Kaufman. *Seconds-scale coherence on an optical clock transition in a tweezer array*, Science **366.**, 93–97 (Oct. 2019). DOI: [10.1126/science.aay0644](https://doi.org/10.1126/science.aay0644) (cit. on pp. 5, 35).
- [51] Stuart, D. and A. Kuhn. *Single-atom trapping and transport in DMD-controlled optical tweezers*, New Journal of Physics **20.**, 023013 (Feb. 2018). DOI: [10.1088/1367-2630/aaa634](https://doi.org/10.1088/1367-2630/aaa634) (cit. on pp. 5, 35).
- [52] Bluvstein, D. *et al.* *Controlling many-body dynamics with driven quantum scars in Rydberg atom arrays*. Dec. 2020. URL: <http://arxiv.org/abs/2012.12276> (cit. on pp. 5, 103).
- [53] Browaeys, A. and T. Lahaye. *Many-body physics with individually controlled Rydberg atoms*, Nature Physics **16.**, 132–142 (Feb. 2020). DOI: [10.1038/s41567-019-0733-z](https://doi.org/10.1038/s41567-019-0733-z) (cit. on p. 5).
- [54] Norcia, M. A., A. W. Young, and A. M. Kaufman. *Microscopic Control and Detection of Ultracold Strontium in Optical-Tweezer Arrays*, Physical Review X **8.**, 041054 (Dec. 2018). DOI: [10.1103/PhysRevX.8.041054](https://doi.org/10.1103/PhysRevX.8.041054) (cit. on pp. 5, 42).
- [55] Cooper, A., J. P. Covey, I. S. Madjarov, S. G. Porsev, M. S. Safronova, and M. Endres. *Alkaline-Earth Atoms in Optical Tweezers*, Physical Review X **8.**, 041055 (Dec. 2018). DOI: [10.1103/PhysRevX.8.041055](https://doi.org/10.1103/PhysRevX.8.041055) (cit. on p. 5).
- [56] Scholl, P. *et al.* *Programmable quantum simulation of 2D antiferromagnets with hundreds of Rydberg atoms*. Dec. 2020. URL: <http://arxiv.org/abs/2012.12268> (cit. on pp. 5, 73, 85, 89, 102).
- [57] Ebadi, S. *et al.* *Quantum Phases of Matter on a 256-Atom Programmable Quantum Simulator*. Dec. 2020. URL: <http://arxiv.org/abs/2012.12281> (cit. on pp. 5, 85, 89, 103).

- 
- [58] Bendkowsky, V., B. Butscher, J. Nipper, J. P. Shaffer, R. Löw, and T. Pfau. *Observation of ultralong-range Rydberg molecules*, *Nature* **458.**, 1005–1008 (Apr. 2009). DOI: [10.1038/nature07945](https://doi.org/10.1038/nature07945) (cit. on p. 5).
- [59] Niederprüm, T., O. Thomas, T. Eichert, C. Lippe, J. Pérez-Ríos, C. H. Greene, and H. Ott. *Observation of pendular butterfly Rydberg molecules*, *Nature Communications* **7.**, 12820 (Nov. 2016). DOI: [10.1038/ncomms12820](https://doi.org/10.1038/ncomms12820) (cit. on p. 5).
- [60] Kleinbach, K. S., F. Engel, T. Dieterle, R. Löw, T. Pfau, and F. Meinert. *Ionic Impurity in a Bose-Einstein Condensate at Submicrokelvin Temperatures*, *Physical Review Letters* **120.**, 193401 (May 2018). DOI: [10.1103/PhysRevLett.120.193401](https://doi.org/10.1103/PhysRevLett.120.193401) (cit. on p. 5).
- [61] Arias, A., G. Lochead, T. M. Wintermantel, S. Helmrich, and S. Whitlock. *Realization of a Rydberg-Dressed Ramsey Interferometer and Electrometer*, *Physical Review Letters* **122.**, 053601 (Feb. 2019). DOI: [10.1103/PhysRevLett.122.053601](https://doi.org/10.1103/PhysRevLett.122.053601) (cit. on p. 5).
- [62] Zeiher, J., P. Schauß, S. Hild, T. Macrì, I. Bloch, and C. Gross. *Microscopic Characterization of Scalable Coherent Rydberg Superatoms*, *Physical Review X* **5.**, 031015 (Aug. 2015). DOI: [10.1103/PhysRevX.5.031015](https://doi.org/10.1103/PhysRevX.5.031015) (cit. on pp. 5, 89).
- [63] Hollerith, S., J. Zeiher, J. Rui, A. Rubio-Abadal, V. Walther, T. Pohl, D. M. Stamper-Kurn, I. Bloch, and C. Gross. *Quantum gas microscopy of Rydberg macrodimers*, *Science* **364.**, 664–667 (May 2019). DOI: [10.1126/science.aaw4150](https://doi.org/10.1126/science.aaw4150) (cit. on pp. 5, 83).
- [64] Guardado-Sanchez, E., B. M. Spar, P. Schauss, R. Belyansky, J. T. Young, P. Bienias, A. V. Gorshkov, T. Iadecola, and W. S. Bakr. *Quench Dynamics of a Fermi Gas with Strong Long-Range Interactions*, 1–12 (Oct. 2020) (cit. on pp. 5, 7, 93, 96).
- [65] Feldker, T., P. Bacher, M. Stappel, D. Kolbe, R. Gerritsma, J. Walz, and F. Schmidt-Kaler. *Rydberg Excitation of a Single Trapped Ion*, *Physical Review Letters* **115.**, 173001 (Oct. 2015). DOI: [10.1103/PhysRevLett.115.173001](https://doi.org/10.1103/PhysRevLett.115.173001) (cit. on p. 5).
- [66] Kazimierczuk, T., D. Fröhlich, S. Scheel, H. Stolz, and M. Bayer. *Giant Rydberg excitons in the copper oxide Cu<sub>2</sub>O*, *Nature* **514.**, 343–347 (Oct. 2014). DOI: [10.1038/nature13832](https://doi.org/10.1038/nature13832) (cit. on p. 5).
- [67] Béguin, L., A. Vernier, R. Chicireanu, T. Lahaye, and A. Browaeys. *Direct Measurement of the van der Waals Interaction between Two Rydberg Atoms*, *Physical Review Letters* **110.**, 263201 (June 2013). DOI: [10.1103/PhysRevLett.110.263201](https://doi.org/10.1103/PhysRevLett.110.263201) (cit. on p. 6).
- [68] Ravets, S., H. Labuhn, D. Barredo, T. Lahaye, and A. Browaeys. *Measurement of the angular dependence of the dipole-dipole interaction between two individual Rydberg atoms at a Förster resonance*, *Physical Review A* **92.**, 020701 (Aug. 2015). DOI: [10.1103/PhysRevA.92.020701](https://doi.org/10.1103/PhysRevA.92.020701) (cit. on p. 6).

- [69] Gallagher, T. F. *Rydberg Atoms*. Cambridge Monographs on Atomic, Molecular and Chemical Physics. Cambridge University Press, 1994.  
DOI: [10.1017/CBO9780511524530](https://doi.org/10.1017/CBO9780511524530) (cit. on p. 6).
- [70] Adams, C. S. and N. Šibalić. *Rydberg Physics*. 2399-2891. IOP Publishing, 2018.  
DOI: [10.1088/978-0-7503-1635-4](https://doi.org/10.1088/978-0-7503-1635-4) (cit. on p. 6).
- [71] Šibalić, N., J. Pritchard, C. Adams, and K. Weatherill. *ARC: An open-source library for calculating properties of alkali Rydberg atoms*, Computer Physics Communications **220**, 319–331 (Nov. 2017). DOI: [10.1016/j.cpc.2017.06.015](https://doi.org/10.1016/j.cpc.2017.06.015) (cit. on pp. 7, 76, 83, 90, 96).
- [72] Ryabtsev, I. I., I. I. Beterov, D. B. Tretyakov, V. M. Entin, and E. A. Yakshina. *Doppler- and recoil-free laser excitation of Rydberg states via three-photon transitions*, Phys. Rev. A **84**, 053409 (Nov. 2011).  
DOI: [10.1103/PhysRevA.84.053409](https://doi.org/10.1103/PhysRevA.84.053409) (cit. on p. 7).
- [73] Arias, A., G. Lochead, T. M. Wintermantel, S. Helmrich, and S. Whitlock. *Realization of a Rydberg-Dressed Ramsey Interferometer and Electrometer*, Physical Review Letters **122.**, 53601 (2019). DOI: [10.1103/PhysRevLett.122.053601](https://doi.org/10.1103/PhysRevLett.122.053601) (cit. on pp. 7, 93).
- [74] Jau, Y.-Y., A. M. Hankin, T. Keating, I. H. Deutsch, and G. W. Biedermann. *Entangling atomic spins with a Rydberg-dressed spin-flip blockade*, Nature Physics **12.**, 71–74 (Jan. 2016). DOI: [10.1038/nphys3487](https://doi.org/10.1038/nphys3487) (cit. on pp. 7, 93, 94).
- [75] Landini, M., S. Roy, L. Carcagní, D. Trypogeorgos, M. Fattori, M. Inguscio, and G. Modugno. *Sub-Doppler laser cooling of potassium atoms*, Physical Review A **84.**, 043432 (Oct. 2011). DOI: [10.1103/PhysRevA.84.043432](https://doi.org/10.1103/PhysRevA.84.043432) (cit. on pp. 7, 13, 26, 27, 44).
- [76] Landini, M., S. Roy, G. Roati, A. Simoni, M. Inguscio, G. Modugno, and M. Fattori. *Direct evaporative cooling of  $^{39}\text{K}$  atoms to Bose-Einstein condensation*, Physical Review A **86.**, 033421 (Sept. 2012). DOI: [10.1103/PhysRevA.86.033421](https://doi.org/10.1103/PhysRevA.86.033421) (cit. on pp. 7, 13).
- [77] Salomon, G., L. Fouché, P. Wang, A. Aspect, P. Bouyer, and T. Bourdel. *Gray-molasses cooling of  $^{39}\text{K}$  to a high phase-space density*, EPL (Europhysics Letters) **104.**, 63002 (Jan. 2013). DOI: [10.1209/0295-5075/104/63002](https://doi.org/10.1209/0295-5075/104/63002) (cit. on pp. 7, 13, 26, 29).
- [78] Salomon, G., L. Fouché, S. Lepoutre, A. Aspect, and T. Bourdel. *All-optical cooling of  $^{39}\text{K}$  to Bose-Einstein condensation*, Physical Review A **90.**, 033405 (Sept. 2014). DOI: [10.1103/PhysRevA.90.033405](https://doi.org/10.1103/PhysRevA.90.033405) (cit. on pp. 7, 13).
- [79] Thompson, J. D., T. G. Tiecke, A. S. Zibrov, V. Vuletić, and M. D. Lukin. *Coherence and Raman Sideband Cooling of a Single Atom in an Optical Tweezer*, Physical Review Letters **110.**, 133001 (Mar. 2013).  
DOI: [10.1103/PhysRevLett.110.133001](https://doi.org/10.1103/PhysRevLett.110.133001) (cit. on pp. 8, 42).

- 
- [80] Schlosser, M., J. Kruse, and G. Birkl. *Synchronization of atomic quantum systems in multi-site optical trapping potentials*. Feb. 2019. URL: <http://arxiv.org/abs/1902.00370> (cit. on p. 8).
- [81] Hutzler, N. R., L. R. Liu, Y. Yu, and K.-K. Ni. *Eliminating light shifts for single atom trapping*, New Journal of Physics **19.**, 023007 (Feb. 2017). DOI: [10.1088/1367-2630/aa5a3b](https://doi.org/10.1088/1367-2630/aa5a3b) (cit. on pp. 10, 33, 44).
- [82] Gil, L. I. R., R. Mukherjee, E. M. Bridge, M. P. A. Jones, and T. Pohl. *Spin Squeezing in a Rydberg Lattice Clock*, Physical Review Letters **112.**, 103601 (Mar. 2014). DOI: [10.1103/PhysRevLett.112.103601](https://doi.org/10.1103/PhysRevLett.112.103601) (cit. on p. 10).
- [83] Glaetzle, A. W., M. Dalmonte, R. Nath, I. Rousochatzakis, R. Moessner, and P. Zoller. *Quantum Spin-Ice and Dimer Models with Rydberg Atoms*, Physical Review X **4.**, 041037 (Nov. 2014). DOI: [10.1103/PhysRevX.4.041037](https://doi.org/10.1103/PhysRevX.4.041037) (cit. on p. 10).
- [84] Macrì, T., A. Smerzi, and L. Pezzè. *Loschmidt Echo for Quantum Metrology*, Physical Review A **94.**, 010102 (July 2016). DOI: [10/gddjs4](https://doi.org/10/gddjs4) (cit. on p. 10).
- [85] Swingle, B., G. Bentsen, M. Schleier-Smith, and P. Hayden. *Measuring the Scrambling of Quantum Information*, Physical Review A **94.**, 040302 (Oct. 2016). DOI: [10/ggm8wj](https://doi.org/10/ggm8wj) (cit. on p. 10).
- [86] Potirniche, I.-D., A. Potter, M. Schleier-Smith, A. Vishwanath, and N. Yao. *Floquet Symmetry-Protected Topological Phases in Cold-Atom Systems*, Physical Review Letters **119.**, 123601 (Sept. 2017). DOI: [10/gcpcsf](https://doi.org/10/gcpcsf) (cit. on p. 10).
- [87] Dalmonte, M., B. Vermersch, and P. Zoller. *Quantum Simulation and Spectroscopy of Entanglement Hamiltonians*, Nature Physics **14.**, 827–831 (May 2018). DOI: [10/gdjb8g](https://doi.org/10/gdjb8g) (cit. on p. 10).
- [88] Elben, A., B. Vermersch, M. Dalmonte, J. Cirac, and P. Zoller. *Rényi Entropies from Random Quenches in Atomic Hubbard and Spin Models*, Physical Review Letters **120.**, 050406 (Feb. 2018). DOI: [10/gddjft](https://doi.org/10/gddjft) (cit. on p. 10).
- [89] Kaubruegger, R., P. Silvi, C. Kokail, R. van Bijnen, A. M. Rey, J. Ye, A. M. Kaufman, and P. Zoller. *Variational Spin-Squeezing Algorithms on Programmable Quantum Sensors*, Physical Review Letters **123.**, 260505 (Dec. 2019). DOI: [10.1103/PhysRevLett.123.260505](https://doi.org/10.1103/PhysRevLett.123.260505) (cit. on p. 10).
- [90] Cohen-Tannoudji, C., J. Dupont-Roc, G. Grynberg, and P. Thickstun. *Atom-Photon Interactions: Basic Processes and Applications*. A Wiley-Interscience publication. Wiley, 1992 (cit. on p. 13).
- [91] Metcalf, H. and P. van der Straten. *Laser Cooling and Trapping*. Graduate Texts in Contemporary Physics. Springer New York, 2012 (cit. on p. 13).
- [92] Foot, C. *Atomic Physics*. Oxford Master Series in Physics. OUP Oxford, 2005 (cit. on pp. 13, 87).
- [93] Landini, M. “A tunable Bose-Einstein condensate for quantum interferometry.” PhD thesis. Università degli Studi di Trento, 2011 (cit. on pp. 13, 22).

- [94] Duda, M. “A Laser System for Cooling and Trapping Potassium-39.” MA thesis. LMU Munich, 2017 (cit. on pp. 13, 15).
- [95] Wu, C.-H. “Strongly Interacting Quantum Mixtures of Ultracold Atoms.” PhD thesis. MIT, 2013 (cit. on pp. 14, 15).
- [96] Omran, A. “A Microscope for Fermi Gases.” PhD thesis. LMU Munich, 2016 (cit. on p. 15).
- [97] Hofmann, C. S., G. Günter, H. Schempp, N. L. M. Müller, A. Faber, H. Busche, M. Robert-de-Saint-Vincent, S. Whitlock, and M. Weidemüller. *An experimental approach for investigating many-body phenomena in Rydberg-interacting quantum systems*, *Frontiers of Physics* **9.**, 571–586 (Oct. 2014). DOI: [10.1007/s11467-013-0396-7](https://doi.org/10.1007/s11467-013-0396-7) (cit. on pp. 17, 20).
- [98] Klocke, K., T. M. Wintermantel, G. Lochead, S. Whitlock, and M. Buchhold. *Hydrodynamic stabilization of self-organized criticality in a driven Rydberg gas*. Sept. 2020. URL: <http://arxiv.org/abs/2009.11908> (cit. on p. 17).
- [99] Cantat-Moltrecht, T., R. Cortiñas, B. Ravon, P. Méhaignerie, S. Haroche, J. M. Raimond, M. Favier, M. Brune, and C. Sayrin. *Long-lived circular Rydberg states of laser-cooled rubidium atoms in a cryostat*, *Physical Review Research* **2.**, 022032 (May 2020). DOI: [10.1103/PhysRevResearch.2.022032](https://doi.org/10.1103/PhysRevResearch.2.022032) (cit. on p. 17).
- [100] Béguin, L. “Measurement of the van der Waals interaction between two Rydberg atoms.” PhD thesis. Institut d’Optique, 2013 (cit. on pp. 17, 36, 37, 49).
- [101] Gantner, T. “Magnetic Trapping of Lithium-6 and Diploma thesis of.” MA thesis. TU Munich, 2012 (cit. on p. 18).
- [102] Koepsell, J., S. Hirthe, D. Bourgund, P. Sompet, J. Vijayan, G. Salomon, C. Gross, and I. Bloch. *Robust Bilayer Charge-Pumping for Spin- and Density-Resolved Quantum Gas Microscopy*. Feb. 2020. URL: <http://arxiv.org/abs/2002.07577> (cit. on p. 20).
- [103] Baillard, X., A. Gauguier, S. Bize, P. Lemonde, P. Laurent, A. Clairon, and P. Rosenbusch. *Interference-filter-stabilized external-cavity diode lasers*, *Optics Communications* **266.**, 609–613 (Oct. 2006). DOI: [10.1016/j.optcom.2006.05.011](https://doi.org/10.1016/j.optcom.2006.05.011) (cit. on pp. 21, 95, 97).
- [104] Camy, G., C. Bordé, and M. Ducloy. *Heterodyne saturation spectroscopy through frequency modulation of the saturating beam*, *Optics Communications* **41.**, 325–330 (May 1982). DOI: [10.1016/0030-4018\(82\)90406-0](https://doi.org/10.1016/0030-4018(82)90406-0) (cit. on p. 22).
- [105] Festa, L. “PhD thesis, To be published.” PhD thesis. LMU Munich (cit. on pp. 31, 35).
- [106] Eberhard, R. “Preparing next generation tweezer systems for quantum simulation of spin models.” MA thesis. LMU Munich, 2020 (cit. on pp. 33, 35, 99, 104).
- [107] Weitenberg, C. “Single-Atom resolved imaging and manipulation of an atomic Mott insulator.” PhD thesis. LMU Munich, 2011, pp. 1–120 (cit. on p. 35).

- [108] Kaufman, A. M. “Laser-cooling atoms to indistinguishability : Atomic Hong-Ou-Mandel interference and entanglement through spin exchange.” PhD thesis. University of Colorado, 2015 (cit. on pp. 35–38).
- [109] Osterholz, P. “Freely Configurable Holographic Trap Arrays for the Trapping of Single Atoms.” MA thesis. LMU Munich, 2020 (cit. on p. 35).
- [110] Kim, D., A. Keesling, A. Omran, H. Levine, H. Bernien, M. Greiner, M. D. Lukin, and D. R. Englund. *Large-scale uniform optical focus array generation with a phase spatial light modulator*, *Optics Letters* **44.**, 3178 (June 2019). DOI: [10.1364/OL.44.003178](https://doi.org/10.1364/OL.44.003178) (cit. on p. 35).
- [111] De Léséleuc, S., D. Barredo, V. Lienhard, A. Browaeys, and T. Lahaye. *Analysis of imperfections in the coherent optical excitation of single atoms to Rydberg states*, *Physical Review A* **97.**, 053803 (May 2018). DOI: [10.1103/PhysRevA.97.053803](https://doi.org/10.1103/PhysRevA.97.053803) (cit. on pp. 36, 37, 41, 46, 73, 83–85, 89).
- [112] Makrides, C., D. S. Barker, J. A. Fedchak, J. Scherschligt, S. Eckel, and E. Tiesinga. *Elastic rate coefficients for  $Li + H_2$  collisions in the calibration of a cold-atom vacuum standard*, *Physical Review A* **99.**, 042704 (Apr. 2019). DOI: [10.1103/PhysRevA.99.042704](https://doi.org/10.1103/PhysRevA.99.042704) (cit. on p. 36).
- [113] Rui, J., D. Wei, A. Rubio-Abadal, S. Hollerith, J. Zeiher, D. M. Stamper-Kurn, C. Gross, and I. Bloch. *A subradiant optical mirror formed by a single structured atomic layer*, *Nature* **583.**, 369–374 (July 2020). DOI: [10.1038/s41586-020-2463-x](https://doi.org/10.1038/s41586-020-2463-x) (cit. on p. 36).
- [114] Beijerinck, H. C. W. *Rigorous calculation of heating in alkali-metal traps by background gas collisions*, *Physical Review A* **61.**, 033606 (Feb. 2000). DOI: [10.1103/PhysRevA.61.033606](https://doi.org/10.1103/PhysRevA.61.033606) (cit. on p. 36).
- [115] Wang, Y., K. Wang, E. F. Fenton, Y.-W. Lin, K.-K. Ni, and J. D. Hood. *Reduction of laser intensity noise over 1 MHz band for single atom trapping*, *Optics Express* **28.**, 31209 (Oct. 2020). DOI: [10.1364/OE.405002](https://doi.org/10.1364/OE.405002) (cit. on p. 37).
- [116] Savard, T. A., K. M. O’Hara, and J. E. Thomas. *Laser-noise-induced heating in far-off resonance optical traps*, *Physical Review A* **56.**, R1095–R1098 (Aug. 1997). DOI: [10.1103/PhysRevA.56.R1095](https://doi.org/10.1103/PhysRevA.56.R1095) (cit. on p. 37).
- [117] Gehm, M. E., K. M. O’Hara, T. A. Savard, and J. E. Thomas. *Dynamics of noise-induced heating in atom traps*, *Physical Review A* **58.**, 3914–3921 (Nov. 1998). DOI: [10.1103/PhysRevA.58.3914](https://doi.org/10.1103/PhysRevA.58.3914) (cit. on p. 37).
- [118] Farré, A., M. Shayegan, C. López-Quesada, G. A. Blab, M. Montes-Usategui, N. R. Forde, and E. Martín-Badosa. *Positional stability of holographic optical traps*, *Optics Express* **19.**, 21370 (Oct. 2011). DOI: [10.1364/OE.19.021370](https://doi.org/10.1364/OE.19.021370) (cit. on p. 37).
- [119] Walker, T. G. and M. Saffman. *Entanglement of Two Atoms Using Rydberg Blockade*, *Advances in Atomic, Molecular and Optical Physics*. Vol. 61. November 2018. 2012, pp. 81–115. DOI: [10.1016/B978-0-12-396482-3.00002-8](https://doi.org/10.1016/B978-0-12-396482-3.00002-8) (cit. on pp. 38, 39).

- [120] Tuchendler, C., A. M. Lance, A. Browaeys, Y. R. P. Sortais, and P. Grangier. *Energy distribution and cooling of a single atom in an optical tweezer*, Physical Review A **78.**, 033425 (Sept. 2008). doi: [10.1103/PhysRevA.78.033425](https://doi.org/10.1103/PhysRevA.78.033425) (cit. on pp. 41, 46, 47, 49, 78).
- [121] Monroe, C., D. M. Meekhof, B. E. King, S. R. Jefferts, W. M. Itano, D. J. Wineland, and P. Gould. *Resolved-Sideband Raman Cooling of a Bound Atom to the 3D Zero-Point Energy*, Physical Review Letters **75.**, 4011–4014 (Nov. 1995). doi: [10.1103/PhysRevLett.75.4011](https://doi.org/10.1103/PhysRevLett.75.4011) (cit. on pp. 41, 44).
- [122] Hamann, S. E., D. L. Haycock, G. Klose, P. H. Pax, I. H. Deutsch, and P. S. Jessen. *Resolved-Sideband Raman Cooling to the Ground State of an Optical Lattice*, Physical Review Letters **80.**, 4149–4152 (1998). doi: [10.1103/PhysRevLett.80.4149](https://doi.org/10.1103/PhysRevLett.80.4149) (cit. on p. 41).
- [123] Kerman, A., V. Vuletić, C. Chin, and S. Chu. *Beyond Optical Molasses: 3D Raman Sideband Cooling of Atomic Cesium to High Phase-Space Density*, Physical Review Letters **84.**, 439–442 (Jan. 2000). doi: [10/chc63w](https://doi.org/10.1103/PhysRevLett.84.439) (cit. on p. 41).
- [124] Kaufman, A. M., B. J. Lester, and C. A. Regal. *Cooling a Single Atom in an Optical Tweezer to Its Quantum Ground State*, Physical Review X **2.**, 041014 (Nov. 2012). doi: [10.1103/PhysRevX.2.041014](https://doi.org/10.1103/PhysRevX.2.041014) (cit. on pp. 42, 45).
- [125] Lester, B. J., A. M. Kaufman, and C. A. Regal. *Raman cooling imaging: Detecting single atoms near their ground state of motion*, Physical Review A **90.**, 011804 (July 2014). doi: [10.1103/PhysRevA.90.011804](https://doi.org/10.1103/PhysRevA.90.011804) (cit. on p. 42).
- [126] Yu, Y., N. R. Hutzler, J. T. Zhang, L. R. Liu, J. D. Hood, T. Rosenband, and K.-K. Ni. *Motional-ground-state cooling outside the Lamb-Dicke regime*, Physical Review A **97.**, 063423 (June 2018). doi: [10.1103/PhysRevA.97.063423](https://doi.org/10.1103/PhysRevA.97.063423) (cit. on pp. 42, 44, 45, 84).
- [127] Young, A. W., W. J. Eckner, W. R. Milner, D. Kedar, M. A. Norcia, E. Oelker, N. Schine, J. Ye, and A. M. Kaufman. *A tweezer clock with half-minute atomic coherence at optical frequencies and high relative stability*. Apr. 2020. URL: [http://arxiv.org/abs/2004.06095](https://arxiv.org/abs/2004.06095) (cit. on pp. 47, 103).
- [128] Ohl de Mello, D. “Rydberg interactions in a defect-free array of single-atom quantum systems.” PhD thesis. TU Darmstadt, 2020 (cit. on pp. 49, 84, 86).
- [129] Cabrera, C. R. “Quantum liquid droplets in a mixture of Bose-Einstein condensates.” PhD thesis. ICFO, 2018 (cit. on p. 50).
- [130] Souza, A. M., G. a. Álvarez, and D. Suter. *Robust dynamical decoupling.*, Philosophical transactions of the royal society. Series A **370.**, 4748–4769 (Oct. 2012). doi: [10.1098/rsta.2011.0355](https://doi.org/10.1098/rsta.2011.0355) (cit. on p. 53).
- [131] Schlosser, M. “Bereitstellung und kohärente Kontrolle von Einzel-Atom-Quantensystemen in zweidimensionalen Quantenregistern.” PhD thesis. TU Darmstadt, 2013 (cit. on p. 53).

- [132] Merkel, B., K. Thirumalai, J. E. Tarlton, V. M. Schäfer, C. J. Ballance, T. P. Harty, and D. M. Lucas. *Magnetic field stabilization system for atomic physics experiments*, Review of Scientific Instruments **90.**, 044702 (Apr. 2019). DOI: [10.1063/1.5080093](https://doi.org/10.1063/1.5080093) (cit. on p. 53).
- [133] Alnis, J., A. Matveev, N. Kolachevsky, T. Udem, and T. W. Hänsch. *Subhertz linewidth diode lasers by stabilization to vibrationally and thermally compensated ultralow-expansion glass Fabry-Pérot cavities*, Physical Review A **77.**, 053809 (May 2008). DOI: [10.1103/PhysRevA.77.053809](https://doi.org/10.1103/PhysRevA.77.053809) (cit. on pp. 57–59, 61, 72).
- [134] Matveev, A. N., N. N. Kolachevsky, J. Alnis, and T. W. Hänsch. *Semiconductor laser with the subhertz linewidth*, Quantum Electronics **38.**, 895–902 (Oct. 2008). DOI: [10.1070/QE2008v038n10ABEH013806](https://doi.org/10.1070/QE2008v038n10ABEH013806) (cit. on pp. 57, 72).
- [135] Matveev, A. N., N. N. Kolachevsky, J. Alnis, and T. W. Hänsch. *Spectral parameters of reference-cavity-stabilised lasers*, Quantum Electronics **38.**, 391–400 (Apr. 2008). DOI: [10.1070/QE2008v038n04ABEH013680](https://doi.org/10.1070/QE2008v038n04ABEH013680) (cit. on pp. 57, 72, 73).
- [136] Drever, R. W. P., J. L. Hall, F. V. Kowalski, J. Hough, G. M. Ford, A. J. Munley, and H. Ward. *Laser phase and frequency stabilization using an optical resonator*, Applied Physics B Photophysics and Laser Chemistry **31.**, 97–105 (June 1983). DOI: [10.1007/BF00702605](https://doi.org/10.1007/BF00702605) (cit. on pp. 59, 69).
- [137] Bai, J., J. Wang, J. He, and J. Wang. *Electronic sideband locking of a broadly tunable 318.6 nm ultraviolet laser to an ultra-stable optical cavity*, Journal of Optics **19.**, 045501 (Apr. 2017). DOI: [10.1088/2040-8986/aa5a8c](https://doi.org/10.1088/2040-8986/aa5a8c) (cit. on p. 59).
- [138] Zeiher, J. “Realization of Rydberg-dressed quantum magnets.” PhD thesis. LMU Munich, 2017 (cit. on pp. 60, 83, 93, 94, 97, 98).
- [139] Walter, A.-S. “Design and Characterization of an UV-Lasersystem for Rydberg Experiments with Potassium.” MA thesis. TU Munich, 2018 (cit. on pp. 61, 67).
- [140] Boyd, R. W. *Nonlinear Optics, Third Edition*. 3rd. USA: Academic Press, Inc., 2008 (cit. on pp. 61, 62).
- [141] Boyd, G. D. and D. A. Kleinman. *Parametric Interaction of Focused Gaussian Light Beams*, Journal of Applied Physics **39.**, 3597–3639 (July 1968). DOI: [10.1063/1.1656831](https://doi.org/10.1063/1.1656831) (cit. on p. 63).
- [142] Kondo, K., M. Oka, H. Wada, T. Fukui, N. Umezū, K. Tatsuki, and S. Kubota. *Demonstration of long-term reliability of a 266-nm, continuous-wave, frequency-quadrupled solid-state laser using  $\beta$ -BaB<sub>2</sub>O<sub>4</sub>*, Optics Letters **23.**, 195–197 (Feb. 1998). DOI: [10.1364/OL.23.000195](https://doi.org/10.1364/OL.23.000195) (cit. on p. 63).
- [143] Sakuma, J., Y. Asakawa, and M. Obara. *Generation of 5-W deep-UV continuous-wave radiation at 266 nm by an external cavity with a CsLiB<sub>6</sub>O<sub>10</sub> crystal*, Optics Letters **29.**, 92 (Jan. 2004). DOI: [10.1364/OL.29.000092](https://doi.org/10.1364/OL.29.000092) (cit. on p. 63).

- [144] Sudmeyer, T., Y. Imai, H. Masuda, N. Eguchi, M. Saito, and S. Kubota. *Efficient 2<sup>nd</sup> and 4<sup>th</sup> harmonic generation of a single-frequency, continuous-wave fiber amplifier*, Optics Express **16.**, 1546 (Feb. 2008). doi: [10.1364/OE.16.001546](https://doi.org/10.1364/OE.16.001546) (cit. on p. 63).
- [145] Burkley, Z., C. Razor, S. F. Cooper, A. D. Brandt, and D. C. Yost. *Yb fiber amplifier at 972.5 nm with frequency quadrupling to 243.1 nm*, Applied Physics B **123.**, 5 (Jan. 2017). doi: [10.1007/s00340-016-6583-9](https://doi.org/10.1007/s00340-016-6583-9) (cit. on pp. 63, 64).
- [146] Sakuma, J., K. Moriizumi, and H. Kusunose. *True CW 1934-nm light generation based on frequency conversion of fiber amplifiers*, Optics Express **19.**, 15020 (Aug. 2011). doi: [10.1364/OE.19.015020](https://doi.org/10.1364/OE.19.015020) (cit. on p. 64).
- [147] Smith, A. *Crystal Nonlinear Optics: With SNLO Examples*. Albuquerque, NM, USA: AS-Photonics, 2015, p. 726 (cit. on p. 64).
- [148] Meier, T., B. Willke, and K. Danzmann. *Continuous-wave single-frequency 532 nm laser source emitting 130 W into the fundamental transversal mode*, Optics Letters **35.**, 3742 (Nov. 2010). doi: [10.1364/OL.35.003742](https://doi.org/10.1364/OL.35.003742) (cit. on p. 66).
- [149] Hannig, S., J. Mielke, J. A. Fenske, M. Misera, N. Beev, C. Ospelkaus, and P. O. Schmidt. *A highly stable monolithic enhancement cavity for second harmonic generation in the ultraviolet*, Review of Scientific Instruments **89.**, 013106 (Jan. 2018). doi: [10.1063/1.5005515](https://doi.org/10.1063/1.5005515) (cit. on pp. 67, 70).
- [150] Cooper, S. F., Z. Burkley, A. D. Brandt, C. Razor, and D. C. Yost. *Cavity enhanced DUV laser for two-photon cooling of atomic hydrogen*. Jan. 2018. URL: <http://arxiv.org/abs/1801.08536> (cit. on p. 67).
- [151] Briles, T. C., D. C. Yost, A. Cingöz, J. Ye, and T. R. Schibli. *Simple piezoelectric-actuated mirror with 180 kHz servo bandwidth*, Optics Express **18.**, 9739 (May 2010). doi: [10.1364/OE.18.009739](https://doi.org/10.1364/OE.18.009739) (cit. on p. 68).
- [152] Hansch, T. and B. Couillaud. *Laser frequency stabilization by polarization spectroscopy of a reflecting reference cavity*, Optics Communications **35.**, 441–444 (Dec. 1980). doi: [10.1016/0030-4018\(80\)90069-3](https://doi.org/10.1016/0030-4018(80)90069-3) (cit. on p. 69).
- [153] Preuschoff, T., M. Schlosser, and G. Birkl. *Digital laser frequency and intensity stabilization based on the STEMLab platform (originally Red Pitaya)*, Review of Scientific Instruments **91.**, 083001 (Aug. 2020). doi: [10.1063/5.0009524](https://doi.org/10.1063/5.0009524) (cit. on p. 70).
- [154] Alnis, J., A. Matveev, N. Kolachevsky, T. Wilken, R. Holzwarth, and T. W. Hänsch. *Stable diode lasers for hydrogen precision spectroscopy*, The European Physical Journal Special Topics **163.**, 89–94 (Oct. 2008). doi: [10.1140/epjst/e2008-00811-y](https://doi.org/10.1140/epjst/e2008-00811-y) (cit. on p. 72).

- 
- [155] Levine, H., A. Keesling, A. Omran, H. Bernien, S. Schwartz, A. S. Zibrov, M. Endres, M. Greiner, V. Vuletić, and M. D. Lukin. *High-Fidelity Control and Entanglement of Rydberg-Atom Qubits*, Physical Review Letters **121.**, 123603 (Sept. 2018). DOI: [10.1103/PhysRevLett.121.123603](https://doi.org/10.1103/PhysRevLett.121.123603) (cit. on pp. 73, 81, 84, 85, 89, 102).
- [156] Kolachevsky, N., J. Alnis, C. G. Parthey, A. Matveev, R. Landig, and T. W. Hänsch. *Low phase noise diode laser oscillator for 1S–2S spectroscopy in atomic hydrogen*, Optics Letters **36.**, 4299 (Nov. 2011). DOI: [10.1364/OL.36.004299](https://doi.org/10.1364/OL.36.004299) (cit. on p. 73).
- [157] Burkley, Z. N. “High-Power Deep-UV Laser for Improved and Novel Experiments on Hydrogen.” PhD thesis. Colorado State University, 2019 (cit. on p. 75).
- [158] Robertson, E. J., N. Šibalić, R. M. Potvliege, and M. P. A. Jones. *ARC 3.0: An expanded Python toolbox for atomic physics calculations*. July 2020. URL: <http://arxiv.org/abs/2007.12016> (cit. on p. 76).
- [159] Isenhower, L., E. Urban, X. L. Zhang, A. T. Gill, T. Henage, T. A. Johnson, T. G. Walker, and M. Saffman. *Demonstration of a Neutral Atom Controlled-NOT Quantum Gate*, Physical Review Letters **104.**, 010503 (Jan. 2010). DOI: [10.1103/PhysRevLett.104.010503](https://doi.org/10.1103/PhysRevLett.104.010503) (cit. on pp. 81, 89).
- [160] De Léséleuc, S. “Quantum simulation of spin models with assembled arrays of Rydberg atoms.” PhD thesis. Institut d’Optique, 2018 (cit. on p. 84).
- [161] Schlosser, M., D. Ohl de Mello, D. Schäffner, T. Preuschoff, L. Kohfahl, and G. Birkl. *Assembled arrays of Rydberg-interacting atoms*, Journal of Physics B: Atomic, Molecular and Optical Physics **53.**, 144001 (July 2020). DOI: [10.1088/1361-6455/ab8b46](https://doi.org/10.1088/1361-6455/ab8b46) (cit. on p. 84).
- [162] Younge, K. C., B. Knuffman, S. E. Anderson, and G. Raithel. *State-Dependent Energy Shifts of Rydberg Atoms in a Ponderomotive Optical Lattice*, Physical Review Letters **104.**, 173001 (Apr. 2010). DOI: [10.1103/PhysRevLett.104.173001](https://doi.org/10.1103/PhysRevLett.104.173001) (cit. on p. 84).
- [163] Barredo, D., V. Lienhard, P. Scholl, S. de Léséleuc, T. Boulier, A. Browaeys, and T. Lahaye. *Three-Dimensional Trapping of Individual Rydberg Atoms in Ponderomotive Bottle Beam Traps*, Physical Review Letters **124.**, 023201 (Jan. 2020). DOI: [10.1103/PhysRevLett.124.023201](https://doi.org/10.1103/PhysRevLett.124.023201) (cit. on pp. 84, 103).
- [164] Omran, A. *et al.* *Generation and manipulation of Schrödinger cat states in Rydberg atom arrays*, Science **365.**, 570–574 (Aug. 2019). DOI: [10.1126/science.aax9743](https://doi.org/10.1126/science.aax9743) (cit. on pp. 85, 89).
- [165] Johansson, J., P. Nation, and F. Nori. *QuTiP: An open-source Python framework for the dynamics of open quantum systems*, Computer Physics Communications **183.**, 1760–1772 (Aug. 2012). DOI: [10.1016/j.cpc.2012.02.021](https://doi.org/10.1016/j.cpc.2012.02.021) (cit. on p. 87).
- [166] Johansson, J., P. Nation, and F. Nori. *QuTiP 2: A Python framework for the dynamics of open quantum systems*, Computer Physics Communications **184.**, 1234–1240 (Apr. 2013). DOI: [10.1016/j.cpc.2012.11.019](https://doi.org/10.1016/j.cpc.2012.11.019) (cit. on p. 87).

- [167] Weber, S., C. Tresp, H. Menke, A. Urvoy, O. Firstenberg, H. P. Büchler, and S. Hofferberth. *Tutorial: Calculation of Rydberg interaction potentials*, J. Phys. B: At. Mol. Opt. Phys. **50.**, 133001 (June 2017). doi: [10.1088/1361-6455/aa743a](https://doi.org/10.1088/1361-6455/aa743a) (cit. on pp. 91, 92).
- [168] Schauss, P., J. Zeiher, T. Fukuhara, S. Hild, M. Cheneau, T. Macri, T. Pohl, I. Bloch, and C. Gross. *Crystallization in Ising quantum magnets*, Science **347.**, 1455–1458 (Mar. 2015). doi: [10.1126/science.1258351](https://doi.org/10.1126/science.1258351) (cit. on p. 89).
- [169] Hankin, A. M., Y. Y. Jau, L. P. Parazzoli, C. W. Chou, D. J. Armstrong, A. J. Landahl, and G. W. Biedermann. *Two-atom Rydberg blockade using direct  $6S$  to  $nP$  excitation*, Physical Review A - Atomic, Molecular, and Optical Physics **89.** (Mar. 2014). doi: [10.1103/PhysRevA.89.033416](https://doi.org/10.1103/PhysRevA.89.033416) (cit. on p. 89).
- [170] Barredo, D., S. Ravets, H. Labuhn, L. Béguin, A. Vernier, F. Nogrette, T. Lahaye, and A. Browaeys. *Demonstration of a Strong Rydberg Blockade in Three-Atom Systems with Anisotropic Interactions*, Physical Review Letters **112.**, 183002 (May 2014). doi: [10.1103/PhysRevLett.112.183002](https://doi.org/10.1103/PhysRevLett.112.183002) (cit. on p. 89).
- [171] Ebert, M., M. Kwon, T. G. Walker, and M. Saffman. *Coherence and Rydberg Blockade of Atomic Ensemble Qubits*, Physical Review Letters **115.**, 093601 (Aug. 2015). doi: [10.1103/PhysRevLett.115.093601](https://doi.org/10.1103/PhysRevLett.115.093601) (cit. on p. 89).
- [172] Schauß, P., M. Cheneau, M. Endres, T. Fukuhara, S. Hild, A. Omran, T. Pohl, C. Gross, S. Kuhr, and I. Bloch. *Observation of spatially ordered structures in a two-dimensional Rydberg gas*, Nature **491.**, 87–91 (Nov. 2012). doi: [10.1038/nature11596](https://doi.org/10.1038/nature11596) (cit. on p. 89).
- [173] Dicke, R. H. *Coherence in Spontaneous Radiation Processes*, Physical Review **93.**, 99–110 (Jan. 1954). doi: [10.1103/PhysRev.93.99](https://doi.org/10.1103/PhysRev.93.99) (cit. on p. 89).
- [174] Dudin, Y. O., L. Li, F. Bariani, and A. Kuzmich. *Observation of coherent many-body Rabi oscillations*, Nature Physics **8.**, 790–794 (Nov. 2012). doi: [10.1038/nphys2413](https://doi.org/10.1038/nphys2413) (cit. on p. 89).
- [175] Haas, F., J. Volz, R. Gehr, J. Reichel, and J. Esteve. *Entangled States of More Than 40 Atoms in an Optical Fiber Cavity*, Science **344.**, 180–183 (Apr. 2014). doi: [10.1126/science.1248905](https://doi.org/10.1126/science.1248905) (cit. on p. 89).
- [176] Guardado-Sanchez, E., P. T. Brown, D. Mitra, T. Devakul, D. A. Huse, P. Schauß, and W. S. Bakr. *Probing the Quench Dynamics of Antiferromagnetic Correlations in a 2D Quantum Ising Spin System*, Physical Review X **8.**, 021069 (June 2018). doi: [10.1103/PhysRevX.8.021069](https://doi.org/10.1103/PhysRevX.8.021069) (cit. on p. 93).
- [177] Zeiher, J., J.-y. Choi, A. Rubio-Abadal, T. Pohl, R. van Bijnen, I. Bloch, and C. Gross. *Coherent Many-Body Spin Dynamics in a Long-Range Interacting Ising Chain*, Physical Review X **7.**, 041063 (Dec. 2017). doi: [10.1103/PhysRevX.7.041063](https://doi.org/10.1103/PhysRevX.7.041063) (cit. on pp. 93, 96).

- [178] Henkel, N., R. Nath, and T. Pohl. *Three-Dimensional Roton Excitations and Supersolid Formation in Rydberg-Excited Bose-Einstein Condensates*, Physical Review Letters **104.**, 195302 (May 2010). DOI: [10.1103/PhysRevLett.104.195302](https://doi.org/10.1103/PhysRevLett.104.195302) (cit. on p. 93).
- [179] Johnson, J. E. and S. L. Rolston. *Interactions between Rydberg-dressed atoms*, Physical Review A - Atomic, Molecular, and Optical Physics **82.** (Sept. 2010). DOI: [10.1103/PhysRevA.82.033412](https://doi.org/10.1103/PhysRevA.82.033412) (cit. on p. 93).
- [180] Riehle, F. *Frequency Standards*. Wiley, Sept. 2003. DOI: [10.1002/3527605991](https://doi.org/10.1002/3527605991) (cit. on p. 95).
- [181] Lorenz, N., L. Festa, L.-M. Steinert, and C. Gross. *Raman Sideband Cooling in Optical Tweezer Arrays for Rydberg Dressing*. Oct. 2020. URL: <http://arxiv.org/abs/2010.07838> (cit. on p. 100).
- [182] Zhang, S., F. Robicheaux, and M. Saffman. *Magic-wavelength optical traps for Rydberg atoms*, Physical Review A - Atomic, Molecular, and Optical Physics **84.**, 043408 (Oct. 2011). DOI: [10.1103/PhysRevA.84.043408](https://doi.org/10.1103/PhysRevA.84.043408) (cit. on p. 103).
- [183] Anderson, S. E., K. C. Younge, and G. Raithel. *Trapping Rydberg Atoms in an Optical Lattice*, Physical Review Letters **107.**, 263001 (Dec. 2011). DOI: [10.1103/PhysRevLett.107.263001](https://doi.org/10.1103/PhysRevLett.107.263001) (cit. on p. 103).
- [184] Piotrowicz, M. J., M. Lichtman, K. Maller, G. Li, S. Zhang, L. Isenhower, and M. Saffman. *Two-dimensional lattice of blue-detuned atom traps using a projected Gaussian beam array*, Physical Review A **88.**, 013420 (July 2013). DOI: [10.1103/PhysRevA.88.013420](https://doi.org/10.1103/PhysRevA.88.013420) (cit. on p. 103).
- [185] Goldschmidt, E. A., T. Boulier, R. C. Brown, S. B. Koller, J. T. Young, A. V. Gorshkov, S. L. Rolston, and J. V. Porto. *Anomalous Broadening in Driven Dissipative Rydberg Systems*, Physical Review Letters **116.**, 113001 (Mar. 2016). DOI: [10.1103/PhysRevLett.116.113001](https://doi.org/10.1103/PhysRevLett.116.113001) (cit. on p. 103).
- [186] Boulier, T., E. Magnan, C. Bracamontes, J. Maslek, E. A. Goldschmidt, J. T. Young, A. V. Gorshkov, S. L. Rolston, and J. V. Porto. *Spontaneous avalanche dephasing in large Rydberg ensembles*, Physical Review A **96.**, 053409 (Nov. 2017). DOI: [10.1103/PhysRevA.96.053409](https://doi.org/10.1103/PhysRevA.96.053409) (cit. on p. 103).
- [187] Aman, J. A., B. J. Desalvo, F. B. Dunning, T. C. Killian, S. Yoshida, and J. Burgdörfer. *Trap losses induced by near-resonant Rydberg dressing of cold atomic gases*, Physical Review A **93.**, 043425 (Apr. 2016). DOI: [10.1103/PhysRevA.93.043425](https://doi.org/10.1103/PhysRevA.93.043425) (cit. on p. 103).
- [188] Adema, J. "A low noise Laser system for high fidelity Rydberg atom manipulation." MA thesis. TU Munich, 2019 (cit. on p. 104).
- [189] Robert, S. W. I. "Magneto-optical trapping of potassium isotopes." PhD thesis. University of Wisconsin - Madison, 1997 (cit. on p. 105).
- [190] Tiecke, T. "Feshbach resonances in ultracold mixtures of the fermionic quantum gases 6Li and 40K." PhD thesis. University of Amsterdam, 2009 (cit. on p. 105).